IONICALLY-FUNCTIONALIZED LEAD SULFIDE NANOCRYSTALS

by

IAN STORMS MOODY

A DISSERTATION

Presented to the Department of Chemistry
and the Graduate School of the University of Oregon
in partial fulfillment of the requirements
for the degree of
Doctor of Philosophy

December 2011

DISSERTATION APPROVAL PAGE

Student: Ian Storms Moody

Title: Ionically-Functionalized Lead Sulfide Nanocrystals

This dissertation has been accepted and approved in partial fulfillment of the requirements for the Doctor of Philosophy degree in the Department of Chemistry by:

David R. Tyler	Chair
Mark C. Lonergan	Advisor
Catherine J. Page	Inside Member
Andrew Marcus	Inside Member
Hailin Wang	Outside Member

and

Kimberly Andrews Espy	Vice President for Research & Innovation/ Dean of the Graduate School

Original approval signatures are on file with the University of Oregon Graduate School.

Degree awarded December 2011

DISSERTATION ABSTRACT

Ian Storms Moody

Doctor of Philosophy

Department of Chemistry

December 2011

Title: Ionically-Functionalized Lead Sulfide Nanocrystals

Lead sulfide nanocrystals (PbS-NCs) are an important class of semiconductor nanomaterials that are active in the near-infrared and exhibit unique properties distinct from their bulk analogues, notably, size tunability of the band gap and solution processability. One factor influencing PbS-NC properties is the presence of an organic ligand shell, which forms the interface between the nanocrystal core and its environment. The specific focus of this dissertation is how *ionic functionalization* of the ligand shell alters the physical and chemical properties of the resulting PbS-NC/ligand complex.

Short-chain ligands can improve photoconductivity in PbS-NC thin films, but there are few solution-based preparations available. Chapter II demonstrates how ionic groups can enable functionalization of PbS-NCs with two short-chain thiol ligands – sodium 3-mercaptopropanesulfonate (MT) and sodium 2,3-dimercaptopropanesulfonate (DT) – via a solution-phase exchange procedure. Despite a structural similarity, DT-functionalized PbS-NCs (PbS-DT) are more stable to oxidation than MT-functionalized PbS-NCs (PbS-MT). The relative stabilities are explained in terms of different binding modes to the nanocrystal surface (bidentate vs. monodentate) and oxidation pathways (intermolecular vs. intramolecular).

Toxicology studies on nanomaterials have been limited by the availability of water-soluble samples with systematically controlled structures. As examples of such materials, PbS-DT and PbS-MT nanocrystals are studied in Chapter III for their toxicological impacts on embryonic zebrafish. PbS-DT solutions induce less toxicity than PbS-MT solutions, which is explained in terms of the relative stabilities of the nanocrystal solutions.

Finally, Chapter IV investigates the hitherto unexplored effects of ionic functionalization on the optical/electrical properties of PbS-NC thin films, with an emphasis on understanding how counter ions affect the photoconductivity of PbS-DT thin films. Films containing small counter ions exhibit increased dark conductivity and responsivity with time under an applied bias, whereas films containing larger or multivalent counter ions show a suppression of this behavior. These results are discussed in terms of ion motion and ion-assisted carrier injection at the PbS-NC/electrode interface.

This dissertation includes previously published and unpublished co-authored material.

CURRICULUM VITAE

NAME OF AUTHOR: Ian Storms Moody

GRADUATE AND UNDERGRADUATE SCHOOLS ATTENDED:

University of Oregon, Eugene, OR
University of California, Davis, CA
Cabrillo Community College, Aptos, CA

DEGREES AWARDED:

Doctor of Philosophy, Chemistry, 2011, University of Oregon
Master of Science, Chemistry, 2007, University of Oregon
Bachelor of Science, Chemistry, 2002, University of California, Davis

AREAS OF SPECIAL INTEREST:

Materials Science
Nanotechnology
Electronic Materials
Green Materials

PROFESSIONAL EXPERIENCE:

Graduate Research Assistant, Department of Chemistry, University of Oregon, Eugene, OR, 2006 - 2011

Graduate Teaching Assistant, Department of Chemistry, University of Oregon, Eugene, OR, 2005 - 2006

Materials Research Technician, DuPont Displays, Goleta, CA, 2003 - 2005

GRANTS, AWARDS AND HONORS:

National Science Foundation IGERT Fellowship, 2009 - 2011

Albert Leoni Scholarship, 1999 - 2000

PUBLICATIONS:

Lisa Truong, Ian S. Moody, Dylan P. Stankus, Jeffrey A. Nason, Mark C. Lonergan, and Robert L. Tanguay, Differential Stability of Lead Sulfide Nanoparticles Influences Biological Responses in Embryonic Zebrafish, *Archives of Toxicology*, 85:787-798, 2011.

Che-Hsiung Hsu, Sunghan Kim, Ian S. Moody, Electrically Conductive Polymer Compositions, U.S. Patent # 7,727,421, 2010.

Che-Hsiung Hsu, Sunghan Kim, Ian S. Moody, Electrically Conductive Polymer Compositions, U.S. Patent # 7,638,072, 2009.

Ian S. Moody, Andreas R. Stonas, and Mark C. Lonergan, PbS Nanocrystals Functionalized with a Short-Chain, Ionic, Dithiol Ligand, *The Journal of Physical Chemistry C*, 112:19383-19389, 2008.

ACKNOWLEDGEMENTS

First and foremost, I would like to thank my advisor Dr. Mark Lonergan who was instrumental in my professional development and whose strengths as a teacher and deep scientific thinker, I can only hope to emulate. Secondly, I would like to thank Drs. Che Hsu and Hjalti Skulason, who were my first teachers in applied scientific inquiry, and inspired my pursuit of a Ph.D. Thanks, also, to past and present members of the Lonergan Lab Research Group who have been my colleagues and friends and have provided helpful feedback throughout my graduate school career.

I would also like to thank all of the talented staff at CAMCOR, in particular, Kurt Langworthy, Josh Razink and Sujing Xie, who taught me the proper way to image nanocrystals, as well as Stephen Golledge and Jason Fahrion for their aid with data collection and analysis with the XPS. Funding from the Air Force Research Laboratory (under agreement number FA8650-05-1-5041), the W.M. Keck Foundation, and the National Science Foundation IGERT program (under Grant No. DGE-0549503) are acknowledged. Voxtel, Inc. and Dune Sciences, Inc. kindly provided access to some of the research instruments and materials used in these studies. The toxicology experiments were performed in conjunction with Lisa Truong and Dr. Robert L. Tanguay who thank the Sinnhuber Aquatic Research Laboratory for the embryos and Cari Buchner for her technical assistance, and acknowledge funding from the National Institute of Environmental Health Sciences (under grant number P3000210) and the Environmental Protection Agency (under grant number RD-833320).

Outside of the lab, I would like to send out a heartfelt thanks to my friend and colleague Dr. Erich Chapman, whose scientific curiosity and general enthusiasm

for life have inspired me to keep a broad view of my professional prospects and maintain a strong sense of my role as a scientist. Thanks to members of my graduate class and all members, past and present, of Specific Heat that have allowed me to maintain my sanity through all of the rigors of graduate school. Thanks to all of the Eugene coffeehouses that have put up with my haunting presence over the years – in particular, Matt and the other talented folk at June, and Jimmy at Black Cat Coffee, whose espresso magic helped catalyze more than a few of the deep thoughts and scientific ideas presented herein. Similarly, I would like to send a heartfelt shout out to MacKlemore and Lafa Taylor, whose uplifting beats have helped this author maintain his mental and spiritual health.

A special thanks to my parents Beth and Storms, and sister Laurel, who have always supported me and instilled in me a general wonder for life and a yearning to understand the unknown. Finally, I would like to thank my loving wife Lauren, who has shared this wonderful Oregon experience with me and has been a pillar of stability throughout all of the uncertainties.

For Lauren, whose care and understanding knows no bounds,

and for the new little person in our lives, who I can't wait to meet.

TABLE OF CONTENTS

Chapter Page

LIST OF FIGURES

Figure Page

Figure Page

CHAPTER I

GENERAL INTRODUCTION

1.1. Introduction to Nanomaterials

Nanomaterials are a widely studied class of materials that encompass a diverse range of structure and composition. Nanomaterials are generally defined as those materials having physical dimensions of 1 to 100 nm and whose physical and/or chemical properties are at least partially influenced by their size[1]. Semiconductor nanocrystals (SC-NCs) – a subset of nanomaterials – have been increasingly studied over the last few decades due to their unique optical and electrical properties. Interest in SC-NC research has been the result of two main factors: 1) improved synthetic control over nanomaterial size and structure, and 2) improved understanding of their physical properties and how to modify them for desired applications. This knowledge of fundamental properties has, in turn, inspired more applied research on methods for integrating SC-NCs into consumer and industrial products. SC-NCs have been investigated for use in a wide variety of technologies, e.g. electroluminescent devices[2,3], biological imaging agents[4,5], and photovoltaic devices[6].

The lead chalcogenides make an interesting subset of the general class of SC-NCs. Due to their narrow electronic bandgap, they offer sensitivity to the near-infrared (NIR) region of the electromagnetic spectrum[5]. This region is inaccessible to many other materials, and yet NIR-activity has important applications in the fields of photovoltaics[7], photodetection[8], and biological imaging[9].

The primary subject of this dissertation is ionically-functionalized lead sulfide nanocrystals (PbS-NCs). The rest of this chapter will attempt to put this

focused subject of study into the greater context of SC-NC research. To provide background, this chapter will introduce the unique size-dependent optical properties of semiconductor nanocrystals (SC-NCs), and discuss synthetic methods and surface passivation schemes used in the preparation of these materials, with a particular emphasis on the lead chalcogenides. Special focus will be put on the hot-injection method using organometallic precursors and ligand-exchange techniques used to prepare the PbS-NCs discussed herein. The organic/inorganic interface – between organic ligand shell and inorganic SC-NC core – will be discussed in terms of its effects on: a) nanocrystal growth, b) passivation of surface states, c) stability to oxidation, and d) charge separation and transport in SC-NC thin films. Charge transport mechanisms and photoconductivity processes will also be introduced, especially as they relate to disorderd semiconductor systems, such as SC-NC solids.

1.2. Overview of Unique Properties of Semiconductor Nanocrystals

1.2.1. Electronic Structure and Energy Transitions in Semiconductors

Semiconductor nanocrystals (SC-NCs) share many of the same properties as their bulk material analogues. As a review, the electronic structure of a bulk semiconductor is composed of energy bands, which are a continuum of closely-spaced energy levels centered around the energy levels of its atomic constituents. The existence of bands is a direct result of the fact that bulk materials are made up of many atoms, whose atomic orbitals overlap and combine to form band structures. As such, the optical and electrical properties of semiconductors are governed by the energy levels of the electronic states composing their valence and conduction bands. More specifically, it is the difference in energy between the edges of the filled valence band and the vacant

conduction band – the electronic band gap – that governs the electrical conductivity and sensitivity to light for a particular material[10].

Semiconductors absorb light by virtue of the available energy levels in their electronic structure, and the band gap defines one of the most important of these transitions. Whenever a photon of energy greater than or equal to the band gap is absorbed by a semiconductor, an electron in the valence band is excited up from the valence band to the conduction band, creating an electron-hole pair. Any absorbed energy in excess of the band gap energy is temporarily stored as kinetic energy, until it is released through emission of vibrational energy (as a phonon) and the electron and hole thermalize to their respective band edges (see Figure 1.1). This electron-hole pair is bound electrostatically through Coulombic forces and is known collectively as an *exciton*[10].

Once generated, the exciton can follow several relaxation paths back to the ground state, as depicted in Figure 1.1. *Recombination*, in which the exciton merges at a common site, can occur radiatively or non-radiatively. Radiative recombination – or *fluorescence* – involves a direct transition of the electron from the conduction band to the valence band concommitant with emission of a photon of energy equal to the band gap, sometimes termed "band-edge" emission. Non-radiative recombination is facilitated by the presence of mid-gap trap states that can be accessed by excited electrons and holes through thermal relaxation and emission of several lower-energy phonons[11]. Mid-gap traps, or recombination centers, are associated with undercoordinated surface atoms, and they are discussed in greater detail in the section on photoconductivity.

Excitons can also be separated into free electrons and holes – *free carriers* – if enough energy is available to overcome their electrostatic attraction – the *exciton*

binding energy. Once generated, free carriers can move throughout the crystal lattice until they meet and recombine with another hole (or electron) or else are extracted out of the material through a contact at a metal electrode[11].

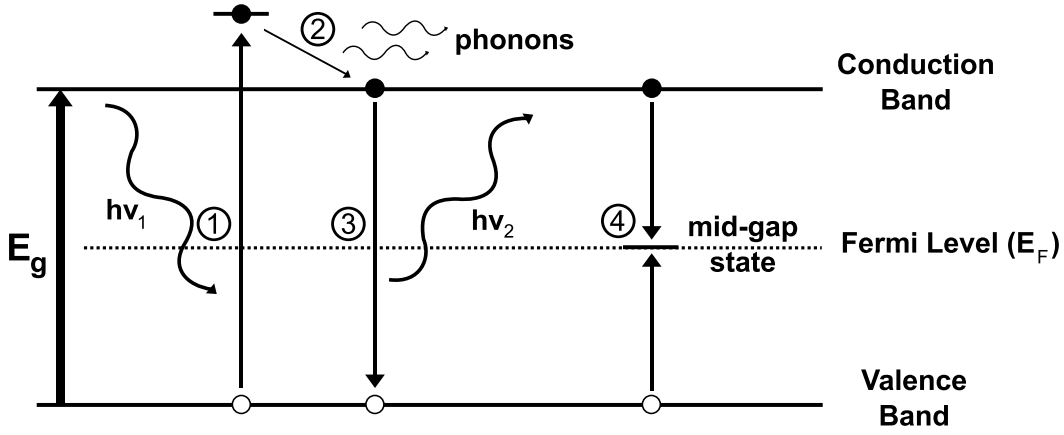

FIGURE 1.1. Excitation and emission pathways in a semiconductor.
1) Absorption of a photon (hv_1) of energy greater than the band gap energy (E_g), and concommitant excitation of an electron from the valence band to the conduction band. 2) Thermal relaxation of electron to conduction band edge. 3) Radiative recombination with band-edge emission (hv_2). 4) Non-radiative recombination via a mid-gap trap state.

1.2.2. Effects of Crystal Size on the Electronic Band Gap and Related Properties

Bulk semiconductors exhibit a constant band gap, independent of their physical dimensions. However, when semiconductor crystals are sufficiently reduced in size – down to the nanoscale regime of a few hundred to a thousand atoms – the band structure begins to break down, and energy levels become more discrete, or "quantized"[12]. This quantization of energy levels occurs first at the edges of the bands where the density of states is lowest, and the bands are narrowed as a result, see Figure 1.2. Most significantly, the band gap is dependent on the relative energy levels

of the band edges, and as such, it is highly sensitive to changes in crystal dimensions within this size regime. This phenomenon is known as *quantum confinement*, and is conceptually analogous to the quantum mechanical "particle in a box" [12]. Smaller nanocrystals exhibit greater quantum confinement, and subsequently a greater band gap energy, than larger crystals. This *size tunability* is one property that makes SC-NCs unique from bulk materials.

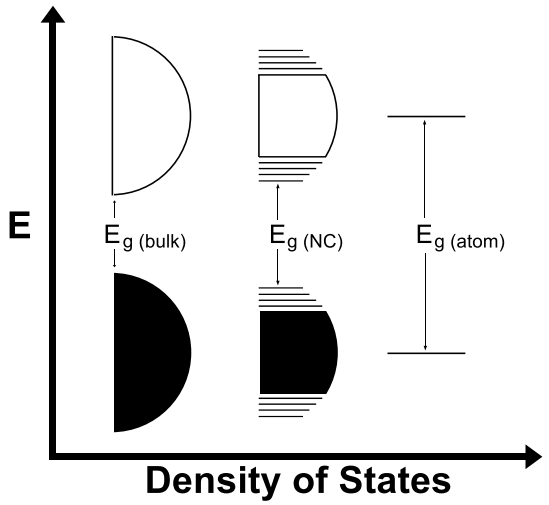

FIGURE 1.2. Effects of crystal size on the band structure of a semiconductor. From Alivisatos, A. P. *Science*, **1996**, *271*, 933-937. Reprinted with permission from AAAS.

Quantum confinement can only occur in nanocrystals that are smaller than the natural length scale of electrons and holes in the bulk material. This length scale is determined by a quantity called the Bohr radius (a_B):

$$a_B = \varepsilon \frac{m}{m^*} a_0 \qquad \text{(Equation 1.1)}$$

where ε is the dielectric constant, m^* is the effective mass of either the electron, hole, or exciton, m is the rest mass of the electron, and a_0 is the Bohr radius of the hydrogen atom [13]. Different Bohr radii can be defined, one for each, for the electron, hole, and

exciton. Excitons, electrons, or holes generated in a semiconductor crystal become "confined" when the crystal radius becomes smaller than the respective Bohr radii for the given material[13]. When all three of these particles are confined, the nanocrystal is said to be within the *strong confinement regime*; nanocrystals governed by this condition exhibit a band gap that is determined by its size. Thus, the larger the Bohr radius for a given material, the greater the range in size for which a crystal will exhibit quantum size effects.

The size-tunability of the band gap of SC-NCs gives them properties unique from the bulk material. From a practical point of view, the most significant of these properties is that the absorption and emission spectra of SC-NCs can be tuned with size. The quantization of energy levels (discussed above) also alters the absorption spectrum from a continuous band to one with peaks corresponding to energy transfer between the discrete energy levels. Because quantization is seen most prominently at the band edges, peaks show up on the low-energy side of the spectrum – near the absorption onset, with the high energy response dominated by the broad, featureless absorption of the bulk[14]. The lowest energy feature in a SC-NC absorption spectrum is called the *first exciton peak* and defines the optical band gap of the material. Subsequent spectral peaks are labeled the *second*, *third*, etc. exciton peaks, and correspond to higher energy transitions between discrete energy levels. The quantity, intensity, and energy spacing of excitonic features is dependent upon the electronic structure of the SC-NC, and is highly material-dependent.

The lead chalcogenides – PbE (E = S, Se, Te) have relatively large bulk exciton Bohr radii – ∼20 nm for PbS and ∼46 nm for PbSe[14,15], as a result of their relatively low effective masses for holes and electrons, and high dielectric constants. This allows for a large range of crystal sizes that will fall into the strong confinement regime, and

exhibit size tunable properties. The lead chalcogenides are considered *narrow band gap semiconductors* – E_g = 0.41, 0.28, and 0.31 eV, for bulk PbS, PbSe, and PbTe, respectively[5]. In PbE nanocrystals, quantum confinement creates a "blue-shift" in their absorption and emission features, allowing them to be tuned across the near-infrared (NIR) region of the electromagnetic spectrum (800-1600 nm), which is an important region for a variety of technologies[10].

Another interesting phenomenon, *multiple exciton generation* (MEG) – also known as impact ionization, in bulk materials – is the creation of more than one electron-hole pair per absorbed photon[16]. MEG is not a unique process to nanocrystals, however there are certain features of the electronic structure of SC-NCs that increase its efficiency in these materials. Normal exciton generation has been described above as the generation of a single electron-hole pair, through absorption of light greater than or equal to the band gap. Excess kinetic energy is transmitted via vibrational energy transfer to the matrix until the excited carriers reach their band edges. In MEG, an exciton with excess kinetic energy (sometimes called a "hot carrier") can transfer its energy to excite another electron up from the valence band – in effect, creating two excited carriers, or excitons (see Figure 1.3). In principal, MEG can occur for any absorbed photon of at least twice the band gap energy, but in practice the energy threshold can be much higher. The efficiency of MEG is governed by the relative rates of relaxation mechanisms available to these "hot carriers", and MEG time scales are typically much lower than those of competing pathways such as thermalization[16].

In SC-NCs, the smaller number of atoms relative to bulk crystals results in less available modes of vibrational energy transfer. This phenomenon is sometimes called the "phonon bottleneck," and it can make MEG more competitive against phonon-

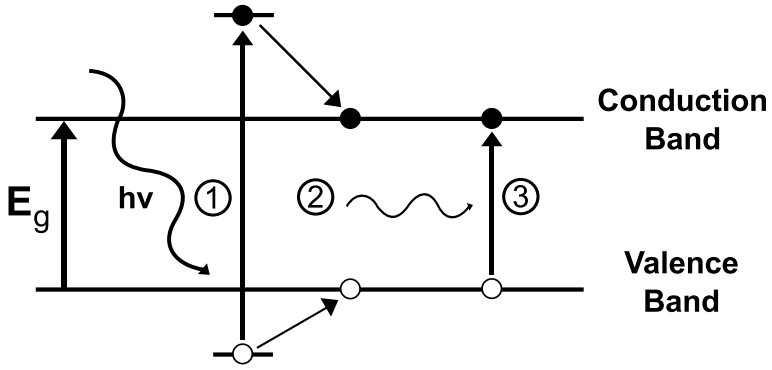

FIGURE 1.3. The process of multiple exciton generation (MEG). 1) Absorption of photon with energy (hv) at least twice the band gap (E_g) excites an electron from the valence band into the conduction band. 2) Relaxation of excited electron and hole to the conduction and valence band edges. 3) Energy transfer from the relaxation of the first exciton creates a second exciton.

assisted relaxation pathways[16]. Two, three, or more excitons can be created through MEG by increasing the photon energy, but the resulting bi- and tri-excitons have increasingly shorter lifetimes. Of SC-NCs, the lead chalcogenides – notably PbS and PbSe – have shown some of the highest efficiencies and lowest photon energy thresholds for observation of MEG[17,18].

Much of the interest surrounding MEG comes from its potential to greatly enhance the efficiencies of photovoltaic devices (PVs). The ability to extract more than one charge carrier for every incident photon raises the bar on the ultimate power efficiency achievable in a photovoltaic device, known as the Shockley-Queisser limit[16]. The increased efficiencies of MEG in SC-NCs gives PVs based on these materials a leg up over traditional designs, assuming other factors limiting the performance in SC-NC devices can be resolved.

1.2.3. Effects of Nanocrystal Structure and Shape

Synthetic methods have been developed that allow SC-NCs to be made using straightforward chemical techniques. Typical methods employ an organometallic approach in which the resulting particles are capped with an organic ligand shell – organic molecules bound to the crystal surface – which make them soluble in common organic solvents. In addition to solubilizing the nanocrystals, this ligand shell provides steric bulk to prevent agglomeration of particles and to keep them discrete so as to maintain their unique optical and electrical properties. An overview of SC-NC synthetic methods will be discussed in more detail in the following section.

The presence of an organic ligand shell influences the electronic structure of SC-NCs. Ligand molecules are typically electron-donating and coordinate to under-coordinated, and electron-poor, metal atoms (or surface states) on the nanocrystal surface. At first glance, it might appear that the presence of the ligand shell would act as a perturbation to the typical properties of the SC-NC core – e.g. absorption and emission profile – but in fact, it enhances them[12]. This is because surface states act as defects to the bulk crystalline properties by introducing mid-gap or other trap states into the otherwise pristine band structure of the bulk material. Electron donation from the ligand shell fills – or *passivates* – these energy levels, leaving an abrupt energy edge between the SC-NC and its environment.

Core-shell SC-NCs – in which a "core" of one semiconductor is encased in a "shell" of another semiconductor material – can exhibit distinct properties from "core-only" nanocrystals. Like organic ligands, inorganic shells can passivate surface states of the core material, which can improve fluorescence through suppression of nonradiative recombination processes associated with electronic mid-gap states.

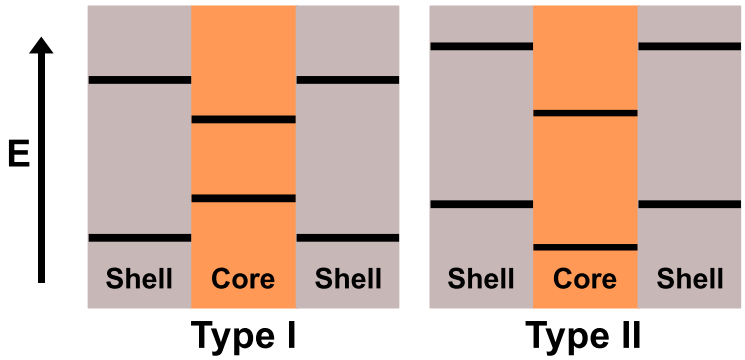

FIGURE 1.4. Schematic of two possible heterojunctions arising from a SC-NC core-shell structure. The relative positions of the band edges for core and shell materials determine whether photoexcited electrons and holes are "confined" to the core (Type I), or are separated with one carrier confined to the core and the other "extracted" to the shell (Type II). In the example shown here, electrons are confined to the core, while holes are extracted to the shell.

The core-shell interface also adds an additional level of complexity, which can be utilized to tune the properties of the material. Choice of core and shell materials of disparate band gap energies can lead to the formation of a junction at the core-shell interface. Such a junction can be "confining" or "extracting" to electrons and holes based on the relative valence and conduction band edge energy levels of the core and shell materials. Figure 1.4 shows two possible configurations of core-shell energy levels and the effect on junction type. Type I heterojunctions – in which both electron and hole are confined to the core material – tend to be the most commonly reported in the literature, as this junction is optimal for achieving high fluorescence efficiencies in photoluminescent or electroluminescent applications. There have been a few reports of utilizing Type II heterojunctions – in which either a hole or an electron is confined, while its partner is extracted – for improving photogenerated charge carrier extraction from PbS/PbSe core-shell nanocrystals[19]. In some cases,

shell materials can contribute additional properties of their own, but typically, core-shell nanocrystals are dominated by the properties of the core.

Numerous methods have also been developed to control the shape of SC-NCs, from common "spherical" particles (more appropriately, "spheroids") to rods, tetrapods, and stars. Shape, like particle size, has a strong influence over the optical and electrical properties of SC-NCs. Nanorods – crystals with an aspect ratio greater than one, and with asymmetric growth confined to a single dimension[20] – can exhibit multi-excitonic features related to the two dimensions of confinement. Tetrapods, stars, and other more exotic nanostructures can exhibit additional opto-electronic properties, and they have utility related to these properties as well as increased interfacial effects afforded by the greater surface area-to-volume ratios relative to spheres[21].

Although core-shell and non-spherical SC-NCs exhibit many intriguing properties, this dissertation only discusses the synthesis and properties of spheroidal, core-only PbS nanocrystals. The background on core-shell materials is intended only to provide the reader with context for the general state-of-the-art of SC-NC preparation.

1.3. Preparation of Semiconductor Nanocrystals

A procedure for the deliberate synthesis of semiconductor nanocrystals was first reported in 1983 with the report of a preparation for CdS crystallites[22]. Since that time, many methods towards monodisperse, size-controllable nanocrystal syntheses have been developed[23,24]. One of the most versatile methods has been the so-called "organometallic" approach[25]. This solution-based method utilizes molecular precursors, which are first dissolved independently in high-boiling, organic solvents

in the presence of one or more organic capping agents, and then mixed rapidly at elevated temperatures to initiate nucleation and crystal growth. The capping agent, typically an electron-donating organic molecule such as a carboxylic acid, thiol, or amine, coordinates with the metal precursor to passivate the reactive surface, and control growth and agglomeration under the reaction conditions. An ideal capping agent will act as a labile ligand under the elevated temperatures of the synthesis – coordinating with the metal to prevent excessive crystal growth rates, but binding weakly enough so that it can be readily replaced to allow controlled growth[25].

Much of the theory behind control of nanocrystal nucleation and growth is based on early experimental and theoretical work performed by LaMer and Dinegar[26] to understand the formation and growth of sulfur colloids in a supersaturated solution of dissolved sulfur. In their system, LaMer and Dinegar were able to describe the conditions under which a relatively monodisperse sample of colloids could be formed through simple adjustment of the initial concentration of precursor, temperature of the reaction, and solubility of the precursor in the given solvent system. Key to this control was an understanding that nucleation and growth events needed to be separated in time during the synthesis.

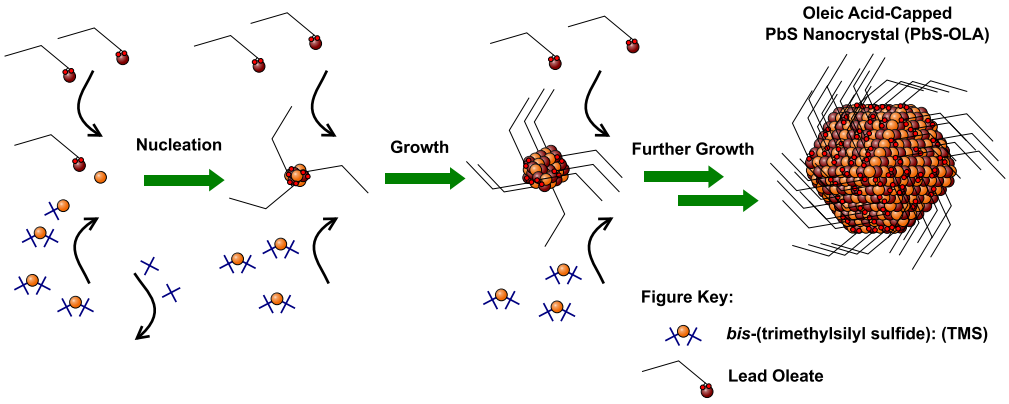

FIGURE 1.5. Schematic of PbS-OLA synthesis

In the organometallic preparation of semiconductor nanocrystals, the separation of nucleation and growth events is acheived through the rapid mixing of molecular precursors under elevated temperatures. The fast addition creates a supersaturated solution of precursor, which is relieved by a rapid nucleation event forming large numbers of small crystallites. Ideally, mixing is quick and uniform, the nucleations take place nearly simultaneously, and the resulting nanocrystals encompass a narrow size distribution. Growth then proceeds at lower monomer concentrations, where additional precursor is consumed by the already-formed nuclei, see Figure 1.5. Since growth in the low monomer concentration regime is presumably uniform, the nanocrystals maintain their tight size distribution until growth is quenched – either through exhaustion of monomer supply, reduction of temperature, or precipitation via addition of a non-solvent[25].

One of the benefits of the organometallic method is that SC-NC functionalization can, at least in part, be controlled through the choice of capping agent (or ligand) used during the synthesis. Ligands that bind to the metal precursors during nucleation and growth remain attached to undercoordinated atoms on the nanocrystal surface – imbuing the particles with solubility and passivating the typically undesirable optical and electronic properties of "dangling bonds" or surface states[12]. Although in principle, choice of "native" ligand (used during the synthesis) is vast, in practice, selection of ligand functionality is limited by its: 1) ability to control size and growth – determined by the binding strength and steric bulk of the ligand and 2) compatibility with the synthetic conditions – which includes its volatility, and reactivity with the precursor solution. Numerous post-synthetic functionalization methods have been developed, therefore, to increase the versatility of SC-NCs, and will be discussed in the following section.

First, however, is a brief review of some relevant syntheses that have been developed for preparation of SC-NCs, and lead chalcogenides, in particular. Early gas-phase or solution-phase syntheses for PbE-NCs suffered from poor size tunability and dispersity. PbE-NCs with lower defect densities and higher luminescent efficiencies could be prepared within a glass-host matrix; however once synthesized, sequestration and purification of the nanocrystals was infeasible. In 1993, a novel synthetic route – the organometallic method – was demonstrated for the preparation of cadmium chalcogenide nanocrystals that allowed for monodisperse, defect-free, and soluble nanocrystals[23]. In 2001, Peng et al. demonstrated the versatility of this approach, and showed that the synthesis was amenable to a number of different Cd-precursors and capping agents that allowed for further tunability of the size dispersity, luminescence efficiency, and shape control of the resulting particles[27,20,28]. Also, in 2001, Murray et al. showed that this technique could be used for the preparation of PbSe-NCs[29]. In 2003, Hines and Scholes greatly expanded this technique for the preparation of PbS-NCs[30]. The Hines and Scholes method, and minor variations thereof, have since become the standard technique for the preparation of PbS-NCs.

In the Hines and Scholes method, PbS-NCs are prepared in a one-pot synthesis, see Figure 1.5. Lead oleate and bis(trimethylsilyl)sulfide are used as the respective Pb- and S-precursors, respectively, with generation of lead oleate occurring *in situ* through the reaction of lead(II) oxide with oleic acid under application of moderate temperatures (∼100 °C) and vacuum. A solution of bis(trimethylsilyl)sulfide in a non-coordinating solvent – 1-octadecene – is prepared separately. Nucleation of PbS-NCs occurs through the quick injection of the S-precursor solution into the Pb-oleate mixture in conjunction with rapid stirring. Growth then proceeds until the reaction is quenched through either reduction of temperature or addition of a non-solvent, such

as acetone. The result is oleate-capped PbS-NCs that can be purified through simple precipitation and washing steps. Particle size is controlled via reaction temperature, ratios of the Pb- and S-precursors to the ligand – oleic acid, and growth time. Additionally, this procedure results in a population of nanocrystals that undergo "size-distribution focusing," which further tightens the size distribution over time, and is discussed in detail in the following subsection.

SC-NCs of multi-component systems can also be synthesized via a modification of the organometallic method. Surrounding a nanocrystal "core" of one material with a "shell" of another semiconductor material leads to so-called "core-shell" structures. As discussed in the previous section, core-shell nanocrystals exhibit optical and/or electrical properties distinct from their "core-only" counterparts. In one sense, inorganic shells can be thought of as an extension of the organic ligand passivation concept – with electron-donating molecules being replaced with thin layers of inorganic semiconductor grown epitaxially atop the core material, and serving a similar purpose – quenching surface states of the core material[31,32,33].

In addition to syntheses which lead to roughly "spherical" particles, there have been many systems studied that result in more exotic shapes, such as nanorods[20] and tetrapods[21]. Control over nanocrystal shape, like that over size, can lead to additional material properties such as improved interfacial areas for junction formation. Synthetically, nanocrystal shape can be controlled through the tuning of the reaction starting conditions and choice of capping agent. Some material sets are more amenable to shape control than others. Semiconductor crystallites that contain more than crystal orientation, can be induced to grow along a certain axis through preferred attachment of ligands to one lattice plane over the others. Binding of ligands to a crystal facet impedes growth at that site, forcing growth to proceed

asymmetrically along other non-coordinated facets. For example, CdSe crystallites are known to exhibit preferred growth along the (00$\underline{1}$) axis in wurtzite crystals under the right conditions of ligand and monomer concentrations[20].

1.3.1. Ripening Processes

Once nucleated, the growing crystals are susceptible to several known "ripening" mechanisms which can either narrow or broaden the crystal size distribution depending on the conditions of the reaction mixture. If monomer concentrations are low during the growth period, nanocrystal solutions will undergo a "size-defocusing" event described by an Ostwald ripening mechanism[25]. Smaller particles, with a larger surface-to-volume ratio are more unstable because they have a greater percentage of reactive surface atoms. As a result, the low-monomer concentration conditions induce re-dissolution of small particles back into solution, which fuel the growth of larger particles. This has the effect of skewing the nanocrystal solution toward larger and broader particle size distributions. This is illustrated in the left-hand portion of the graph in Figure 1.6, where crystals below a certain "critical size" have a negative growth rate.

With a high monomer concentration, however, the nanocrystal solution will undergo "size-distribution focusing"[25]. The smaller particles become stabilized when there is a plentiful amount of monomer present. Under these conditions, the solution will spontaneously narrow its size distribution due to the faster growth rate of small crystals compared to large crystals. Large crystals require greater amounts of monomer to increase in radius relative to small crystals. This concept is well illustrated in the "High monomer concentration" curve of Figure 1.6, where high

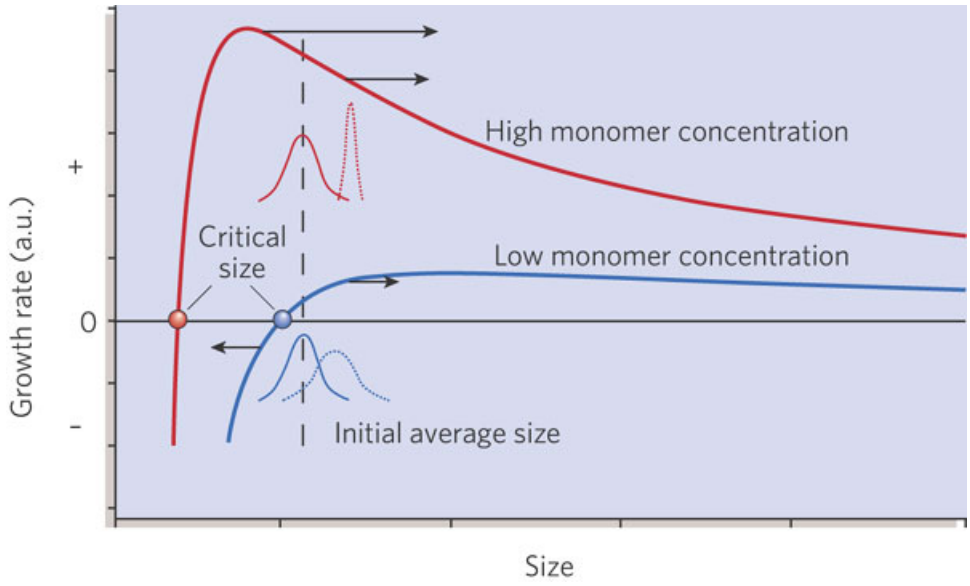

FIGURE 1.6. Size focusing and defocusing ripening mechanisms. Reprinted by permission from Macmillan Publishers Ltd: Nature. Yin, Y. , Alivisatos, A. P. *Nature*, **2005**, *437*, 664-670, copyright 2005.

growth rates exist for small crystals, and lower growth rates are seen for larger crystals. Over time this behavior will lead to a narrowing of the size distribution.

1.4. Surface Functionalization of Semiconductor Nanocrystals

Many of the more intriguing applications of SC-NCs involve further modification of the nanocrystal surface. In general, capping agents (or ligands) that are desirable for controlling nucleation and growth in optimized SC-NC syntheses are less than optimal for a desired application. For example, many of the ligands utilized in organometallic syntheses are long-chain, fatty acids, thiols, or phosphines[25]. Alkyl group-terminated ligand shells like these, although easily dispersible in non-polar organic solvents, are poorly soluble in aqueous systems – a key requirement for biological fluorescent markers. Furthermore, even if as-synthesized SC-NCs functionalized with these fatty acid ligands could be induced to stay suspended in

polar media, the alkyl chains offer, at best, *non-specific* binding to any desirable biological targets. This limits the use of as-synthesized SC-NCs in aqueous biological systems.

As another example, the application of SC-NCs in thin-film-based electronic devices necessitates efficient electrical conduction through a SC-NC array. Long-chain alkyl ligands are typically electrically insulating and create barriers to conduction by maintaining large inter-particle separations between nanocrystals. Use of short-chain or electrically conductive ligands is therefore desired for these applications.

Several different methods have been developed for adjusting SC-NC functionalization (see Figure 1.7), and are discussed in greater detail below.

1.4.1. Surface Functionalization Techniques

Native Synthesis One method for adjusting the ligand shell composition of SC-NCs is to simply start with a ligand of desired functionality during the synthesis. This method is known as the *native synthesis* approach. The benefit of this method is straightforward: synthesis and functionalization are combined into a single step, which offer potential increases in yield and throughput. The challenge of this method lies in the need for the ligand of choice to be multifunctional – the ligand must be of sufficient lability to encourage controlled crystal growth during synthesis, while also having the desired attributes of the final functionalization (e.g. solubility, ligand length, etc.). Compromises must therefore be made to at least minimally meet all the desired properties. Nonetheless, a number of native syntheses have been developed for SC-NCs, most notably for use in aqueous solvent systems[34]. In a few cases, successful one-step syntheses of SC-NCs with short-chain ligands have also been achieved[34].

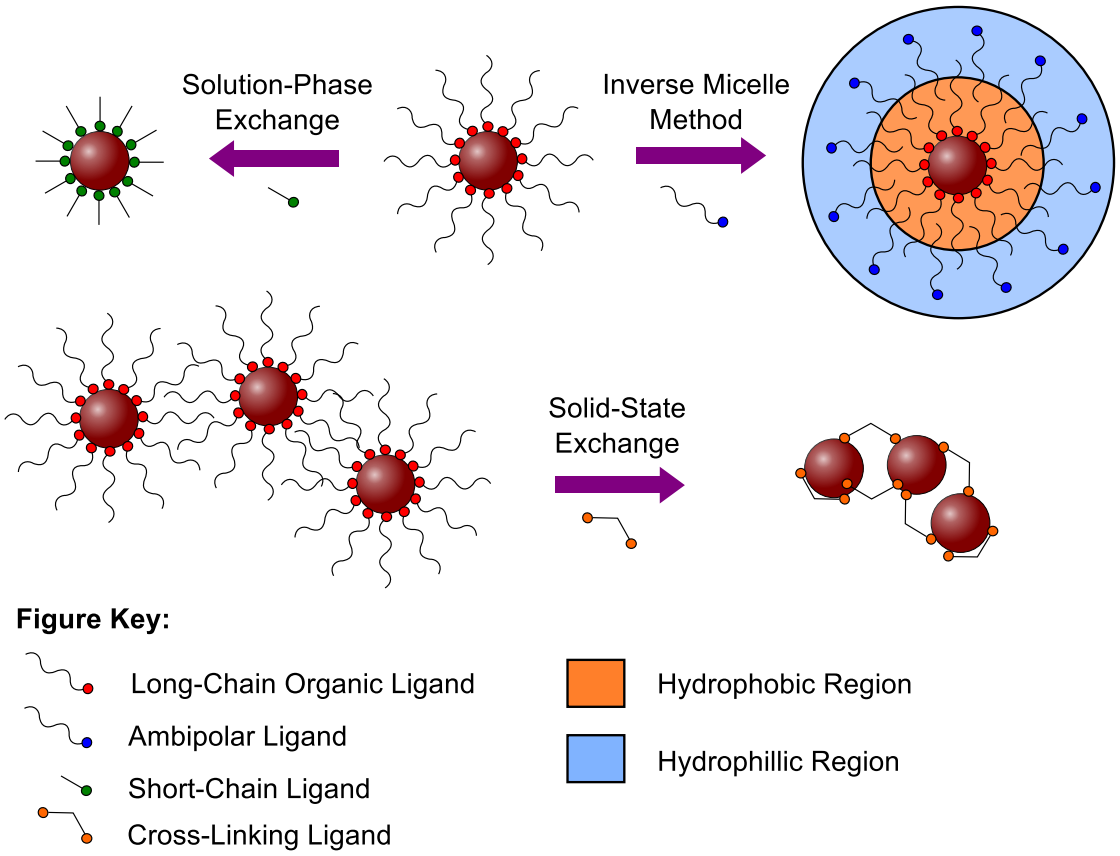

FIGURE 1.7. Schematic of SC-NC functionalization methods

Inverse-Micelles Another method for SC-NC functionalization is known as the *inverse-micelle* approach. The main goal of this method is to imbue aqueous solubility to otherwise organically-soluble particles. As the name suggests, this feat is accomplished through the introduction of an additional binding group of an ambipolar nature – one end polar, and one end non-polar. Dissolution of the non-polar SC-NCs into an aqueous mixture containing the ambipolar binding agent leads to the creation of an inverse micelle – the non-polar end of the binding group intercolates with the alkyl chains of the SC-NC ligand shell, the polar end points out into aqueous solution, and the SC-NCs become suspended, surrounded by a double-layer of ligands.

One complication of the inverse micelle approach is that the increased steric bulk surrounding the nanocrystal core – a double layer of ligands – results in a relatively large hydrodynamic radius for the inverse micelle complex. The bulky structure can limit the utility of these materials – especially in *in vivo* and *in vitro* applications, where bioavailability is strongly correlated with particle size and cellular uptake mechanisms[35].

Ligand Exchange Methods – General The following two methods of SC-NC functionalization involve the replacement of the original, native ligand with a new molecule. To achieve this, several requirements must be met by the incoming ligand. First, and most importantly, the incoming ligand must be able to competitively bind to the SC-NC surface. Ideally, the incoming ligand will bind more strongly than the original, native ligand. In practice, ligand exchange can be facilitated through exposing the natively-functionalized SC-NCs to an excess concentration of the incoming ligand.

Binding of ligands to SC-NCs generally occurs through coordination to surface metal atoms. The strength of this interaction can, in part, be predicted based on the concept of Pearson's hard/soft acid/base categorization[36,37]. SC-NCs exhibit similar affinities to those of analogous metal complexes, although oxidation state and coordination sphere have a strong influence over the relative "hardness" or "softness" of the metal ions. In nanocrystals composed of binary semiconductors, metal atoms can be thought of as existing in a "coordination sphere" of atoms of its crystal ion pair. In general, "hard" ligands (e.g. carboxylates) will bind more strongly to SC-NCs containing "hard"metal ions (e.g. ZnO), and "soft" ligands (e.g. thiols) will have a greater affinity for SC-NCs containing soft metal ions (e.g. PbS or CdSe).

Besides binding affinity, additional requirements for the incoming ligand include: solubility of the incoming ligand, and low chemical reactivity with the original ligand. Ideally, the new ligand will be soluble both in the "free", unbound form, and in the "bound" form as part of the nanocrystal-ligand complex.

Solution-State Ligand Exchange *Solution-state ligand exchange* is a versatile method of SC-NC functionalization. Generally, a solution of natively-functionalized SC-NCs is exposed to a solution of a replacement ligand, and the mixture is stirred and/or heated to induce exchange. After sufficient interaction time, exchanged SC-NCs are precipitated through addition of a non-solvent and/or centrifugation, excess soluble ligand is drawn off, and the exchanged nanocrystals are resuspended in fresh solvent. This series of precipitation/resuspension steps is often repeated several times to achieve purification. Key parameters for the exchange process are: concentrations of the SC-NC and ligand solutions, mixing time, and temperature.

The chief benefit of the solution-state exhange method is that SC-NC functionalization is not limited by the requirements of synthesis. In principal, any molecule that can displace the original ligand, and result in a stable nanocrystal-ligand complex, can be utilized. This method also takes full advantage of the benefits of solution-phase chemistry. In particular, solution-stable SC-NCs can be purified and characterized through the diverse array of wet chemical techniques.

One limitation of the solution-state ligand exchange method is the requirement that the new nanocrystal-ligand complex be a soluble species. Short-chain ligands, with reduced steric bulk relative to the native ligands, can be limited in their ability to solvate the SC-NC core. Cross-linking ligands, which can potentially bind to more than one SC-NC core, can induce agglomeration and disrupt solubility. The issues affecting solubility are discussed in more detail in the following subsection.

Enabling complete reaction of the natively-capped SC-NCs with the exchange ligand can sometimes be challenging. Maximum interaction is achieved in a single-phase mixture, but this method requires similar solubilities of the reactants. Often times, this restriction is at odds with the desired functionality of the exchange ligand. Additionally, the single-phase mixture can create complications during separation and purification. Finding a suitable non-solvent that precipitates the desired product, but not the free ligand or starting material, can be challenging because of the similarities in miscibility.

An alternative approach is a *biphasic* solvent system in which the natively-capped SC-NCs are suspended in one layer, and the exchange ligand dissolved in the other[38]. This method has the added benefit of separating starting material and product into two separable layers. As ligand exchange proceeds, SC-NCs are drawn into the product layer, enhancing the speed and completion of reaction. The challenge of this method lies in generating sufficient mixing of the two immiscible solvent layers such that ligand exchange proceeds at a reasonable rate. Vigorous, chaotic mixing is therefore desirable to achieve maximum contact between the reactants.

One final complication of the solution-phase method arises from poor solubility of partially-exchanged SC-NCs. This scenario most typically arises in biphasic exchange systems and is the result of a mixed ligand shell of intermediate polarity. This complication can sometimes be remedied through adjustment of the SC-NC and ligand concentrations and reaction times. In some cases, more complete removal of the native ligand shell can also be facilitated through the use of certain metal ions, which aid transfer of the exchange ligand to the nanocrystal surface[39].

Solid-State Ligand Exchange One final method for SC-NC functionalization is *solid-state ligand exchange*, and it is specific to the use of SC-NCs in the

solid-state, thin-film form[40,41,42,43]. The main goal of this method is typically to tune the morphology of a SC-NC thin film for adjustment of optical and/or electronic properties, through either: 1) decreased particle spacing, or, 2) increased organizational order. Solid-state exchange can also be used to affect passivation of SC-NC surfaces[44]. Generally, a pre-fabricated thin film of as-synthesized SC-NCs is subjected to either chemical or thermal treatment to fully or partially remove the native ligand shell, and either replace it with another desired chemical species, or else remove it entirely to leave a bare nanocrystal surface.

The main benefit of the solid-state exchange approach is that it skirts the requirement of solubility for the resulting nanocrystal-ligand complex. This makes the method extremely useful for the preparation of SC-NCs functionalized with short-chain, cross-linking, or otherwise insoluble ligand shells. Solid-state exchange is, thus, most used for preparation of SC-NC thin films where electronic conduction is a concern, and dense nanocrystal arrays can not otherwise be achieved.

One drawback of this method is the potential for introducing unintended defects into the SC-NC film. Removal of native, long-chain ligands from a pre-formed film leave voids that cannot be fully compensated by the smaller incoming ligands. If enough native ligands are replaced, the resulting stress can lead to film cracking. Although cracks can sometimes be filled through additional overcoating steps, the result is not always optimal. Additionally, solid-state-exchanged films are difficult to purify. Whereas other ligand exchange methods maintain the full toolbox of solution-state purification methods, solid-state exchanges rely almost solely on solvent washes to remove impurities or excess ligands. Finally, solid-state exchanges are also more susceptible to incomplete exchange due to a reduced interface with the ligand solution.

This can be especially troublesome in thick films, where SC-NCs buried at the bottom of the stack might have limited contact with the incoming ligand.

Another variation on the solid-state exchange method is layer-by-layer (LbL) deposition. This method also relies on ligand exchange of a pre-deposited SC-NC film, and will be discussed in greater detail in the following section.

1.4.2. Effects of Surface Functionalization on Solubility and Stability

SC-NC surface functionalization has a large effect on the solution stability of nanocrystal suspensions. There are three major factors which affect stability of SC-NC solutions: 1) solubility in the selected solvent, 2) resistance to agglomeration, and, 3) resistance to decomposition pathways (e.g. ligand desorption or oxidation). All three of these factors are directly influenced by composition of the SC-NC ligand shell.

As with any chemical species, solubility of SC-NCs is determined by the interactions of the solute with the solvent. Bare nanocrystal cores are typically insoluble in most solvent systems, requiring the presence of a bound organic ligand shell to aid in suspension. The length and composition of the ligand shell, therefore, governs the solubility of SC-NCs. Long ligand chains extend out farther from the particle surface allowing for increased solvation relative to short ligand chains. Rigidity of the ligand backbone plays a factor, with ligands composed of saturated alkane chains allowing greater solvation than those with aromatic or unsaturated backbones[45]. Additionally, ligand packing density, branching, and tail group composition all affect interactions with the solvent. The compatibility and miscibility of the solvent with these ligand features ultimately determine solubility.

SC-NC surface functionalization also affects susceptibility to agglomeration. In general, increased steric bulk of the ligand shell will make SC-NCs more resistant to agglomeration and/or precipitation[46]. Long-chain, densely-packed, and highly-branched ligand shells have all been shown to increase the solution stability of SC-NCs. Additionally, the use of charged ligand shells can reduce agglomeration via electrostatic repulsion. Charges can be incorporated through tethering of either ionic or ionizable ligand functional groups (e.g. covalently-bound sulfonate, ammonium, or carboxylate groups) to the ligand backbone[38]. Ionic functional groups exist as an ion pair, with one ion tethered to the ligand backbone, and its oppositely-charged counter ion bound throuch electrostatic attraction. Solubilization of the counter ion separates the ion pair and generates a remnant electrostatic charge on the SC-NC ligand shell, which in turn, keeps particles separated in solution through electrostatic repulsion. Thus, the method of electrostatic stabilization does not require bulky ligand backbones, but is only effective in polar media, e.g. water, and only within certain ranges of pH and ionic strength that allow for significant separation of ionic charges. Ultimately, electrostatic and steric repulsion methods maintain inter-particle separation through ligand/ligand interactions, and it is this separation that govern agglomeration rates.

The inherent lability of ligands that prove optimal for SC-NC synthetic preparations, also make these molecules prone to desorption from the nanocrystal surface. Studies have shown that solutions of SC-NCs contain a natural equilibrium between "bound" ligands – tethered to the particle surface – and "free" ligands – floating uncoordinated in solution[47]. Purification steps used during synthetic workup of SC-NCs often involve washings with pure solvents. Due to the bound/free ligand equilibrium, however, these solvent rinses can deplete the concentration of

free ligands. Equilibrium forces then draw replenishment by stripping bound ligands off the nanocrystal surface. If enough surface ligands are removed, this process can eventually cause precipitation of the de-ligated SC-NCs.

Certain ligand functional groups are susceptible to oxidation, which can impact their affinity for binding to SC-NC surfaces, and lead to particle precipitation after excessive ligand desorption. In particular, strong, thiolate ligands (deprotonated thiols) have been shown to undergo reaction with molecular oxygen to form weak-binding disulfides[45,48,38]. Once oxidized to disulfides, coordination to the nanocrystal surface is weakened, leading to ligand stripping and eventual nanocrystal agglomeration and/or precipitation. Ligands with other head groups, such as carboxylic acids and amines, have proven more resistant to oxidation and more exotic ligands have also been investigated for concerns about air stability[49,50]. Additionally, increased ligand packing density around the SC-NC core seems to impede oxidative decomposition, presumably through protection of either the nanocrystal surface or ligand head group from reaction with molecular oxygen[45]. Use of ligands with long-chain and/or straight alkane backbones, as well as highly branched dendrimer ligands, has been associated with increased stability to oxidation[51].

Oxidation can also lead to an alteration of SC-NC core properties. For example, oxidation can result in irreversible chemical transformations of surface atoms, leading to core etching or deposition of a surface oxide layer atop the SC-NC core[45]. Either of these processes will cause an effective shrinking of the SC-NC core, which in turn will alter any optical and electronic properties associated with the electronic band gap. For example, core oxidation can induce a "blue-shift" of the optical exciton peak to higher energies and shorter wavelengths[45]. Oxide outer layers are also associated with increased electron trapping and device noise in SC-NC thin films, both of which

can have detrimental effecs on SC-NC device performance[8]. Robust ligand shells are therefore important to maintain the desired properties of SC-NCs.

1.4.3. Effects of Surface Functionalization on SC-NC/Biological Interactions

Appropriate choice of ligand can be utilized to make SC-NCs soluble in aqueous systems so as to be compatible with biological environments. Additionally, SC-NCs can be "decorated" with a variety of bioconjugates, antibodies, etc. that allow specific targeting of cellular structures, for biolabeling or fluorescent imaging[4]. This application, which demands close interaction of SC-NCs with potentially sensitive biological targets, has led to a natural interest in understanding their toxicology.

Since the early days of nanomaterial research, there has been concern that these novel materials may pose adverse risks to human health and the environment. At the heart of these concerns was the unique size regime that these materials inhabit (1 - 100 nm). Particles of this scale are amenable to a wider variety of cellular uptake mechanisms, increasing the exposure concern that nano-sized particles might have greater bioavailability[52]. Also, SC-NCs, like all nanomaterials, are governed more strongly by their interfaces than macroscopic objects. Reactive surface atoms on SC-NCs might facilitate potentially damaging chemical reactions in ways that bulk materials do not.

Many of these concerns have been borne out – SC-NCs *do* exhibit toxicity profiles different from the bulk materials, and smaller particles tend to be more toxic than larger ones[53,54]. However, the overall picture has proven more complicated. Plenty of SC-NCs exhibit no harmful effects, and more is being learned about how to make nanomaterials safer every day. Nanotoxicology remains an increasingly active area

of research, and likely will remain that way for years to come. Following is a brief overview of some of the known factors governing SC-NC toxicity.

Many of the factors that influence SC-NC susceptibility to oxidation – e.g. labile ligands and access to the core – have also been implicated in SC-NC toxicity to biological systems. One of the main factors governing SC-NC toxicity is the composition of the core. Many of the more technologically relevant SC-NCs contain heavy metals or other toxic elements, e.g. CdSe, PbS, InAs, etc. There are two competing theories for what causes the toxic response from exposure to some SC-NCs. In one model, toxic metal ions are etched from the SC-NC surface via passive or targeted oxidative decomposition processes, which then go on to cause oxidative stress or other forms of cellular damage. In another model, SC-NC cores, themselves, act as the source of toxicity. Bare SC-NC surfaces are thought to act as centers of free radical formation and oxidative stress, due to their known ability to photooxidize organic molecules[55]. In both mechanisms, however, exposure of the SC-NC core is the key factor governing toxicity. SC-NCs with surface functionalizations that encapsulate, or otherwise sequester the particle surface, therefore, tend to exhibit lower toxic responses[55]. Additionally, there is considerable drive to develop so-called, "green-by-design" materials that replace toxic elements with more benign ones, while still maintaining the desirable properties of the original materials[56,57,58].

Core composition of SC-NCs is clearly not the only factor governing nanotoxicity. There are a number of nanomaterials composed of seemingly benign materials, (e.g. Au) that nontheless exhibit toxic responses[59]. In these systems, it is the ligand shell, itself, that is culpable for the deleterious effects. The cellular mechanisms governing the toxic response to ligand shell functionality is even less understood than those

involved in core toxicity[60]. Ongoing studies will hopefully shed some light on these effects.

Surface functionalization also has a strong influence over the organization and packing density of SC-NCs in solid-state thin films. These effects will be discussed in greater detail in the following section.

1.5. Thin Films of Semiconductor Nanocrystals – Preparation and Properties

Some of the more promising applications of semiconductor nanocrystals – especially the lead chalcogenides – involve their use in photonic devices. This class of electronic devices include, but is not limited to, light-emitting diodes (LEDs), photodetectors, and photovoltaics. All three of these devices rely on solid-state materials to form the basis of their function. Considerable effort, therefore, has been put into understanding how SC-NCs organize themselves in the solid state. In particular, there has been an interest in how SC-NCs can be fabricated into high-quality thin films.

1.5.1. Fabrication of SC-NC Thin Films

SC-NC thin films can be fabricated using standard coating methods including, drop-casting, dip-coating, and spin-coating. There are also reports of less-common techniques such as chemical aerosol and electrophoretic deposition methods. The desired film properties (e.g. thickness, roughness, etc.) will, in part, determine the coating method. Spin-coating is a common technique whereby a nanocrystal solution is deposited atop a desired substrate, and then spun at high speeds to induce quick drying and removal of excess material[61]. Spin speed, solution concentration, and

solvent surface tension and viscosity are but a few of the factors influencing film quality[61]. Under the proper conditions, spin-coating can produce high-quality, glossy films, with low defect densities.

Another increasingly common method of SC-NC thin-film fabrication is layer-by-layer (LbL) deposition[62]. In this method, thick films are built up piecemeal – an initial thin layer of SC-NCs is first deposited via dip or spin coating from a dilute nanocrystal solution, then insolubilized through exposure to a cross-linking or short-chain ligand solution. The insolubilizing agent must efficiently replace the original ligand, so it must either have a stronger binding strength to the nanocrystal surface, or else be competitive enough with the original ligand that excess concentrations will drive the equilibrium towards replacement. Additionally, the insolubilizing agent must be soluble in the free form, yet not induce solubility of the SC-NC in the bound form. Once the first SC-NC layer is insolubilized, subsequent layers can be built up through alternating dips in SC-NC and ligand solutions.

SC-NC thin films have also been studied as part of multi-component systems. One type of system includes multilayer sandwich devices, where additional interfaces are made by depositing a layer of SC-NCs adjacent to other semiconductor layers (e.g. a conjugated polymer) in a vertical arrangement, to create a planar heterojunction. The geometry of heterojunctions need not be planar, and formation of so-called "bulk heterojunctions" through blending of SC-NCs with semiconducting, conjugated polymers, has also been an active area of study.

The electronic properties of SC-NC thin films lend themselves for use in a wide variety of applications. But first, the underlying physics governing charge transport in these materials is discussed.

1.5.2. Charge Transport in SC-NC Thin Films

The electronic transport properties of SC-NC thin films are governed by two main factors: 1) the electronic structure of its individual SC-NC components, and 2) the organization of the nanocrystals within the film. With regards to the electronic structure, size dispersity and ligand energy levels (or barrier height) are two properties that influence the ensemble behavior of SC-NCs. Organizational structure is primarily influenced by inter-particle separation (or barrier width) and packing order. All of these parameters are, at least in part, governed by the composition of the nanocrystal ligand shell.

Thin films of SC-NCs can be conceptually envisioned as a series of conducting nanocrystal islands surrounded by a sea of insulating ligands. To have an electronic charge travel through the film, it must traverse the inter-nanocrystal distance and "hop" from particle to particle. This transport is primarily a tunneling mechanism, and the rate of tunneling (Γ) can be expressed as:

$$\Gamma \approx exp\{-2(2m^*\Delta E/\hbar^2)^{1/2}\Delta x\} \qquad \text{(Equation 1.2)}$$

where m^* is the electron effective mass, $\hbar$ is the reduced Planck's constant, and ΔE and Δx are the height and width of the tunneling barrier, respectively[63]. From this relationship, we can see that the tunneling rate decreases exponentially with an increase in the inter-nanocrystal separation, and it has a slightly weaker dependence on the barrier height and the effective mass. The tunneling rate can therefore be enhanced through the use of short-chain ligands that minimize the separation between nanocrystals[64,65] and, to a lesser extent, with conjugated ligands that offer lower

barrier heights to conduction[66]. This concept is sometimes discussed in terms of the *coupling energy* (β), where $\beta \approx h\Gamma$, and h is Planck's constant[63].

Another factor governing charge transport in SC-NC thin films is the Coulombic *charging energy* (E_c), which is the energy cost of placing an additional electronic carrier into a nanocrystal. It can be expressed as:

$$E_c = \frac{e^2}{4\pi\varepsilon_m\varepsilon_0 r} \qquad \text{(Equation 1.3)}$$

where e is the elementary electron charge, ε_m is the dielectric constant of the surrounding medium (i.e. that of the ligand shell), ε_0 is the permittivity of vacuum, and r is the nanocrystal radius[63].

The charging energy represents a barrier to charge transport. If $\beta > E_c$, then the charging energy is overcome and electronic charges can move freely through the film. This change in behavior is known as the Mott metal-insulator transition[63].

The other main factor governing charge transport in SC-NC thin films is disorder ($\Delta\alpha$). Two types of disorder exist in SC-NC thin films – one is caused by the dispersity in nanocrystal size, and the resulting distribution of energy levels, for particles in the film, and the other is caused by variations in nanocrystal packing within the film[63]. Electronic charge transfer between two SC-NCs is most efficient when their energy levels are the same. When variation in particle size creates a dispersion in the energy levels, charge transfer can only occur in conjuction with the absorption or emission of phonons. Thus, uniformity in size and shape of SC-NCs is important for thin-film charge transport. Additionally, control over packing organization in SC-NC thin films is another method of improving transport properties. Ordered nanocrystal arrays – or, superlattices – exhibit reduced disorder due to increased orbital overlap between nanocrystals. SC-NC ligand structure is one of the key factors influencing formation

of superlattices. For example, the organized stacking of long-chain alkyl ligands has been found to encourage superlattice formation, although at the cost of increasing nanocrystal separation[63].

The interplay and variation of the β, E_c, and $\Delta\alpha$ energies determine the conduction mechanism for a particular SC-NC system. Often times, this mechanism will also change based on the temperature[63]. In films of SC-NCs utilizing bulky ligands with large inter-nanocrystal separations, "nearest-neighbor" hopping is often seen. In other materials, denser packing[67] and electrochemical doping[68,69] have resulted in films demonstrating *variable range hopping* (VRH). In VRH, a hopping electron finds an optimal path with the lowest activation barrier, which, depending on temperature, is not always a nearest neighbor. As with the individual components of transport, conduction mechanisms in SC-NC thin films are dominated by inter-crystal separation and packing order, which in turn, are governed by the ligand shell.

1.5.3. Applications of SC-NC Thin Films

The optical and electronic properties of SC-NC thin films make them potential candidates for use in photonic devices. Low fabrication costs, due to their solution processability, and their compatibility with flexible substrates make SC-NC thin films a viable alternative to replace traditional materials in existing applications, and enable advancement of new technologies. Despite their promise, SC-NC-based devices are still limited by their poor charge transport properties relative to bulk crystalline devices.

Heterojunctions (see Figure 1.4) are sometimes called donor/acceptor interfaces and can be useful for the design of photonic or purely electronic devices. Their utility comes from energy offsets afforded by the relative energy levels of the respective

bands, and can be used to improve charge carrier separation (or exciton dissociation), to impose unidirectional current flow (or rectification), amongst other things. Bulk or planar heterojunctions composed of SC-NCs and conjugated polymers are often affected by many of the same factors that govern nanocrystal-only thin films.

Following is a brief overview of recent progress in the field of SC-NC-based photonic devices.

Photovoltaics In its most simple configuration, a photovoltaic (PV) device consists of one or more semiconductor materials sandwiched between two metal electrodes. When light is absorbed by a PV device, excitons are *generated* within the semiconductor material. Excitons are *separated* into free carriers, which are then *transported* to the electrodes, and finally *extracted* at the semiconductor/metal interface. To generate a photocurrent, electrons need to be delivered to one electrode, and holes to the other. This unidirectional current flow can only occur through the presence of some form of asymmetry in the device. This asymmetry can take the form of a junction – e.g. at the interface of p-type and n-type regions within the semiconductor – or through an offset in the work functions of the metal electrodes[10]. The efficiency of a PV device is ultimately governed by the relative rates of its four components: *exciton generation*, *exciton separation*, *charge transport*, and *charge extraction*.

The use of SC-NCs in PV devices comes primarily from their potential to increase the efficiency of exciton generation. An important attribute of PV devices is the degree of spectral overlap between the solar radiation spectrum and the absorption spectrum of the active material in the device. As a black-body radiator, the sun emits a wide bandwidth of light from the ultra-violet into the infrared[10]. To maximize photon collection, a photovoltaic material must be sensitive to as wide a range of this

light as possible. This condition can be met with a semiconductor of an infinitely small band gap, or a metal. However, it is not just the *number* of collected photons that determines the power conversion efficiency of a PV device. Energy from light is transferred to the semiconductor and stored in the form of an exciton. Energy in excess to that of the band gap is lost through thermal vibrations and the remaining potential energy of the exciton is equal to that of the band gap. To maximize the potential energy of each exciton, a material with an infinitely large band gap is required. Thus, to maximize the output power of a PV device, a balance must be struck between the *number* and the *energy* of the photogenerated excitons. This balance can be achieved through careful tuning of the semiconductor band gap.

Thin films of SC-NCs, especially those of PbS and PbSe, have been explored for use as photovoltaic (PV) materials. The band gaps of bulk PbS and PbSe lie within the mid-infrared region of the electromagnetic spectrum, however, quantum confinement allows tunability throughout the near-infrared (NIR). For a single junction device, a band gap energy of 1.13 eV is optimal for maximum power output from solar radiation[7]. This energy lies in the heart of the NIR, and is easily accessible through proper size tuning of PbS or PbSe nanocrystals.

The main limitation to SC-NC-based PV devices is their poor charge transport properties relative to single crystal-based devices. Charge transport is primarily influenced by inter-particle separation, and thus, ligand composition. The dependence of photovoltaic device efficiency on ligand chain length has been verified by a variety of groups[70]. Additionally, the nature of the ligand head group has been shown to have an effect. Thiols have been shown to passivate recombination centers in PbS-NC thin films, which can improve the efficiency of photovoltaic devices[44].

The large surface area-to-volume ratio of SC-NCs make them amenable to bulk heterojunction structures. The efficiency of exciton separation and charge transport in bulk heterojunction films is highly dependent on film morphology. Optimal separation occurs with maximum interfacial area between the SC-NC and polymer materials; however, efficient charge transport requires continuous paths through each of the materials to their respective electrodes. The optimized morphology – a co-continuous, interpenetrating network – balances the two requirements of maximum interface and uninterrupted path to the electrode. Morphology of bulk heterojunctions can be controlled through concentrations of the two components and solvent choice during deposition. Additionally, use of branched nanocrystals and other shape control methods have been explored for improving the interfacial area between the SC-NC and polymer layers[21].

There have also been attempts to harness the process of multiple exciton generation (MEG) to increase power conversion efficiencies in SC-NC-based PVs. MEG allows for the potential capture of multiple excitons per absorbed photon, and thus, in principal, could allow conversion efficiencies exceeding the Shockley-Queisser limit[16]. To date, no photovoltaic device has approached this limit – max efficiency ∼66 % in a uniform device of infinite layers perfectly matched to the solar spectrum[16]. Despite this, there has been a report of observing the contribution of MEG in photovoltaic devices based on PbS-NCs[71].

Photodetectors A photodetector is a device designed to detect light in the form of an electrical response. Like photovoltaic devices, the geometry of a photodetector device can be as simple as a semiconductor sandwiched between two metal electrodes[10]. One form of photodetector – a *photodiode* – includes a junction to aid in separation of photogenerated excitons, which can operate

much like a PV device, i.e. generating a photocurrent without an applied bias. Another type of photodetector is based on a *photoconductor*, or a material that changes its conductivity with response to light. Because the primary function of a photodetector is simply to detect light and not to generate power, photoconductive photodetectors are often biased to improve sensitivity to light and signal-to-noise ratios. Photoconductors are also of simpler construction than photodiodes – they do not require formation of a junction or dissimilar electrode materials – and can exhibit values of *gain* greater than unity. The subject of photoconductivity and gain is discussed in greater detail below and in the following section.

There are three main parameters that determine the performance of a photodetector: 1) the quantum efficiency and gain, 2) the response time, and 3) the sensitivity (or detectivity)[10]. The quantum efficiency (η) is defined as the number of carriers – electrons and holes – generated per incident photon. It can be expressed as:

$$\eta = \frac{i_{ph}}{e}\left(\frac{h\nu}{P_{opt}}\right) \qquad \text{(Equation 1.4)}$$

where i_{ph} is the photocurrent, e is the elementary charge, $h\nu$ is the energy of a photon, and P_{opt} is the incident optical power[10]. A quantum efficiency of unity means that every incident photon creates a free carrier that contributes to the photocurrent. Photons that do not generate free carriers (e.g. due to reflection or scattering) or generate excitons that do not contribute to the photocurrent (e.g. due to recombination), lead to reductions in the quantum efficiency[10]. Another common metric is the responsivity (R), which is generally expressed in units of A/W:

$$R = \frac{i_{ph}}{P_{opt}} = \frac{\eta e}{h\nu} = \frac{\eta\lambda(\mu m)}{1.24} A/W \qquad \text{(Equation 1.5)}$$

where λ is the wavelength of incident light measured in microns[10]. The distinction between η and R is that η references the photocurrent to the *number* of incident photons, while R references the photocurrent to the *power* of illumination. The photocurrent can be further amplified through *gain* mechanisms, which are discussed in greater detail in the section on photoconductivity.

The *sensitivity* defines the lowest optical signal that can be measured by a photodetector, and it is influenced by the magnitude of the photocurrent as well as the noise in the device[10]. Noise is an inherent property of any electronic device and sets a lower limit on the level of light that can be detected; thus, it is the *signal-to-noise* ratio that determines the sensitivity. Noise can come from many sources. Noise can originate from external sources, such as background radiation or from internal sources, such as fluctuations in current flow due to temperature – as in the case of Johnson noise, or due to the discrete nature of electronic charge carriers and the statistical distribution of their flow through a material – as in the case of shot noise[10]. In general, noise in a photodetector increases with the gain and the dark current density.

The smallest light power that can be distinguished above the noise level is called the *noise equivalent power* (NEP)[10]. A related metric – the *detectivity* (D^*) – normalizes NEP for the device area, and allows direct comparison between photodetectors of different geometries. It can be expressed as:

$$D^* = \frac{\sqrt{AB}}{NEP} \qquad \text{(Equation 1.6)}$$

where A is the device area, and B is the electrical bandwidth – often measured at 1 Hz. The greater the value of D^*, the higher the sensitivity of the photodetector.

The response time of a photodetector is governed by the lifetime of excited carriers. Techniques used to increase gain and sensitivity in photodetectors generally increase the lifetime of excited carriers, and thus lead to slower response times. Balance must, therefore, be reached between response time and sensitivity for a particular application. This interplay between response time and sensitivity is discussed in greater detail on the section on photoconductivity.

SC-NC thin films have been studied for use as photodetectors, especially nanocrystals of the lead chalcogenides: PbS and PbSe. As previously discussed, the band gaps of PbS and PbSe nanocrystals can be size-tuned across the NIR. NIR photodetectors are important from a technological point of view for use in optical fiber systems used in the telecommunications industry and for night-vision applications[72]. Like all SC-NC thin film applications, NIR photodetectors can benefit from the low production costs associated with solution-processing and their amenability to flexible or curved substrates. Photodetectors based on PbS-NCs have also shown performance values rivaling, and in some cases surpassing, that of devices based on traditional materials. Sargent et al. have demonstrated gains of up to 10^4 and detectivities of up to 10^{13} Jones in the NIR for PbS-NC-based detectors[8,72].

Light Emitting Diodes (LEDs) In addition to their electrical response to light, SC-NCs are also desirable for their emission properties. SC-NCs composed of direct band-gap materials can exhibit very efficient photoluminescence (PL), in some cases with internal quantum efficiencies approaching unity. Fluorescence occurs from relaxation of photoexcited electrons through radiative recombination with its hole partners, emitting light of energy and wavelength equal to the band gap.

The bandwidth of emitted light from SC-NCs is typically quite narrow relative to comparable chromophores such as organic dyes. The broad excitation spectrum coupled with a narrow emission spectrum make SC-NCs ideal for PL applications such as biological imaging agents[73]. "Spectrally-pure" emission is also highly desirable for solid-state, light-emitting diodes (LEDs)[3]. Pixelated displays, composed of many subpixels of red, green, and blue emitters are often limited by the color purity of its components, and SC-NCs have been investigated to meet this design challenge.

From a simple, conceptual point-of-view, LEDs can be thought of as a photovoltaic device operating in reverse. Rather than absorbing light and generating a photocurrent as in PV devices, LEDs emit light under external power. As such, LEDs are sensitive to many of the same factors that govern performance in photovoltaic or photodetector devices, namely charge injection/extraction and charge transport. LEDs often employ multiple layers of materials to create heterojunctions – e.g. pn junctions or donor/acceptor interfaces – to improve rates of radiative recombination of injected electrons and holes. A unique requirement to LEDs is that of *charge balance* between injected electrons and holes – maximum emission efficiency is achieved when the number of electrons and holes is equal and recombination occurs near the center of the device[10].

LEDs based on SC-NCs generally use a monolayer of nanocrystals as the emissive layer, with other conductive materials (e.g. semiconducting polymers) as electron and hole "blocking" and/or "transport" layers to achieve charge balance[74,2]. Nanocrystal-only devices typically have much lower emission efficiencies due to higher rates of nonradiative recombination and/or poor charge balance[2]. Additionally, bulk heterojunctions structures have been explored for improving the performance of SC-NC-based LEDs[75,76].

1.6. A Deeper Discussion of Photoconductivity

One of the most promising applications of PbS-NCs involve their use in thin-film photodetection or photovoltaic systems. To better understand the potential advantages and disadvantages of the replacement of convential bulk semiconductors with nanomaterials, a closer look at the physical processes at work in these devices is warranted. In particular, photoconductivity is examined in greater detail. As is the case for most properties of SC-NCs, photoconductivity in SC-NC thin films arises from similar physical processes to those seen in bulk semiconductors. As an initial point of reference, therefore, the manifestation of photoconductivity in bulk materials, will first be described, with any deviations due to nanocrystallinity pointed out where needed.

Photoconductivity is the phenomenon of an increase in the conductivity of a material in response to illumination[11]. This behavior emanates from the excitation of electrons in a material by light. Thus, to exhibit photoconductivity, a material must first be sensitive to light, i.e. the available energy levels of the material must be such as to allow absorption of energy equal to that of the incident photons. Semiconductors are particularly suited for this behavior due to their electronic band structure. In intrinsic semiconductors, the valence and conduction bands are separated in energy by the electronic band gap, which corresponds to the energy of light spanning the UV, visible, and infrared regions. The bands, themselves, are composed of closely spaced energy levels forming a continuum of states. Electrons can be excited from the filled levels of the valence band as long as they absorb enough energy to reach beyond the forbidden energy region between the bands, and into a vacant state in the conduction band. These features allow a semiconductor to absorb a broad spectrum of light, with the electronic band gap energy acting as the lower limit.

The conductivity of a semiconductor can be expressed as:

$$\sigma = e(n\mu_n + p\mu_p) \qquad \text{(Equation 1.7)}$$

where e is the electron charge, σ is the conductivity, n and p are the densities of free electrons and holes, respectively, and μ_n and μ_p are the elecron and hole mobilities[11]. Excitation of electrons due to absorption of light creates an increase in the free carrier density of the material. This leads to the following expression for the change in conductivity, or photoconductivity:

$$\Delta\sigma = e(\Delta n\mu_n + \Delta p\mu_p) \qquad \text{(Equation 1.8)}$$

The photoconductivity can also be expressed in terms of the free carrier lifetimes for electrons (τ_n) and holes (τ_p):

$$\Delta\sigma = fe(\mu_n\tau_n + \mu_p\tau_p) \qquad \text{(Equation 1.9)}$$

where f is the number of electron-hole pairs generated per second per unit volume of the semiconductor[11].

In semiconductors, photoexcited electron-hole pairs are initially bound through Coulombic forces as excitons. The energy required to separate the electron-hole pair into genuine free charge carriers is called the exciton binding energy. In SC-NCs, this binding energy can be quite high due to the confinement of the exciton to the relatively small region of the nanocrystal core, and barriers at the surface that inhibit transfer to adjacent particles. Efficient separation of excitons in SC-NCs therefore relies on close, organized packing of nanocrystals and efficient orbital overlap between adjacent

particles. Uniformity of SC-NC size and shape also improves exciton dissociation through reduction of site energy disorder[63].

It is often desirable to quantify how responsive a semiconductor is to light. One way of defining this quantity is as the number of charge carriers which pass between the electrodes per unit time for each photon absorbed; this ratio is called the gain G[11]. The gain can be related to the photocurrent (i_{ph}), which is the increase in current due to illumination, and can be expressed as:

$$i_{ph} = \eta e N_\lambda G \qquad \text{(Equation 1.10)}$$

where η is the number of electron-hole pairs generated per absorbed photon and N_λ is the number of photons of wavelength λ absorbed in the material per unit time[63]. Here, it is clear that the gain is a measure of efficiency. A gain of unity means that every photogenerated charge carrier is extracted at the electrode, while a value of less than one represents a reduced extraction efficiency. Gain values greater than unity can also be achieved. To see how this can occur, the gain can be expressed as a function of the free carrier lifetimes:

$$G = \frac{\tau_n}{t_n} + \frac{\tau_p}{t_p} \qquad \text{(Equation 1.11)}$$

where t_n and t_p are the transit times for electrons and holes, respectively[11]. The transit time reflects how long it takes a charge carrier to move between the electrodes, and is a function of the distance between electrodes (L), the applied electric field ($\mathcal{E}$), and the mobility[11]. It can be expressed as:

$$t = \frac{L}{\mu \mathcal{E}} \qquad \text{(Equation 1.12)}$$

From Equation 1.11 we can see that improvements in gain can be had through two main routes: 1) increasing the carrier lifetimes – a process known as photosensitization, or 2) decreasing the transit times[72]. Equation 1.11 and Equation 1.12 can be combined and a new expression written for gain as:

$$G = (\tau_n \mu_n + \tau_p \mu_p) \frac{\mathcal{E}}{L} \qquad \text{(Equation 1.13)}$$

Imperfections in crystal structure can introduce new energy levels into the electronic structure of a semiconductor – so-called, *trap states*, or *traps*, see Figure 1.8. Impurity atoms, vacancies, dislocations, undercoordinated surface atoms, and surface oxidation can all manifest themselves as trap states[11]. In SC-NCs, traps often originate from the distinct chemical environment of surface atoms relative to that seen by atoms in the core. Traps in PbS-NC films, in particular, have been attributed to exposure to oxygen and the presence of a variety of surface oxidation states, e.g. $PbSO_4$, $PbSO_3$, and Pb-carboxylate[77,78].

Traps play an important role in photoconductive materials, specifically, through affecting gain. Trap states are spatially localized and typically have energy levels that lie within the forbidden band gap of the semiconductor[11]. Trap states also tend to exhibit different "capture cross sections" for electronic charge carriers based on their energetic position within the band gap. Traps that lie closer (but lower in energy) to the semiconductor conduction band will have a greater affinity for electrons – i.e. *electron traps* – while states that lie closer to the valence band (but greater in energy) will more likely act as *hole traps*. Traps that lie near the middle of the band gap – so-called, mid-gap states – can capture both electrons and holes, and will often function as recombination centers.

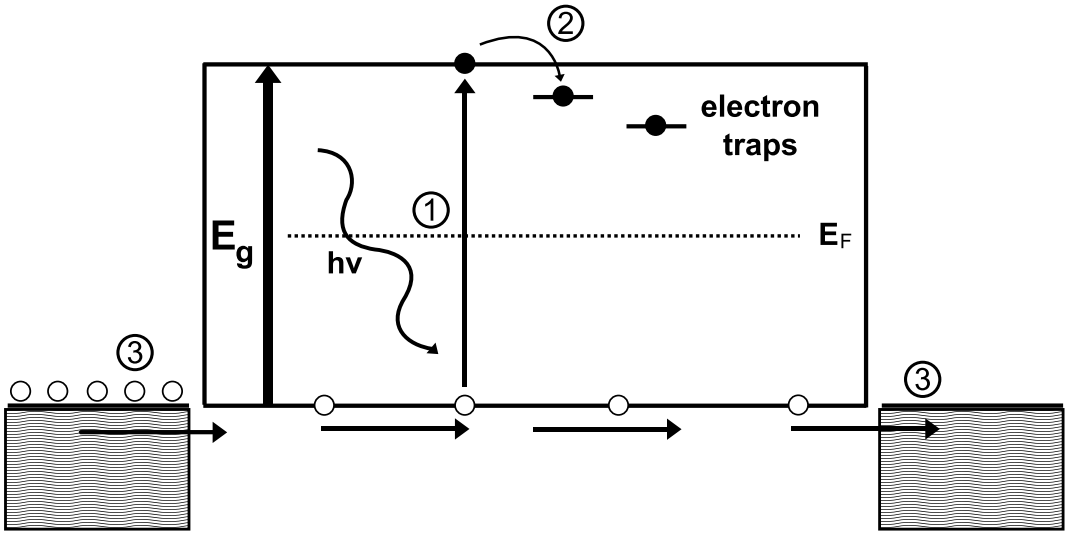

FIGURE 1.8. Effect of traps on photoconductivity. 1) Absorption of light excites an electron and generates an exciton. 2) Excited electron becomes trapped at a defect site. Recombination is suppressed and lifetimes of electrons and holes are increased. 3) The hole lifetime now exceeds the transit time. As holes are extracted at one electrode interface (*right*), they are replenished at the other electrode interface (*left*) due to an applied electric field.

Traps have the effect of extending the lifetime of the associated charge carrier. The difference in energy between a trap state and the nearest band edge determines the lifetime of a trapped charge carrier, and it is known as the trap "depth." *Deep* traps (those with a greater energy difference) will hold charge carriers longer than *shallow* traps, and result in longer lifetimes for the associated carrier. When traps are associated with the minority carrier, the increase in lifetime results in a greater value for the gain, as shown in Equation 1.11. Deliberate introduction of traps (e.g. through exposure to oxygen), can, therefore, be a technique to improve the photosensitivity of a photoconductor[11]. The improvement in the magnitude of the photoresponse comes at the cost of increasing the time constant, i.e. the on/off switching time is increased. This inherent trade-off between sensitivity and switching speed has profound implications for applications of photoconductors, e.g.

as photodetectors, where both parameters affect performance. In PbS-NC thin films, it has been shown that trap state depth (and thus, sensitivity and speed) can be engineered through simple chemical processing[78].

1.7. Summary

SC-NCs offer the potential for improving the performance of a variety of existing technologies based on: 1) their ease of synthesis, 2) the large degree of control over their composition and properties, 3) their ease of fabrication into high-quality thin films, and 4) their unique optical and electrical properties. Their incorporation into future applications will depend on the degree to which current research efforts succeed in addressing the factors limiting their performance, e.g. low charge transport efficiency in thin films. All of these issues will require greater control over SC-NC functionalization.

1.8. Chapter Overview

The primary focus of this dissertation is the effect that *ionic functionalization* has on the physical and chemical properties of lead sulfide nanocrystals (PbS-NCs). Following is an overview of the chapter organization of this document. Also detailed is the individual contributions of each co-author to this body of work.

1.8.1. Chapter II. Synthesis and Stability of Lead Sulfide Nanocrystals Functionalized with Short-Chain, Ionic Thiol Ligands

This chapter demonstrates how ionic groups can enable functionalization of PbS-NCs with two short-chain ligands – sodium 3-mercaptopropanesulfonate (MT) and sodium 2,3-dimercaptopropanesulfonate (DT) – via a stable, solution-phase, exchange

procedure. Despite a structural similarity, DT-functionalized PbS-NCs (PbS-DT) are more stable to oxidation than MT-functionalized PbS-NCs (PbS-MT). The relative stabilities are explained in terms of different binding modes to the nanocrystal surface (bidentate vs. monodentate) and oxidation pathways (intermolecular vs. intramolecular) for DT and MT ligands, respectively.

This chapter was previously published as: Moody, I. S.; Stonas, A. R.; Lonergan, M. C. "PbS Nanocrystals Functionalized with a Short-Chain, Ionic, Dithiol Ligand," *The Journal of Physical Chemistry C*, **2008**, *112*, 19383-19389. The bulk of the experimental work was performed by me. A. R. Stonas and M. C. Lonergan aided in experimental design and data analysis. The writing is mostly mine, with my co-authors providing overall editorial assistance and co-writing some portions.

1.8.2. Chapter III. Differential Stability of Lead Sulfide Nanoparticles Influences Biological Responses in Embryonic Zebrafish

Expanding on the stability study of Chapter II, this chapter investigates the exposure effects of PbS-MT and PbS-DT nanocrystals on biological systems. Interactions of nanomaterials with living systems is still poorly understood, with those of PbS nanomaterials even more rarely studied. Progress in this field has been hampered by a lack of well-characterized, water-soluble materials. Ionic functionalization, and the stability it lends to PbS-MT and PbS-DT nanocrystal solutions, make these materials an intriguing system in which to study bio-interactions. This chapter presents an *in vivo* study which expands upon the existing knowledge base through an examination of the toxicological effects of PbS-NCs on embryonic zebrafish. PbS-MT solutions were found to be relatively more toxic, and

PbS-DT nanocrystals less toxic to zebrafish. The differential toxicity and morbidity is tied to the relative stabilities of the nanocrystal solutions.

This chapter was previously published as: Truong, L.; Moody, I. S.; Stankus, D. P.; Nason, J. A.; Lonergan, M. C.; Tanguay, R. L. "Differential Stability of Lead Sulfide Nanoparticles Influences Biological Responses in Embryonic Zebrafish," *Archives of Toxicology*, **2011**, *85*, 787-798. The experimental work was performed either by myself, L. Truong, or D. P. Stankus. All material synthesis and characterization (except DLS measurements, which were performed by D. P. Stankus) were performed by me. All animal-related measurements were performed by L. Truong. The article was co-written between myself and L. Truong. All other co-authors provided editorial assistance.

1.8.3. Chapter IV. Mobile Ions Influence Charge Injection and Photoconductivity in Ionically-Functionalized Lead Sulfide Nanocrystal Thin Films

This chapter investigates the effects of ionic functionalization on the optical and electrical properties of PbS-NC thin films. Although ions are known to influence the behavior of electronic charge carriers in conjugated polymer devices, the effects of ions have been relatively unexplored in semiconductor nanocrystal systems. This chapter explores the effects that a change of counter ion has on PbS-DT thin-film photodetectors. Specifically, it is observed that films containing small counter ions (e.g. Na^+) exhibit increased dark conductivity and photoresponse with time under an applied bias, whereas, films containing larger (e.g. NMe_4^+) or multivalent (e.g. Ca^{2+}) counter ions do not show this behavior. These results are discussed in the context of a model of ion motion and ion-assisted injection at the PbS-NC / electrode interface.

This chapter is based on a manuscript in preparation for submission. It is written in the style of *The Journal of Physical Chemistry C*, and includes co-authored material (with M. C. Lonergan). The experimental work was performed entirely by me. The writing is entirely mine. M. C. Lonergan provided editorial assistance.

1.8.4. Chapter V. Concluding Summary

This chapter offers a concluding summary of all the results presented herein, and presents future outlooks on the role of ionic functionalization in SC-NC research. It is written in the style of *The Journal of Physical Chemistry C*.

1.9. Bridge to Chapter II

Chapter I provided a general overview of the unique properties of semiconductor nanocrystals, synthetic methods used for their preparation, and the optical and electrical properties of thin films prepared from them. In all of these subsections, a special emphasis was placed on the lead chalcogenide materials – including PbS-NCs – which form the subject of this document. More specifically, this dissertation will discuss the effects that *ionic functionalization* have on the physical, chemical, toxicological, and electrical properties of PbS-NCs. One of the challenges in the design of PbS-NCs for use in thin films is finding methods to bypass the use of bulky, long-chain molecules that offer proven control over nanocrystal synthesis and solubility. Post-synthetic functionalization with short-chain molecules can improve charge transport in PbS-NC thin films, but there are currently limited solution-based methods for their preparation.

Chapter II demonstrates how *ionic functionalization* can enable a solution-phase ligand exchange procedure for short-chain ligands. This chapter presents the

preparation of soluble PbS-NCs with two different short-chain, ionic, thiol ligands. Also included is an investigation into the relative stabilities of the two nanocrystal-ligand complexes, with a special focus on the difference in oxidative stability afforded by the two different ligands. Finally, a qualitative comparison reveals the improved optical and electrical performance of thin films of PbS-NCs functionalized with the new short-chain ligands relative to those capped with native, long-chain ligands.

CHAPTER II

SYNTHESIS AND STABILITY OF LEAD SULFIDE NANOCRYSTALS FUNCTIONALIZED WITH SHORT-CHAIN, IONIC THIOL LIGANDS

2.1. Introduction

The size-dependent optical properties of semiconductor nanocrystals (SC-NCs) have been an intense area of research for the last two decades. Development of versatile syntheses for SC-NCs using organometallic precursors have allowed fine control over nanocrystal size and dispersity, and result in well-defined optical and electrical behavior[1]. To attain such control, researchers have typically relied on long-chain organic ligands (e.g. oleic acid and trioctylphosphine) that reversibly bind to the nanocrystal surface and slow growth during the synthesis. Additionally, these ligands imbue the SC-NCs with solubility in organic solvents and act as a steric barrier to post-synthetic crystal growth, which can lead to agglomeration and precipitation[1].

The tunable and sometimes exotic electronic and optical properties of SC-NCs, along with the fact that they can be solution processed, has made them candidates for use in a wide variety of photonic devices, including light-emitting diodes (LEDs)[2], photodetectors[3,4], and photovoltaic devices[5,6,7]. Nanocrystals composed of the lead chalcogenides, PbE (E = S, Se, or Te), have been of particular interest due to the tunability of their band gap within the near-infrared (NIR) region of the

electromagnetic spectrum. Activity in the NIR region is important to the development of NIR photodetectors for telecommunications[8,4], and efficient photovoltaics that are well-matched to the solar energy spectrum[9,10].

Charge transport between nanocrystals is critical to many electronic and photonic applications of SC-NCs. Shorter ligands lead to reduced interparticle spacing, which reduces the energy barrier to charge tunneling between NCs. As such, reducing ligand chain length has been shown to improve the conductivity of doped and undoped nanoparticle solid films and the photoconductivity of such films by improving the efficiency of charge separation of photogenerated excitons.[11,12,13,14,4,15]. Relatedly, reduced interparticle separation has also improved the photovoltaic efficiency of pure nanoparticle films sandwiched between dissimilar contacts and nanoparticle / conjugated polymer hybrids.[3,6,9]

The reduced steric bulk of SC-NCs capped with short-chain ligands does, however, make them more susceptible to agglomeration and precipitation[16]. Because of this, short-chain ligands are often introduced as a surface treatment to preformed SC-NC thin films, to bypass any issues of solution stability. Surface-based exchanges can suffer from film cracking and incomplete ligand exchange[17], though, so a reproducible and stable solution-based exchange procedure is desirable.

The goal of the work presented herein is to investigate the dithiol sodium 2,3-dimercaptopropane-sulfonate (DT) as a ligand for PbS nanocrystals with the hypothesis that it would impart the greatest particle stability and solubility possible for such a short ligand. The DT ligand offers a number of structural features that were anticipated to offer distinct advantage. First, thiol exchange reactions are one-step post-synthetic treatments that take advantage of the strong metal-thiol interaction to replace existing ligands with ones incorporating desired functionality,

and have been previously utilized with PbE (E = S, Se, Te) NCs[18,19,20]. Second, the DT ligand incorporates an ionic sulfonate group. Use of a strong acid salt allows favorable interactions between the coated nanocrystal and a suitable polar solvent, with entropic forces driving the dissociation of ions and subsequent solvation of the anionic nanocrystal. Once dissociated, the charged ligand shell makes use of electrostatic repulsion to maintain interparticle spacing, and thus reduces agglomeration and increases stability. Ionic ligands have been previously used to stabilize gold nanoparticles,[21] and ionizable carboxylic acid ligands have been used to stabilize semiconductor nanocrystals.[22] Finally, DT is a dithiol ligand that is not prone to intramolecular disulfide formation. Studies on CdSe systems have shown that thiols are susceptible to oxidative decomposition – forming weakly coordinating disulfides in the presence of light and air – which leads to NC agglomeration and precipitation.[23] Perhaps contrary to expectations based on the chelate effect, semiconductor nanocrystals stabilized with certain dithiol ligands have been shown to be less stable to oxidation than similar monothiols due to intramolecular disulfide formation and reduced ligand density.[23] Previous stability studies with bidentate dithiol groups have focused on 1,3-dithiols, which are known to form five-membered 1,2-dithiolane rings via intramolecular disulfide formation.[23] It was anticipated that the DT ligand, a 1,2-dithiol, would be resistant to this decomposition pathway due to the instability of its intramolecular oxidation product. Intramolecular disulfide formation with DT would require the formation of a four-membered 1,2-dithietane ring, which have been rarely observed, and have been calculated to have high ring strain energies.[24]

Points of comparison are important in evaluating the role the DT ligand plays in improving interparticle electronic transport and particle stability. Transport through

DT-NC films are evaluated against widely studied oleic acid-capped PbS-NC films using an open-face interdigitated electrode geometry. Very few stability studies have been reported for PbE NCs[25,26]. To provide a suitable point of reference, NCs based on the monothiol sodium 3-mercaptopropanesulfonate (MT) are prepared, and their stability compared to PbS-DT NCs. These comparisons assess the promise of the DT ligand for stabilizing PbS-NCs for use in electronic and photonic devices.

2.2. Results

2.2.1. Synthesis and Characterization of Ionically-Functionalized PbS Nanocrystals

PbS nanocrystals functionalized with the DT ligand, or its monodendate analogue MT, were synthesized through a biphasic ligand exchange procedure performed on oleic acid-capped PbS-NCs (PbS-OLA). The PbS-OLA NCs were synthesized following the procedure of Hines and Scholes[27]. In a typical exchange, 5-15 molar equivalents of ionic ligand were dissolved in D_2O and mixed with a 25 mg/mL solution of PbS-OLA NCs in toluene. After vigorous shaking for ~1 hr, ionically-functionalized PbS-NCs (I-NCs), either DT-capped or MT-capped, were separated from the organic layer and rinsed with excess toluene to remove any remaining oleic acid. I-NCs were then purified through several precipitation/centrifugation steps (see Experimental). During all exchanges, NCs were kept under nitrogen atmosphere to prevent oxidation of the ligands or NC surface. Deuterium oxide was used in place of water to reduce effects of solvent absorption during post-exchange characterization by ^{1}H NMR and near-infrared absorbance spectroscopy.

Ligand exchange was initially observed as a visible migration of the dark-brown PbS-NCs from the toluene into the aqueous layer. The exchange process was further

monitored via ^{1}H NMR spectroscopy of the organic layer taken before and after ligand exchange. Ligands bound to the nanocrystal surface show broadened peaks in the NMR spectrum due to the geometrical constraints of being attached to the relatively bulky nanocrystal that tumbles slowly on the NMR time scale. Additionally, certain proton peaks of the bound oleic acid ligand shift slightly downfield from the free ligand. For instance, the vinylic protons shift from ∼5.6 ppm in the free form to ∼5.8 ppm in the bound form (in toluene-d8).

After exchange with either DT or MT, oleic acid peaks were observed to switch from the bound form to the free form, indicating that oleic acid had been liberated from the PbS-NC surface. ^{1}H NMR measurements taken on the aqueous layer after the exchange showed an absence of oleic acid peaks in the I-NC solution, confirming removal of oleic acid. Subsequent NMR measurements taken for the aqueous layer after each purification step confirmed removal of excess thiol ligand. Purified I-NC solutions showed no peaks in the ^{1}H NMR spectra. Presumably, the rotational freedom of the methylene protons is severely limited in the bound ligands resulting in severe peak broadening. The presence of DT or MT ligands was confirmed by FTIR spectroscopy on purified I-NC powders. Both PbS-DT and PbS-MT samples exhibited strong absorption peaks at ∼1050 cm^{-1} and ∼1190 cm^{-1} which correlated with peaks seen in spectra of the free ligands. These peaks are consistent with typical symmetric and antisymmetric S-O stretches, respectively, seen for organic sulfonic acid salts[28].

The DT ligand was observed to exchange much more readily with PbS-OLA than the MT ligand. To explore this behavior, equimolar concentrations of DT and MT solution were allowed to exchange with equal amounts of PbS-OLA NCs, in a side-by-side comparison. To minimize differences in interfacial area that might arise from

inconsistent mixing, biphasic mixtures were left undisturbed to maintain a constant interface between the aqueous and organic layers. Mixtures sat for 3 days to allow sufficient ligand exchange in the absence of continuous mixing. After 3 days, both mixtures were worked up and purified in the normal manner. Starting with the same initial mass of PbS-OLA NCs, the mass of product isolated in the DT ligand exchange reaction was ten times greater than in the MT ligand exchange. To compensate for the lower reactivity of the MT ligand relative to DT, a higher concentration of MT was used to achieve sufficient yields of PbS-MT for characterization (see Experimental for details).

To monitor any changes that may have occurred to the NC core during exchange, I-NCs were characterized by TEM and VIS-NIR absorbance spectroscopy. TEM images of the same batch of PbS-NCs before and after ligand exchange are shown in Figure 2.1 along with histograms of the particle size distribution. The average particle sizes before and after exchange were similar. Figure 2.2 shows absorbance spectra measured for the same batch of freshly exchanged PbS-MT and PbS-DT NCs as in the TEM images of Figure 2.1. The exciton peak in the VIS-NIR spectra of the I-NC spectra exhibited a red-shift of ∼40 nm relative to the parent batch of PbS-OLA. The shift is believed to be due to increased dielectric screening by water (dielectric constant ∼80) relative to toluene (dielectric constant ∼2.4), rather than a change in particle size. Examples of such solvatochromism have been reported previously in CdSe NC systems[29].

2.2.2. Stability of Ionically-Functionalized PbS Nanocrystals

The stability of I-NCs was investigated under a variety of conditions. For all studies under illumination, the samples were exposed to a tungsten-halogen light

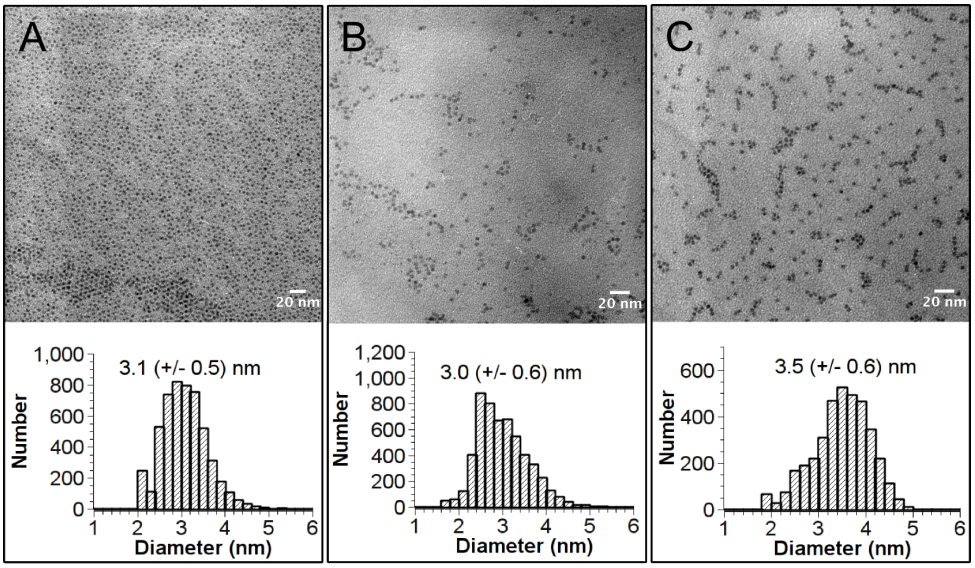

FIGURE 2.1. TEM images and size histograms of (a): PbS-OLA, (b): PbS-MT, and (c): PbS-DT nanocrystals.

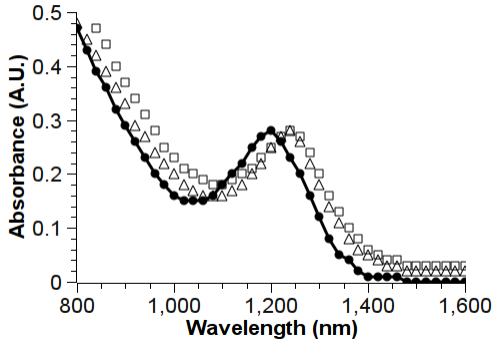

FIGURE 2.2. Absorption spectra of PbS-DT, PbS-MT, and PbS-OLA nanocrystal solutions. Spectra of freshly-exchanged PbS-DT (open squares) and PbS-MT (open triangles) NC solutions are compared to the parent PbS-OLA (solid circles) solution. I-NC spectra display a red-shift of ∼40 nm relative to the PbS-OLA spectrum.

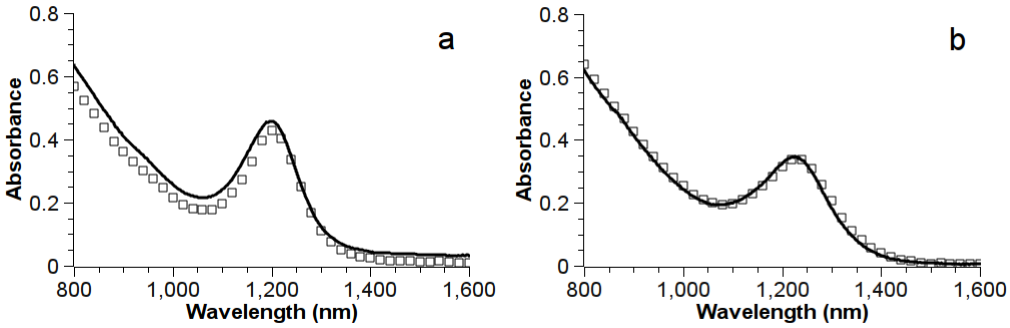

FIGURE 2.3. Comparison of the stability of PbS-MT and PbS-DT nanocrystals under air-free conditions in the light. Absorption spectra were measured fresh (solid line) and after 108 hr (squares) for (a) PbS-MT and (b) PbS-DT. Both samples were stored under 16 mW/cm^2 illumination with a tungsten-halogen lamp.

source filtered through water and with a resulting power of 16 mW/cm^2. I-NCs were stable in D_2O solution when stored under air-free conditions (see Experimental). Even when illuminated continually for greater than four days, air-free solutions showed no signs of precipitation or change in spectral features, as shown in Figure 2.3. These same samples, stored in ambient room light, have maintained stability for greater than five months.

To investigate the effects of air on the relative stabilities of PbS-MT and PbS-DT, freshly exchanged solutions were aerated for equal amounts of time. To preclude any influence of illumination, samples were kept in the dark between measurements. The resulting absorption spectra are shown in Figure 2.4. In contrast to the air-free samples, aerated I-NC solutions show complete precipitation within two days. The PbS-DT NCs did, however, prove substantially more resistant to precipitation than PbS-MT NCs. By 15 hours, the PbS-MT NCs had completely precipitated whereas there was little change in the absorption spectrum of the PbS-DT NCs. Continued monitoring of the aerated PbS-DT solution revealed a blue shift in the

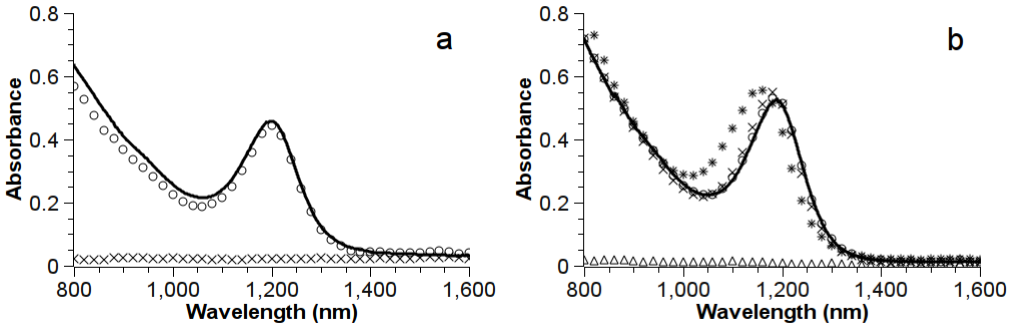

FIGURE 2.4. Comparison of the stability of PbS-MT and PbS-DT nanocrystals in aerated solution in the dark. Absorption spectra were measured fresh (solid line), after 45 min. (circles), and after 15 hr (crosses) for (a) PbS-MT and (b) PbS-DT. Additional spectra were collected for PbS-DT after 25 hr (stars) and after 42 hr (triangles).

exciton peak. This spectral shift occurred between 15 and 25 hours, but before any signs of precipitation. Complete precipitation of PbS-DT occurred by 42 hours.

The effects of illumination on aerated solutions were measured for both ligand systems. Illumination accelerated the decomposition, but again, the PbS-DT solution was observed to be more stable to precipitation than the PbS-MT solution. As shown in Figure 2.5, the PbS-MT NCs had completely precipitated from aerated solutions after 45 minutes of continuous illumination, whereas there was little spectral shift or precipitation noted over that same time period in the PbS-DT NCs. Continued illumination resulted in the complete precipitation of the PbS-DT NCs by 15 hours.

Semiconductor nanocrystals are known to catalyze the photooxidation of thiols.[23]. The photocatalytic activity of PbS-DT and PbS-MT NCs in the presence of an excess of their respective ligands was studied. The effects of extra ligand on the stability of PbS-MT and PbS-DT systems were measured by preparing solutions of each, and adding an excess of the respective free ligand. These solutions were then aerated, placed under illumination, and monitored over time via ^{1}H NMR. Aerated

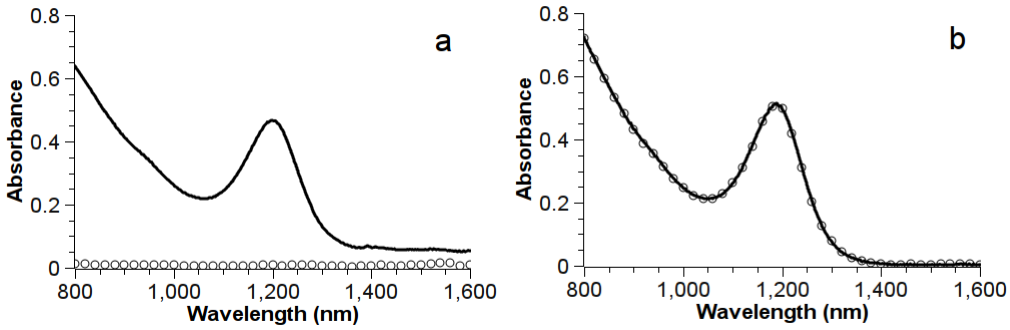

FIGURE 2.5. Comparison of the stability of PbS-MT and PbS-DT nanocrystals in aerated solution in the light. Absorption spectra were measured fresh (solid line) and after 45 min. (circles) for (a) PbS-MT and (b) PbS-DT. Both samples were stored under 16 mW/cm^2 illumination with a tungsten-halogen lamp.

and illuminated solutions of the free ligands were monitored as controls. After two days, the ^{1}H NMR spectra of the DT ligand with and without PbS-DT NCs were very similar. In both cases, the NMR resonance peaks for the initial DT (δ 3.42 (m, 2H), 3.17 (m, 1H), and 2.96 (m, 2H)) were observed to broaden substantially suggesting the formation of oligodisulfides rather than a single well-defined disulfide product. The extent of thiol oxidation in the two solutions was estimated to be within 15% of each other. In contrast, the PbS-MT NCs were observed to substantially photocatalyze the oxidation of MT ligands. The ^{1}H NMR spectra in D_2O clearly showed the conversion of the MT (δ 3.04 (m, 2H), 2.67 (t, J = 7.5Hz, 2H) and 2.03 (m, 2H)) to its disulfide product (3,3'-dithiobis-1-propanesulfonic acid, disodium salt, δ 3.04 (m, 2H), 2.87 (t, J = 7.5Hz, 2H) and 2.16 (m, 2H)) upon oxidation. After two days, 80% of the excess MT ligand had been converted to disulfide in the presence of PbS-MT NCs, whereas less than 10% of the excess MT ligand had been oxidized to disulfide in the absence of PbS-MT NCs.

Both the PbS-DT and PbS-MT solutions with excess ligand proved more stable under aerated and illuminated conditions than their respective counterparts with

no additional ligand. The PbS-DT NCs in solutions of excess ligand showed no precipitation or significant shift in their absorption spectrum for over 14 days. This compares with the complete precipitation and blue shift of the exciton peak that occurred in less than two days in the absence of excess ligand. The PbS-MT NCs in solutions of excess ligand showed only slight precipitation after one day whereas PbS-MT NC solutions with no excess ligand completely precipitated after only 45 minutes.

2.2.3. Photoconduction in PbS-DT NC films

The photoresponse of PbS-DT NC films was compared with that of PbS-OLA NC films to assess the role of chain length in the photogeneration of carriers and their subsequent transport. Films of PbS-DT and PbS-OLA NCs were prepared on interdigitated gold electrodes (IDEs) for characterization. The films were cast in air under ambient illumination. Figure 2.6 shows the ratio of the photocurrent (I_{ph}) under 100 μW illumination at 900 nm to the dark current as a function of voltage for the PbS-DT versus PbS-OLA NCs. No detectable photocurrent was measurable in the PbS-OLA NCs under these conditions or under similar illumination and with the use of lock-in amplification. To further quantify the response of PbS-DT films to light, a lock-in amplifier was used to isolate the photocurrent in the IDE devices, and a spectral response was measured at 20 Hz. Responsivities as high as $\sim$1.3 A/W were measured at the first exciton peak wavelength, as seen in Figure 2.7. An absorption spectrum of PbS-DT in solution is also shown for comparison.

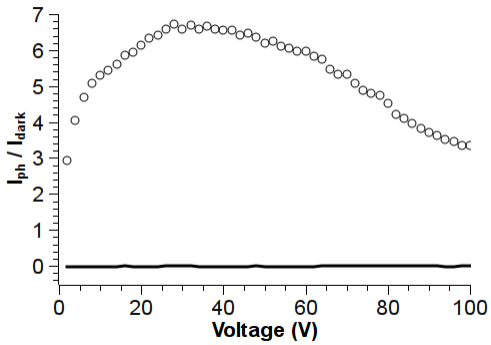

FIGURE 2.6. Ratio of photocurrent (I_{ph}) to dark current (I_{dark}) for thin-film devices of PbS-OLA and PbS-DT nanocrystals. Thin-film devices of PbS-OLA (line) and PbS-DT (open circles) were measured under 100 μW illumination at 900 nm and compared against the responses in the dark. The IDE used to measure the photoresponse of the PbS-OLA sample had half the electrode spacing of the PbS-DT sample and still no measurable photocurrent was observed.

2.3. Discussion

The key observation in this work is the enhanced stability of PbS-DT NCs relative to PbS-MT NCs (either illuminated or not). Oxygen is the primary factor affecting stability with light accelerating the oxidative precipitation. Here and throughout the discussion, the term stability generally refers to that against NC precipitation from aqueous solution. The primary observable used to ascertain stability was precipitation, rather than, for instance, direct observation of the oxidation state of the nanocrystal surface. The enhanced stability of the PbS-DT NCs relative to PbS-MT NCs can be understood by comparing and contrasting the temporal and environmental factors affecting their stability, spectral shifts observed upon aging, and their relative activity in the photocatalytic oxidation of excess ligand. Work on related thiol-stabilized PbS and CdSe NCs provides valuable guidance in understanding the stability of the PbS-DT NCs studied herein.[23,25,30,31].

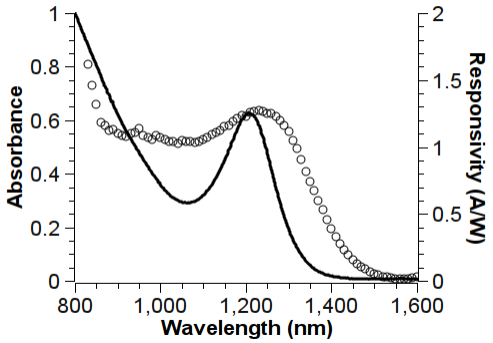

FIGURE 2.7. Spectral response of a PbS-DT thin-film device under bias. Graph shows device responsivity (circles) measured at 10 V across an 18 μm gap. For comparison, the absorption spectrum for an aqueous solution of PbS-DT is overlaid (solid line).

In their report on the photostability of hydrophilic thiols in CdSe NCs, Aldana et al.[23] developed and supported a mechanism for the photooxidation of semiconductor NCs. They showed photochemical degradation proceeds first with the oxidation of the thiol ligands to form disulfides. These disulfide species have reduced adhesion to the NC surface ultimately leading to precipitation. In the model of Aldana et al., the precise route to precipitation depends on the solubility of the disulfide formed. For soluble disulfides, precipitation occurs rapidly due to the desorption of the ligand shell. For insoluble disulfides, precipitation is slowed because the ligands form "micelle-like" structures around the bare NCs rather than redissolving in solution. These structures keep the NCs temporarily suspended, but they offer limited protection against oxidation of the NC core. Eventually, extensive oxidation of the core causes the ligand shells to collapse, and the NCs to precipitate. Dithiols were observed to be less stable than analogous monothiols in the CdSe system. This observation was logically argued to be due to the propensity of dithiols to form intramolecular

disulfides and the greater permeability to oxygen of the less densely packed ligand shell.

The model of Aldana et al. provides a good starting point to understand the results observed herein. This does raise an apparent contradiction, however, in that the dithiol DT ligand was observed to be more stable than its monothiol MT analogue in the PbS system. This contradiction is readily resolved, however, by considering the nature of the disulfides formed, as will be discussed further below. The formation of disulfides is consistent with degradation requiring the presence of oxygen; simple aging of the solutions does not lead to precipitation. Furthermore, in the photocatalytic oxidation of excess ligands, the well-defined disulfide product of MT oxidation was directly observed. Such photocatalytic oxidation of ligands has also been documented in other semiconductor NC systems[30,31].

The relative stabilities of the thiol-stabilized NCs depends on the nature of the disulfide product. The oxidation of dithiols is different from monothiols in that the former can, in principle, form either intramolecular disulfides or oligodisulfides. Aldana et al. studied 1,3 dithiols, which favor the formation of intramolecular, five-member 1,2-dithiolane rings. The DT ligand studied herein is a 1,2-dithiol that does not readily form an intramolecular disulfide because this would require the generation of a highly energetic four-member 1,2-dithietane ring[24].

The differing reactivity of 1,2- vs. 1,3-dithiols resolves the apparent contradiction in the relative stability of dithiol vs. monothiol ligands. In the case of 1,3-dithiols, intramolecular disulfide formation dominates. This facile process coupled with their comparatively lower ligand density results in the 1,3 dithiol stabilized NCs being less stable than their monothiol analogues. In the case of the 1,2-dithiols, oligodisulfide formation dominates. The resulting oligodisulfides are proposed to remain partially

bound to the NC surface thereby slowing ligand desorption and providing greater stability to precipitation.

The oligodisulfide formation mechanism is supported by a number of additional observations. As in the case of insoluble ligands studied by Aldana et al., the PbS-DT spectrum was observed to blue shift – indicating effective shrinking of the NC core – prior to precipitation. This shift suggests a period of time where the NC is encapsulated by an oligodisulfide shell that resists precipitation, but not oxidation of the core. Here, oxidation of the core refers to reaction of O_2 with the PbS-NC surface. Studies of oxidation of PbS thin films have shown formation of PbO and $PbSO_4$ upon reaction with O_2[32] and similar processes have been suggested to occur in PbE NC systems[26]. Oxidative decomposition of the PbS-NC surface, therefore, reduces the size of the NC core and results in the observed spectral blue-shift.

In contrast to PbS-DT, the PbS-MT crystals precipitate prior to any spectral shift due to rapid desorption and dissolution of the disulfide product. The low activity of the PbS-DT NCs toward the photocatalytic oxidation of excess dithiol ligands also supports the formation of oligodisulfides that do not desorb from the NC surface. In the PbS-MT case, disulfides desorbed from the surface are readily replaced by fresh monothiols when they are present in excess. This turnover of ligands on the NC surface leads to photocatalytic oxidation. The proposed absence of substantial ligand desorption from the NC surface in the PbS-DT case is consistent with the fact that it does not accelerate the photooxidation of excess ligand.

The proposed oligodisulfide shell does not apparently prevent all access to the NC surface. Indeed oxidation of the core, as evidenced by the blue shit in the NIR absorption spectrum, certainly occurs in the purified PbS-DT NCs. Furthermore, the addition of excess ligand still increases the stability of the PbS-DT NCs. Defects in the

original ligand shell or those created upon oligodisulfide formation can presumably be partially healed by the presence of excess ligand. By filling gaps in the ligand shell, surface sites that can act as nucleation sites for core oxidation are removed. Correspondingly, the absorption spectra of the PbS-DT NCs are not observed to shift prior to precipitation under oxidizing conditions in the presence of excess DT ligand.

Up to this point, oligodisulfide formation has been the focal point for rationalizing the enhanced stability of the PbS-DT NCs relative to the PbS-MT NCs. Within this model, the bidendate nature of the DT ligand is essential for oligodisulfide formation and continued binding to the NC surface. A more traditional chelate effect may also play a role. Any increased binding constant of the DT ligand relative to the monothiol due to the chelate effect could impart additional stability toward oxidation. Even in this case, oligodisulfides will be the ultimate product and remain partially bound, thereby inhibiting precipitation, until extensive oxidation occurs. Either through a traditional chelate effect, the formation of partially bound oligodisulfides, or both, the important conclusion is that DT ligands or their disulfide oxidation products remain bound to the PbS-NC surface, increasing stability to precipitation.

The enhanced stability offered by the DT ligand coupled with its short length make it an interesting candidate for the fabrication of optoelectronic devices. Photoconduction experiments are a first step in assessing the potential for the PbS-DT NCs in such applications. The responsivities of over 1 A/W in the NIR for the PbS-DT system are substantially greater than for the PbS-OLA system, where no photoresponse was measurable under similar conditions. This is as expected given how short the DT ligand is relative to OLA. The reduced interparticle spacing presumably improves charge carrier generation and transport. Despite the improvement of the PbS-DT system relative to the PbS-OLA system, other groups have achieved

responsivities as high as ∼100 A/W in the NIR with PbS-NCs[4]. Further studies are currently under way to explore the dependence of responsivity on device geometry, film deposition conditions, electric field and frequency.

2.4. Conclusions

The sodium 2,3-dimercaptopropanesulfonate (DT) ligand affords water soluble PbS-NCs that are indefinitely stable in the absence of oxygen and that exhibit greater stability than NCs based on their monothiol analogue sodium 3-mercaptopropanesulfonate (MT) in the presence of air. The 1,2 arrangement of the thiol group prevents intramolecular disulfide formation in DT, which would otherwise lead to rapid ligand desorption under oxidizing conditions, as is observed with 1,3-dithiols[23]. Instead, disulfide formation is believed to occur with the formation of oligodisulfides that inhibit precipitation by remaining partially bound to the nanocrystal surface.

The enhanced stability of the PbS-DT nanocrystals make solution processing in air and light much more feasible than with the PbS-MT NCs. Solution-cast PbS-DT films prepared in such a manner exhibit responsivities of over 1 A/W in the NIR, much greater than with PbS-OLA NCs under similar conditions. Although solutions of the PbS-DT NCs can be handled in air for hours without precipitation, the role of surface oxidation and oligodisulfide formation on the detailed optical and electrical response of thin films needs further investigation. The possibility for Na^+ transport in PbS-DT films also raises interesting questions on the influence of ion mobility on electronic behavior, as has been investigated in ionically functionalized organic semiconductors.[33,34].

2.5. Experimental

2.5.1. Chemicals

Lead (II) oxide (PbO), oleic acid (OLA, 90 % technical grade), 1-octadecene (ODE, 90 % technical grade), *bis*(trimethylsilyl)sulfide, 3-mercapto-propanesulfonic acid, sodium salt (MT, 90 %), and 2,3-dimercaptopropanesulfonic acid, sodium salt, monohydrate (DT, 95 %) were all purchased from Aldrich.

2.5.2. Nanocrystal Synthesis

This procedure closely follows the one reported by Hines and Scholes[27]. A typical procedure follows: First, 0.36 g (1.6 mmol) PbO was dissolved in 8.0 mL (7.1 g, 25 mmol) OLA and heated under vacuum at ∼100°C to drive off water and form lead oleate. Once the water was removed, the flask was back-filled with nitrogen, and the temperature was raised to 130°C. At this stage, 8 mL of a 0.1 M solution of *bis*(trimethylsilyl)sulfide in ODE was quickly injected into the stirring mixture of Pb-oleate, initiating nucleation of PbS nanocrystal growth. Immediately after injection, the heat was removed, and the flask was left stirring as it slowly cooled to room temperature. The crude nanocrystal solution was purified by a series of precipitation-centrifugation-resuspension steps. Nanocrystals were precipitated with methanol, centrifuged to remove supernatant, and then redissolved in toluene. This procedure was performed twice to remove unreacted lead oleate and freely dissolved oleic acid. Unless otherwise specified, nanocrystal solutions were transferred via gas-tight syringe to sealed vessels under an inert N_2 atmosphere. Methanol and toluene used in the work-up were distilled under nitrogen prior to use.

2.5.3. Nanocrystal Ligand Exchange

Natively functionalized oleic-acid capped PbS nanocrystals were exchanged with 3-mercaptopropanesulfonic acid, sodium salt (MT) or 2,3-dimercaptopropanesulfonic acid, sodium salt (DT) in a biphasic solution of toluene and water. In NMR experiments, benzene-d6 or toluene-d8 and D_2O were used instead to minimize solvent proton signals. Biphasic mixtures were manually shaken for ∼1 h and then centrifuged for 5 min. at 4000 RPM to break any formed emulsions. The organic layer, along with any remaining organic-soluble NCs, were removed from the aqueous layer and discarded. Ionically-functionalized NCs (I-NCs) in the aqueous layer were washed 3x with toluene to remove any remaining free oleic acid. I-NCs were then precipitated with acetonitrile, centrifuged to remove supernatant, and then redissolved in H_2O. This procedure was performed twice to remove any freely dissolved ligand from the NC solution.

A typical exchange procedure used equal volumes of a 25 mg/mL solution of PbS-OLA in toluene and either a 180 mM solution of MT or 78 mM solution of DT in water. Ligand concentrations correspond to ∼10:1 molar ratio of MT/OLA and ∼5:1 molar ratio of DT/OLA. Under these conditions, 78 % of the original mass of PbS-OLA nanocrystals was recovered in the MT/OLA exchange, compared to 87 % in the DT/OLA exchange.

All non-deuterated solvents used in the exchange reactions were distilled under nitrogen prior to use. Deuterated solvents were degassed using the freeze-pump-thaw technique repeated 3x, prior to use. Deuterated solvents were obtained from Cambridge Isotope Laboratories, Inc. All other reagents and starting materials used here were obtained from Sigma-Aldrich.

2.5.4. Spectroscopy

Near-infrared (NIR) absorption spectra were measured on a Perkin-Elmer Lambda 19 UV/VIS/NIR Spectrophotometer. If not already sufficiently dilute, all NC solutions were diluted to a concentration region (∼1 mg/mL) that gave a linear response with absorbance. Fourier Transform Infrared Spectra (FTIR) were measured using a Nicolet Magna-550 Fourier Transform Infrared Spectrophotometer. Solution ^{1}H NMR spectra were obtained from a Varian INOVA 300MHz spectrometer. Chemical shifts reported for oleic acid are relative to tetramethylsilane (TMS). All other chemical shifts are relative to trimethylsilyl tetradeuteriopropionic acid, sodium salt (DSS).

2.5.5. Transmission Electron Microscopy (TEM)

Samples of PbS-OLA were prepared by adding a drop of dilute NC solution in chloroform atop a SiO-coated, Formvar-supported, 200 mesh copper grid and blotting with filter paper from below to wick away excess solvent. Samples of PbS-MT and PbS-DT were prepared using surface-functionalized "Smart Grids" obtained from Dune Technologies, Inc. A drop of dilute I-NC solution in deionized water was added atop a"Smart-Grid". After ∼10 s, the grid was dipped in deionized water to remove excess sample, then blotted dry from beneath using filter paper. Images were taken using a Philips CM12 Transmission Electron Microscope operating at 100 keV.

2.5.6. Stability Studies of MT- and DT- PbS-NCs

Freshly exchanged I-NC solutions were diluted to a concentration region (∼1 mg/mL) that gave a linear response with absorbance. Air-free samples were prepared by transferring solution to glass cuvettes, freezing in liquid N_2, and flame-sealing

while under active vacuum. Aerated samples were prepared by transferring solution to glass cuvettes, bubbling with air for 1 min., and loosely capping to prevent solvent evaporation. "Dark" samples were wrapped in foil, stored in a dark cabinet, and only exposed to light for brief periods during absorption measurements. "Light" samples were placed under continuous illumination in front of an EHJ tungsten-halogen light source. The light was filtered through a water filter with a resultant intensity of 16 mW/cm^2. To reduce scattering effects due to flocculation, prior to an absorption measurement, aerated solutions were transferred to centrifuge tubes, centrifuged, and then returned to the cuvettes leaving behind any insoluble solids. The pH of both PbS-MT and PbS-DT solutions used in the stability studies was measured to be ∼9.3.

2.5.7. Stability of I-NCs with Extra Ligand

Freshly exchanged I-NC solutions were diluted to a concentration of ∼1 mg/mL with an aerated solution (∼7 mM) of the respective thiol ligand and placed in an NMR tube. An equal volume of the same thiol-only solution was also placed in an NMR tube, and both tubes were set under ∼16 mW/cm^2 illumination from a tungsten-halogen lamp. Samples were monitored over time via ^1H NMR.

2.5.8. Electrode Fabrication

The active area of the interdigitated gold electrodes (IDE) used in this study consisted of a set of twenty interlocking gold fingers separated by 10-20 μm gaps and running a length of 3 mm. Gold fingers on the IDE were formed using a lift-off procedure. Gold films were deposited by thermal evaporation onto a glass substrate using a chromium adhesion layer, onto a glass substrate patterned with Shipley S1818

photoresist. Gold-coated slides were then soaked in acetone overnight and rinsed with fresh acetone to remove metal not adhered directly to the glass.

2.5.9. Film Casting

Devices were fabricated by drop-casting a PbS-NC film from a concentrated solution (50-80 mg/mL) in appropriate solvent onto a clean gold IDE. PbS-OLA NCs were cast from toluene solution, while PbS-MT and PbS-DT NCs were both cast from aqueous solution. To improve coating between the gold fingers, the IDE was pretreated with oxygen plasma for 5 min. to remove remnant organic molecules from the gold surface and to create a more hydrophillic surface. Deposition was performed in air, and films allowed to dry by evaporation in a fume hood. Nanocrystal films were dried further by placing them under vacuum for 6-12 hours.

2.5.10. Device Characterization

Current-voltage measurements were performed using an Agilent 4156C semiconductor parameter analyzer. Illumination was achieved by focusing light from a EHJ tungsten-halogen lamp through a monochromator and onto the device area. For responsivity measurements, monochromated light was mechanically chopped at a frequency of 20 Hz before being focused onto the device area, and the current was measured using a Stanford Research Systems SR530 lock-in amplifier. For the 800-1600 nm spectral range measured here, a long pass filter (800 nm) was used to remove higher order diffraction lines. Light intensity was controlled through use of neutral density filters, and was measured separately at each wavelength using a calibrated InGaAs (Newport) detector placed at the device position. The intensity reported and used for responsivity calculations is that incident on the portion of the film between

the gold fingers of the interdigitated electrode. To reduce noise associated with the source-measure unit of the parameter analyzer, a separate DC power supply was used to provide bias during the responsivity measurements.

2.6. Bridge to Chapters III and IV

In Chapter II, the method of preparation of two, novel PbS nanocrystal-ligand assemblies was presented. PbS nanocrystals (PbS-NCs) were functionalized with either sodium 3-mercaptopropanesulfonate (MT) or sodium 2,3-dimercaptopropane-sulfonate (DT) via a facile, biphasic ion exchange procedure. Physical characterization of the two new materials proved that exchange from an oleic acid (OLA) ligand to either an MT or DT ligand was successful and complete. This exchange procedure represents one of the few solution-phase examples that exist for functionalization of PbS-NCs with short-chain alkyl ligands.

The reduced steric bulk of short-chain ligand shells relative to ones composed of long-chain fatty acids or phosphines allows for increased packing density and increased charge transport in PbS-NC thin films. The comparison of thin films of DT-functionalized PbS-NCs (PbS-DT) with OLA-functionalized PbS-NCs (PbS-OLA) showed that PbS-DT offers orders of magnitude improvements in both conductivity and photoconductivity relative to PbS-OLA. The promising preliminary device data from thin films of PbS-DT nanocrystals suggested that these materials warranted more study as the active material in photonic devices. This subject is explored in greater detail in Chapter IV.

Also in this chapter, the similarity in the chemical structures between the MT and DT ligands suggested an opportunity to investigate the relative stabilities of PbS-MT and PbS-DT nanocrystal solutions. MT and DT differ only in their head

group, with DT ligands containing an additional thiol group at the C2 position. This difference in head group was found to have a profound effect on the stability of the resulting PbS-MT and PbS-DT nanocrystal solutions, with PbS-DT solutions more stable to precipitation than PbS-MT solutions. The increased stability of PbS-DT solutions relative to PbS-MT solutions was attributed to the chelating effect of the dithiol head group of DT, which was found to be more robust to oxidation than the monothiol head group of MT ligands.

The differential stability of PbS-MT and PbS-DT nanocrystals, with a concomitant similarity in structure, made these materials a compelling system with which to study the biological effects of PbS nanocrystal exposure. The field of nanotoxicology is still young, and many of the interactions of novel nanomaterials with biological systems are not well understood. Complicating the existing studies is the fact that many of the material systems themselves are not well-characterized. Here, we had the opportunity to explore the toxicology of a relatively well-characterized set of materials that differed only in a single aspect of their physical properties – that of head group structure and the resulting difference in relative oxidative stability. Chapter III examines the effect of the differential stability of PbS-MT and PbS-DT nanocrystals (explored in this chapter) on the biological effects in embryonic zebrafish subjected to waterborne exposure of these nanocrystal solutions.

A special note on terminology – throughout Chapter III, the term "nanoparticle" replaces "nanocrystal," which is used everywhere else in this document. This change in wording is purely one of convention. In other words, a "PbS nanoparticle" in Chapter III is equivalent to a "PbS nanocrystal" elsewhere in this document.

CHAPTER III

DIFFERENTIAL STABILITY OF LEAD SULFIDE NANOPARTICLES INFLUENCES BIOLOGICAL RESPONSES IN EMBRYONIC ZEBRAFISH

3.1. Introduction

Nanoparticles (NPs) are becoming ubiquitous as they are incorporated into an increasing number of commercial products. Exploiting their unique material properties, nanoparticle-based applications will undoubtedly revolutionize many features of our lives. Nanotechnology is used in a broad spectrum of applications, encompassing cosmetics, biomedical supplies, fluorescent bioimaging, and electronics (Minchin and Martin 2010, Usenko et al. 2007, Bharali et al. 2009, Newman et al. 2009).

Despite the rapid growth of the nanotechnology industry, research into interactions of nanoparticles with environmental and biological systems has not kept pace with material development. Currently, the interplay between nanoscale materials and biological systems is poorly understood, and hazards have not been fully evaluated. Without toxicological data regarding the biocompatibility of nanoparticles, it is impossible to identify risk associated with nanoparticle exposure.

An efficient testing method, if proven predictive, would help with these critical data gaps.

Various biological models have been proposed for toxicological assessments including *in vitro* and *in vivo* methodologies. *In vitro* studies, such as cell culture, are rapid, efficient, and low cost. However, results from these studies are often difficult to translate to the whole organism. Utilizing *in vivo* models may offer a more immediately relevant platform for translational studies (Teraoka et al. 1993, den Hertog 2005, Hall et al. 2007). The widely accepted rodent model is both cost and labor intensive; it requires extensive animal care facilities and significant quantities of test materials for the toxicity assessments. A powerful alternative is the zebrafish model (Parng 2005), which is now widely accepted for mechanistic-based toxicological studies (Haendel et al. 2004, Hill et al. 2005, Ton et al. 2006, Usenko et al. 2007, Bar-Ilan et al. 2009).

Zebrafish have a high degree of homology to the human genome and share many cellular, anatomical, and physiological characteristics with other vertebrates (Barbazuk et al. 2000). Their small size, rapid development, and short life cycle make zebrafish an ideal rapid assessment model, which is needed to provide solid and crucial toxicological data (Dodd et al. 2000, Rubinstein 2003, Yang et al. 2009). Female zebrafish are capable of producing hundreds of embryos a day, thereby providing statistical power to the analysis. Embryos develop externally and are transparent for the first few days of their development, allowing for non-invasive assessments (Kimmel and Ballard 1995). The small quantity needed to fully evaluate biological responses to a novel engineered nanoparticle (typically, less than 1 mg) is also a major advantage for green by design synthesis strategies. With other models, material requirements are orders of magnitude greater. This combination of rapid assessments, unlimited

embryos, and minimal material needs makes the zebrafish model ideal for investigation of nanomaterial-biological interactions.

Lead sulfide nanoparticles (PbS-NPs) have been increasingly developed and studied due to their unique electrical and optical properties. Like other semiconductor nanoparticles, they exhibit quantum confinement below a certain size threshold – the so-called, *quantum size effect* – that allows their optical and electrical properties to be precisely tuned with size. Lead sulfide, in particular, has shown promise as a material that is optically active in the near-infrared (NIR) region of the electromagnetic spectrum. Sensitivity to this spectral window is critical for a variety of photonic applications, including single- and multi-junction solar cells (Koleilat et al. 2008, McDonald et al. 2005), NIR photodetectors for telecommunications (Konstantatos et al. 2006), and NIR light-emitting diodes (LEDs) (Konstantatos et al. 2005). Additionally, solubilized PbS-NPs have been studied as fluorescent biomarkers that can take advantage of the transparent tissue window at 700 - 1,000 nm for *in vivo* cellular imaging (Hyun et al. 2007, Hinds et al. 2007, Lim et al. 2003).

Despite increased interest in PbS-NPs as industrial materials, very little is known about their biological or environmental interactions. Compounds containing lead can induce a wide variety of adverse human effects (Agency for Toxic Substances and Disease Registry (ATSDR) 2007), such as genotoxicity (Zelikoff et al. 1988), oxidative stress (Sharma et al. 2010), and neurological effects (De Gennaro 1978). It is known that lead can affect multiple systems in the body, most notably the nervous system. Cardiovascular, immune, and reproductive systems as well as bones, teeth, and kidneys are also sensitive targets (White et al. 2007). Lead sulfide (PbS) – *galena* – is an extensively mined ore, which is negligibly soluble in aqueous systems, making bioavailability in solutions limited. PbS can undergo decomposition processes,

and reduced particle size is known to increase decomposition rates (Liu et al. 2009), which influences the amount of ionic lead available. To complicate the understanding of nanoparticle–biological interactions, nearly all colloidal nanoparticle preparations have organic stabilizing molecules, ligands, that bind to the surface of the core, passivate surface states, retard particle growth and agglomeration, and imbue the nanoparticles with solubility.

Toxicological studies on other nanoparticle systems have identified key structural features important to understanding of nanomaterial–biological interactions (Kirchner et al. 2005, Kotov et al. 2009). One such feature, chemical composition of the nanoparticle core, has been identified as a good predictor of toxicity. Nanoparticles composed of known toxic metals – for example cadmium (Samia et al. 2003, Kirchner et al. 2005) and silver (Wise et al. 2010) – are generally more toxic than those composed of inert materials such as gold (Bar-Ilan et al. 2009). Core size is also an important feature, with smaller particles of the same core material, generally more toxic than larger ones (Meng et al. 2007, Guo et al. 2008). Smaller particles are thought to interact more strongly with biological systems, either through enhanced cellular uptake or through faster decomposition due to greater surface area-to-volume ratios compared to larger particles. In addition to the composition of the nanoparticle core, ligand shells can affect nanoparticle toxicity (Hoshino et al. 2004).

This wide array of variables can make correlation of structure-activity relationships difficult. The aim of this study was to isolate one of these variables – ligand head group – as a key factor in nanoparticle stability, while keeping all other factors (core material, core size, and ligand tail group) constant. At the same time, we hoped to open investigation into the little understood toxicity of the technologically relevant nanomaterial – PbS. Specifically, in this study, two

types of water-soluble PbS-NPs were tested in the embryonic zebrafish system. Both PbS-NPs had similar core size (∼3 nm) and were functionalized with either a sodium 3-mercaptopropanesulfonate (MT) ligand or its bidentate analog – sodium 2,3-dimercaptopropanesulfonate (DT). These two ligands are structurally analogous; both ligands have the same carbon backbone and sulfonate tail group and differ only in the head group – mono- vs. dithiol, respectively. Prior studies on these nanoparticles revealed that the two ligands offered differential protection against oxidative decomposition, with MT-functionalized particles being less stable to precipitation (Moody et al. 2008). This feature made MT- and DT-capped nanoparticles a compelling set in which to study the effects of particle stability on nanoparticle toxicity, while keeping other structural features unchanged. Utilizing the zebrafish model to screen for developmental toxicity revealed that the different surface functionalizations of the nanoparticles produced different biological responses.

3.2. Materials and Methods

3.2.1. Nanoparticles

Materials Lead (II) oxide (PbO); oleic acid (OLA, 90% tech. grade); 1-octadecene (ODE, 90% tech. grade); bis-(trimethylsilyl) sulfide; 3-mercaptopropanesulfonic acid, sodium salt (MT, 90%); and, 2,3-dimercaptopropanesulfonic acid, sodium salt, monohydrate (DT, 95%) were all purchased from Aldrich. Deuterium oxide was obtained from Cambridge Isotope Laboratories, Inc. Acetonitrile and toluene were distilled under nitrogen from P_2O_5 and Na/benzophenone, respectively, before use. Nanopure water and other solvents were deoxygenated either by sparging with nitrogen or freeze-pump-thaw degassing.

Synthesis of Lead Sulfide Nanoparticles (PbS-NPs) Moody et al. (Moody et al. 2008) have previously reported this procedure. Briefly, PbO was dissolved in OLA and heated under vacuum to remove water and form lead oleate. To form PbS-NPs, a solution of bis-(trimethylsilyl) sulfide in ODE was quickly injected into the stirring mixture of lead oleate at 130°C under nitrogen. After cooling, the crude nanoparticle solution was purified by a series of precipitation-centrifugation-resuspension steps, using distilled toluene and methanol as the solvent and non-solvent, respectively. Oleic acid-capped PbS-NPs were then exchanged with either MT or DT ligands in a biphasic solution of toluene and water. Biphasic mixtures were manually shaken for 1 h and then centrifuged. The organic layer, along with any remaining organic-soluble NPs, was removed from the aqueous layer and discarded. Thiol-functionalized NPs in the aqueous layer were washed with toluene to remove any remaining free OLA. To purify the nanoparticles, another series of precipitation-centrifugation-resuspension steps was performed using nanopure water and acetonitrile, as the solvent and non-solvent, respectively. A typical exchange procedure used equal volumes of a 25 mg/mL solution of PbS-OLA in toluene and either a 180 mM solution of MT or 78 mM solution of DT in water.

At all steps in the synthesis and exchange, standard airfree techniques were employed. Samples and reagents were stored under nitrogen in Schlenk flasks or centrifuge tubes with septa caps and transferred via gas-tight syringes.

3.2.2. Physical Characterization of Nanoparticles

Near-Infrared (NIR) Absorption Spectroscopy Absorption spectra were measured on a Perkin-Elmer Lambda 19 UV/VIS/NIR Spectrometer. To reduce solvent absorption in the spectral window of interest, deuterium oxide was used

in place of water for this measurement. Nanoparticle solutions were diluted to a concentration regime (∼1 mg/mL) where a linear dependence of absorbance on concentration was observed.

Transmission Electron Microscopy (TEM) Samples of PbS-MT and PbS-DT were prepared using amine-functionalized "Smart Grids" obtained from Dune Sciences, Inc. To prepare, a "Smart-Grid" was floated atop a drop of dilute nanoparticle solution. After 10 s, the grid was dipped in deionized water to remove excess sample and then blotted dry from beneath with a Kimwipe. Images were taken using an FEI Titan 80-300 S/TEM microscope operating at 300 keV at 56 k magnification and a pixel resolution of 2.58 pixels/nm.

Size analysis was performed using ImageJ software. Image contrast was enhanced to the minimum level necessary for automated particle counting, and all images were processed identically. To improve contrast, a Gaussian blur function and bandpass filter were applied. Segmenting was achieved using the "MultiThresholder" plug-in, utilizing the "Intermodes" method. Prior to automated counting, size and circularity constraints were used to remove large agglomerates from the count. The results of the automated particle analysis were checked against the original image. Particle diameter was taken to be the average of the major and minor axes of the ellipse fit.

Lead Analysis by Inductively Coupled Plasma-Optical Emission Spectrometry (ICP-OES) Three aliquots (50 μL each) for both fresh PbS-MT and PbS-DT (nominally, 3 mg/mL) were analyzed. Aliquots were digested with 196 μL of ultra pure nitric acid (HNO_3) (VWR: 87003-226) for 12 h prior to analysis. The remaining nanoparticle solutions were then left to precipitate (age) under ambient conditions for 5 days. When precipitated, the nanoparticles from both

solutions collected as insoluble agglomerates, leaving fractions of solubilized lead in the clear supernatant. For each aged sample, the supernatant was drawn off and centrifuged at 13,000 rpm for 10 min to remove any remaining nanoparticles. The centrifuged supernatant (50 μL) was then digested in the same manner as for the fresh nanoparticle solution aliquots (three replicates). Prior to sampling, each sample was diluted to 10 mL with Milli-Q water. Samples were vortexed and placed into autosampler racks prior to being analyzed. The ICP-OES was calibrated using a lead standard in 0.5% HNO_3 at seven concentrations (0.25, 0.5, 5, 10, 20, 35, and 50 ppm). The calibration curve created by the standard solutions had an R^2 value of 0.996. Measured concentrations of lead in the undiluted nanoparticle solutions were back-calculated from the lead content determined by ICP-OES in the aliquots and the dilution factor. The percentage of recovered lead was calculated from the ratio of the measured concentration to the theoretical concentration. The theoretical concentration is based on several assumptions: the nanoparticles are spherical, the Pb to S ratio in the core is 1:1, and the surface Pb atom to ligand ratio is 1:1. Given these assumptions, the calculated theoretical concentrations of lead in the fresh solutions were 2,189 ppm for PbS-MT and 2,129 ppm for PbS-DT.

Dynamic Light Scattering (DLS) Equal concentrations (40 ppm) of PbS-MT and PbS-DT were prepared by diluting aqueous nanoparticle stock solutions (20 mg/mL in deionized water) with fish water (FW). Immediately after dilution, solutions underwent a single pass through a 0.2-μm filter to remove dust that could influence the scattering experiments. Hydrodynamic radii were taken as the average of three samples and measured using a Brookhaven 90 Plus Particle Size Analyzer.

3.2.3. Zebrafish

Exposure Protocol Embryonic zebrafish were obtained from a Tropical 5D strain of zebrafish (*Danio rerio*) reared in the Sinnhuber Aquatic Research Laboratory (SARL) at Oregon State University. Adults were kept at standard laboratory conditions of 28°C on a 14-h light/10-h dark photoperiod in FW consisting of reverse osmosis water supplemented with a commercially available salt (Instant Ocean®) to create a salinity of 600 microsiemen. Sodium bicarbonate was then added as needed to adjust the pH to 7.4. Zebrafish were group-spawned, and embryos were collected and staged as described by (Kimmel and Ballard 1995). To increase bioavailability, the chorion, an acellular envelope surrounding the embryo, was removed enzymatically with pronase at 4 h post fertilization (hpf). Briefly, embryos were placed in 25 mL of FW with 50 μL of 50 mg/mL pronase (Fluka #81748) for 45 min; the water was decanted and replenished with fresh FW for a total of 10 min. Embryos were allowed to rest for at least 30 min prior to the initiation of nanoparticle exposure. After the rest period, dechorionated embryos were transferred to individual wells of a 96-well plate with 100 μL of prepared nanoparticle solution. Control animals were exposed to FW only. Non-exposed animals (embryos raised in FW with the chorion intact) were also retained to monitor inherent embryo quality. Embryos were exposed to a FW control and six concentrations of nanoparticles (n = 24, three replicates), with the highest concentration being 320 μg/mL (ppm) and the remainder from sequential two-fold dilutions down to 10 ppm. The static nanoparticle exposure continued under standard laboratory conditions in sealed plates until 120 hpf. Each individual embryo was scored for mortality and morphological malformations at 120 hpf. Only surviving embryos were accounted for when assessing for malformation. Fifteen morphological malformations were evaluated: yolk sac edema, bent body

axis, eye, snout, jaw, otolith pericardial edema, brain, somite, caudal fin, pectoral fin, circulation, pigmentation, trunk length, and swim bladder. Representative images were captured of malformed embryos using an Infinity 3 CCD camera. The percent mortality and total malformations were calculated and graphed as a mean of three replicates with standard error bars.

Determination of Nanoparticle Uptake by ICP-MS Embryos were exposed beginning at six hpf to PbS nanoparticle solutions of 10, 20, 40, 80, 160, and 320 μg/mL, and the embryos were sampled at 12 hpf to quantify their overall lead tissue concentrations. For each exposure group, three embryos were removed with plastic pipette tips and washed with 40 μL of Milli-Q water three times in a 35-mm plastic petri dish. The pooled embryos were placed into individual 14-mL round bottom plastic tubes and stored at –20°C until time to sample. Twelve hours prior to sampling, the embryos were digested using 98 μL nitric acid; 1 ppb of internal standard (Indium, Rhenium and Bismuth) was added, and the samples were brought to a total volume of 5 mL with Milli-Q water. Samples were vortexed for 10 s prior to being placed into the autosampler racks. The ICP-MS was calibrated using a lead standard in 0.5% HNO_3 at five concentrations (0.01, 0.1, 1, 5, 10 ppb) with 1 ppb internal standards. The calibration curve created by the standard solutions had an R^2 value of 0.992. The mass of lead contained in each embryo was calculated from the measured lead concentration of the aliquots and the dilution factor.

Statistics All analyses were compiled using SigmaStat/Plot 11 (SPSS Inc, Chicago, IL). Dose response significance was determined using one-way ANOVA ($P < 0.05$) and Dunnetts post hoc tests. All exposure groups consisted of 24 individually exposed

embryos (N = 24), three replicates unless otherwise noted with 80% confidence of significant difference.

3.3. Results

3.3.1. PbS Nanoparticles Synthesized Through Ligand Exchange From A Common Core

Sodium 3-mercaptopropanesulfonate (MT)- and sodium 2,3-dimercaptopropanesulfonate (DT)-capped lead sulfide nanoparticles were synthesized (Fig. 3.1a) and purified in an identical manner, using a biphasic exchange from oleic acid-capped lead sulfide nanoparticles (see Materials and Methods). Furthermore, each toxicological trial was performed using PbS-MT and PbS-DT nanoparticles prepared from the same parent batch of oleic acid-capped nanoparticles. This was done to minimize the possibility that differences in biological response arose from different synthetic preparations. In addition, post-synthesis characterization of the nanoparticle cores was also conducted. Transmission electron microscopy (TEM) was used to image and calculate average nanoparticle sizes. Size analysis performed on TEM micrographs of representative samples of PbS-MT (Fig. 3.1c) and PbS-DT (Fig. 3.1d) revealed similar average particle diameters (3.0 and 3.5 nm, respectively). Corresponding near-infrared (NIR) absorption spectroscopy experiments (Fig. 3.1b) showed close spectral overlap between the two materials, with exciton peaks observed at 1,188 (PbS-MT) and 1,202 nm (PbS-DT). Both TEM and NIR absorption measurements were taken on freshly made particles and indicate initial properties. Precipitation of the nanoparticles over the course of the zebrafish exposures made post-exposure characterization infeasible.

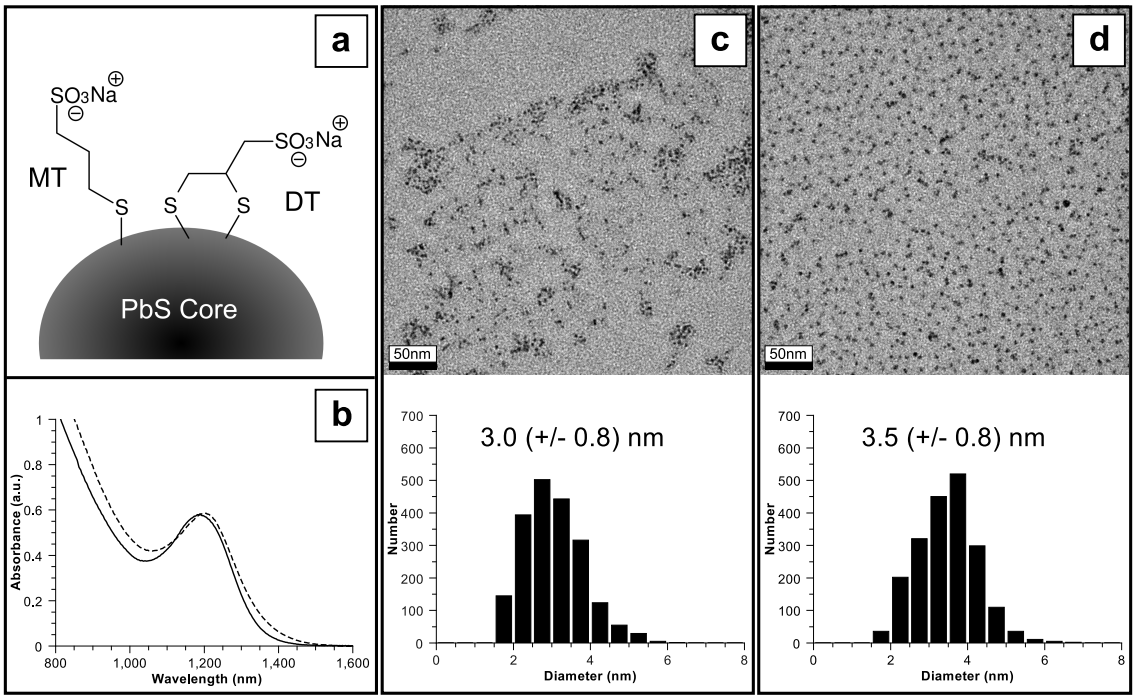

FIGURE 3.1. Physical properties of PbS-MT and PbS-DT nanoparticles. **a** Schematic of two ligands used in the study – sodium 3-mercaptopropane sulfonate (MT) and sodium 2,3-dimercaptopropane sulfonate (DT). **b** Near-infrared absorption spectra of solutions of PbS-MT (*solid*) and PbS-DT (*dashed*) nanoparticles. Peak position is indicative of average particle size. Plots were scaled to better illustrate spectral overlap. **c** and **d** TEM images of PbS-MT and PbS-DT, respectively, with corresponding particle size histograms. *Scale bars* represent 50 nm. Values in histograms show average nanoparticle diameter, with standard deviation in *parentheses*.

3.3.2. PbS-MT, PbS-DT, and Lead Nitrate Elicit Differential Biological Responses

Embryos were exposed to suspensions of lead sulfide nanoparticles capped with either the monothiol sodium 3-mercaptopropanesulfonate (PbS-MT) or the dithiol sodium 2,3-dimercaptopropanesulfonate (PbS-DT) over a twofold concentration (10-320 μg/mL) range to determine whether the nanoparticles elicited embryo mortality or induced developmental malformations. Exposure to PbS-MT induced mortality in 100% of the animals at 160 μg/mL (Fig. 3.2a). At concentrations as low as 20 μg/ml, PbS-MT induced 20% mortality in the embryos and the remaining 80% survivors had an average of five malformations (Fig. 3.2b). The multiple malformations observed upon PbS-MT exposure are visually represented in Fig. 3.3b and include bent body axis, jaw, brain, and snout. At 40 and 80 μg/mL, the incidence of mortality was statistically significant ($P < 0.001$) and increased to 75 and 92%, respectively. All surviving embryos exposed to PbS-MT displayed multiple malformations, with an average of 4.5 at 40 μg/mL (Figs. 3.2b, 3.3b). Embryos exposed to PbS-DT nanoparticles, however, did not display statistically significant mortality at the same concentrations tested for PbS-MT (Figs. 3.2a, 3.2b, 3.3c). PbS-DT-exposed embryos had a consistent number of malformations (between 1.5 and 2.3) at concentrations between 10 and 320 μg/mL, which is similar to that observed at higher concentrations (>80 μg/mL) for the ionic lead control sample, lead nitrate ($Pb(NO_3)_2$). The lead nitrate control was intended to model the extreme situation where the NPs entirely decomposed into water-soluble lead salts, which is admittedly unlikely given the insolubility of PbS (Ksp of 2.5 x 10^{-27}). Lead nitrate is soluble in pure water, but the presence of carbonate and other anions in the FW used for the experiments leads to some precipitation. Further, the addition of $Pb(NO_3)_2$ also results in the

acidification of the FW to as low as pH = 5.2 at the highest concentrations. It is noted that PbS-MT and PbS-DT are soluble in FW at the concentrations used in this study, and their addition does not affect the pH. The various equilibria involving lead ion in FW mean that the listed concentrations for $Pb(NO_3)_2$ do not necessarily represent the concentration of freely soluble lead. Nevertheless, $Pb(NO_3)_2$ remains a good control because the same equilibria affecting its bioavailability also operate on any ionic lead leached from the nanoparticles. The onset of mortality in $Pb(NO_3)_2$ exposures occurred at a greater concentration than that observed for PbS-MT exposures. Embryos exposed to 1040 μg/mL of lead nitrate had 0.25 or fewer malformations, but the average number of malformations rose to 2.3 at 160 μg/mL. Lead nitrate induced a statistically significant increase in bent body axis in the embryo (Fig. 3.3d) at 160 μg/mL. Near 320 μg/mL, 100% mortality was observed for both $Pb(NO_3)_2$ and PbS-MT. At this concentration, no significant mortality was observed for PbS-DT exposures.

3.3.3. Monothiol And Dithiol Ligands Did Not Induce Biological Responses

To determine whether the ligands themselves were responsible for the adverse biological response, embryonic zebrafish were exposed to MT and DT ligands independent of the nanoparticles. Both ligands were tested at the same concentrations used for the nanoparticle exposures. These concentrations were greater than the ligand concentrations in the corresponding nanoparticle solutions, since the ligands make up only a fraction of the nanoparticle-ligand complex. As seen in Fig. 3.2c and d, there was no statistically significant increase in malformation or mortality observed in embryos exposed to the ligands.

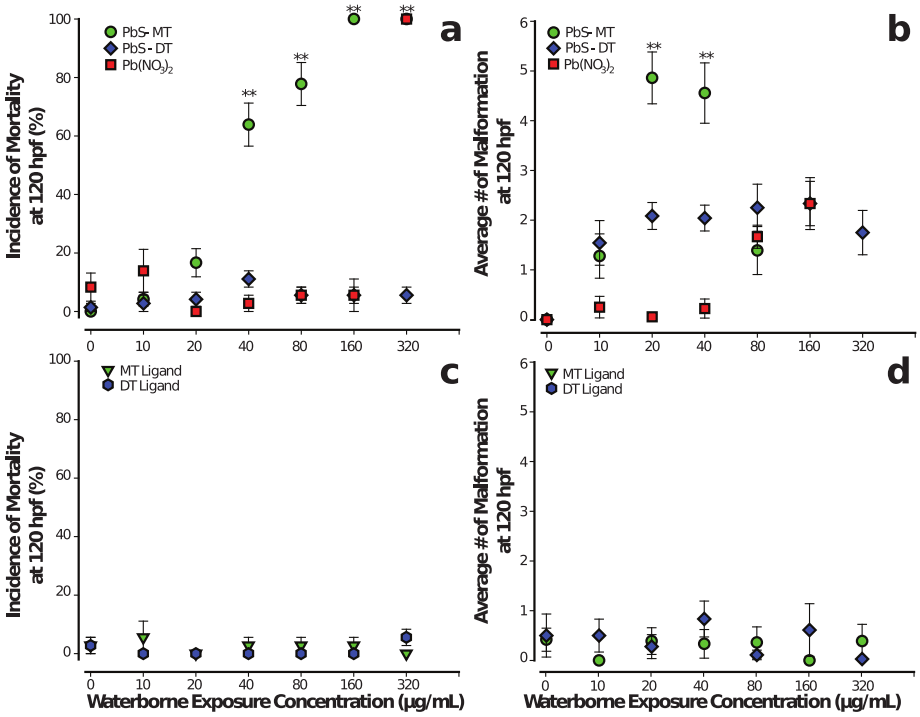

e

Waterborne Exposure Concentration (µg/mL)	Bent Body Axis (%)			Eye Malformation (%)			Snout Malformation (%)			Jaw Malformation (%)		
	PbS-MT	PbS-DT	$Pb(NO_3)_2$	PbS-MT	PbS-DT	$Pb(NO_3)_2$	PbS-MT	PbS-DT	$Pb(NO_3)_2$	PbS-MT	PbS-DT	$Pb(NO_3)_2$
0	0 ± 0	0 ± 0	0 ± 0	0 ± 0	0 ± 0	0 ± 0	0 ± 0	0 ± 0	0 ± 0	0 ± 0	0 ± 0	0 ± 0
10	11.6 ± 3.3	72.2 ± 5.5	2.8 ± 2.8	0 ± 0	5.6 ± 2.8	2.8 ± 2.8	8.6 ± 0.3	5.6 ± 2.8	2.8 ± 2.8	8.6 ± 0.3	5.6 ± 2.8	2.8 ± 2.8
20	93.3 ± 6.6	59.8 ± 7.7	2.8 ± 2.8	20 ± 6.9	23.2 ± 8.1	0 ± 0	66.7 ± 0	5.8 ± 2.9	0 ± 0	61.1 ± 2.8	5.8 ± 2.9	0 ± 0
40	88.9 ± 5.6	77.8 ± 4.0	2.8 ± 2.8	88.9 ± 5.6	2.8 ± 2.8	0 ± 0	94.4 ± 5.6	2.8 ± 2.8	0 ± 0	94.4 ± 5.6	5.6 ± 2.8	4.2 ± 4.2
80	33.3 ± 0	67.2 ± 4.3	52.8 ± 3.8	33.3 ± 0	17.8 ± 4.9	6.1 ± 3.0	100 ± 0	13.3 ± 6.7	0 ± 0	100 ± 0	16.1 ± 3.9	0 ± 0
160	-	75 ± 0	58.3 ± 4.8	-	11.7 ± 2.5	11.1 ± 2.8	-	2.8 ± 2.8	8.3 ± 4.2	-	2.8 ± 2.8	8.3 ± 4.2
320	-	62.4 ± 8.8	-	-	8.6 ± 0.3	-	-	2.8 ± 2.8	-	-	2.8 ± 2.8	-

FIGURE 3.2. Mortality and malformation curves for embryos exposed to PbS-MT, PbS-DT, $Pb(NO_3)_2$, and MT and DT ligands. Embryos were exposed to PbS-MT, PbS-DT, or $Pb(NO_3)_2$ at 6 hpf and were evaluated for malformations and mortality at 120 hpf. Mortality (**a**) was statistically significant for PbS-MT (40-320 μg/mL) and $Pb(NO_3)_2$ (only at 320 μg/mL). All surviving embryos exposed to PbS-MT had malformations (average of 5 at 20 μg/mL) (**b**). $Pb(NO_3)_2$-exposed embryos had little to no malformations (<0.25) up until 40 μg/mL, where a steady increase in malformations was observed at 80 and 160 μg/mL. PbS-DT-exposed embryos caused a consistent number of malformations ($\sim$2) at all concentrations. A summary of the statistically significant malformations observed in PbS-MT-, PbS-DT-, and $Pb(NO_3)_2$-exposed embryos is visualized in a table (**e**), where *shaded boxes* indicate statistical significance (Fishers Exact, P <0.05). MT and DT ligands did not induce mortality (**c**) or malformations (**d**) in exposed embryos. Data presented with ** designate statistically significant values (Fishers Exact, $^{**}P$ <0.001). Three replicates, n = 24.

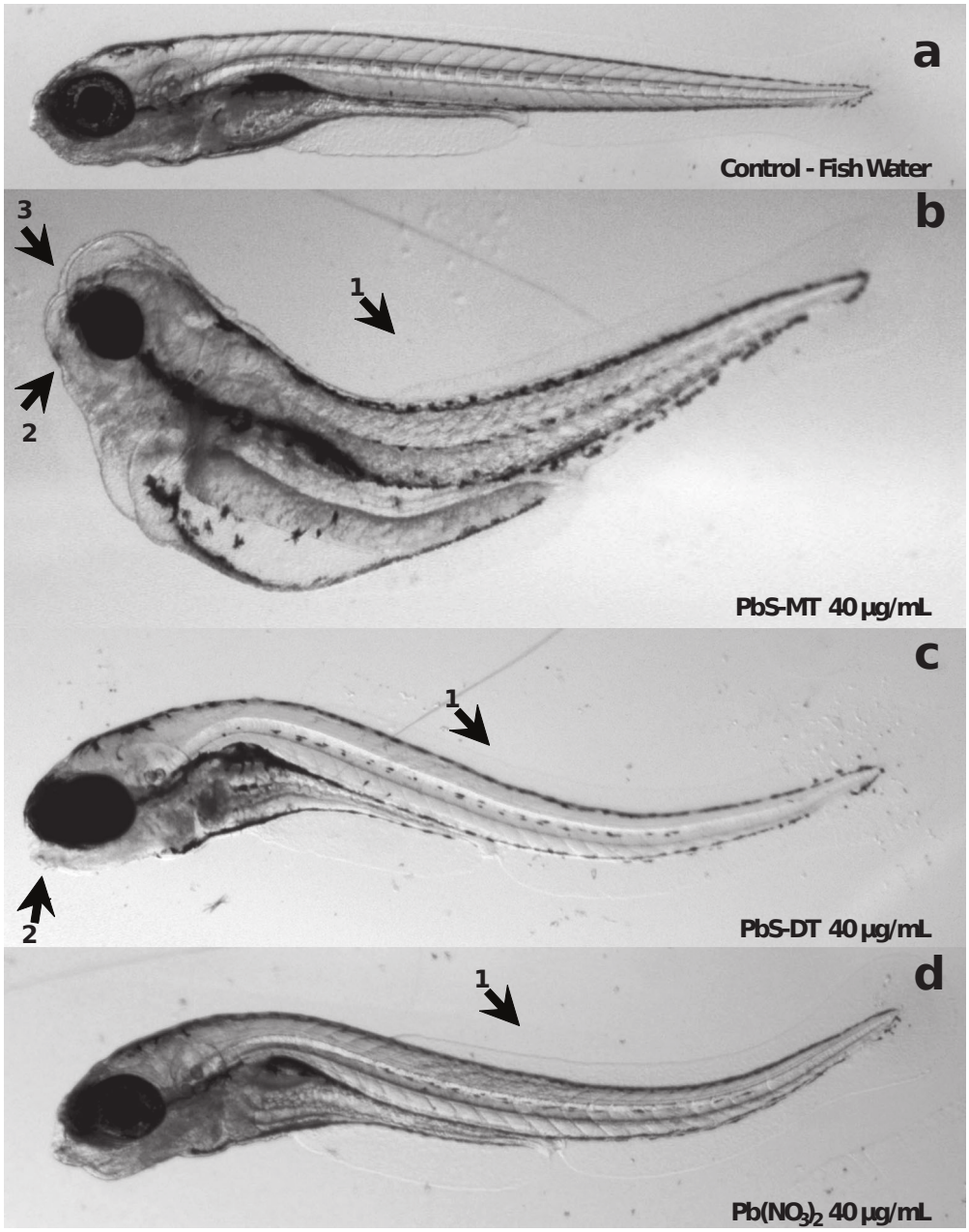

FIGURE 3.3. Representative images of exposed zebrafish embryos. Embryonic zebrafish exposed to PbS-MT nanoparticles (**b**) and $Pb(NO_3)_2$ (**d**) induced a statistically significant increase in bent body axis (*1*), jaw (*2*), and snout (*3*) malformation compared to control (**a**). PbS-DT (**c**) elicited a statistically significant increase in bent body axis and jaw malformation, but not snout abnormalities. All images were taken at 120 hpf, and except for the control embryo, represent exposures at a concentration of 40 μg/mL.

3.3.4. PbS-MT Nanoparticles Decomposed More Readily Than PbS-DT

PbS-MT and PbS-DT nanoparticles are known to precipitate from aqueous solution upon exposure to air (Moody et al. 2008); however, the effects of salinity from exposure to FW were hitherto unexplored. To test the relative stabilities of PbS-MT and PbS-DT nanoparticles in FW, dynamic light scattering (DLS) measurements were performed. Although zebrafish exposures were made using unfiltered nanoparticle solutions, DLS measurements required pre-filtering to remove dust that could affect the scattering experiments. Hydrodynamic radii were measured at times 0, 24, 48, and 120 h. Both samples showed evidence of agglomeration with hydrodynamic radii greater than the average nanoparticle diameter. However, PbS-MT exhibited greater particle size and destabilized more quickly than the PbS-DT samples. PbS-DT samples maintained a consistent particle size of ∼80 nm at 0, 24, and 48 h, but had completely precipitated by 120 h. Conversely, PbS-MT samples had average hydrodynamic radii of 140 nm at 0 h and 340 nm at 24 h and had completely precipitated by 48 h. It was hypothesized that degradation of the nanoparticle cores could follow precipitation and give rise to ionic lead decomposition products. To quantify the concentration of ionic lead after five-day exposure to air (aged), nanoparticle solutions were monitored using an inductively coupled plasma-optical emission spectrometer (ICP-OES). Aged solutions were first centrifuged to remove insoluble species (i.e. precipitated nanoparticles), and the resulting supernatant was digested with nitric acid. The lead content in the supernatants of the aged nanoparticle solutions was 87 ± 0.4 ppm (4% recovery rate) for PbS-MT and 1.075 ± 0.002 ppm (0.02% recovery rate) for PbS-DT, a statistically significant difference. It is important to note that the 87 ppm lead content measured for the aged PbS-MT sample is not due to the original nanoparticles; fresh solutions of PbS-MT

nanoparticles at this concentration are clearly colored due to absorption from the nanoparticle core, whereas the supernatant was colorless. Precaution was taken to ensure that differences in lead concentration seen in the supernatants of the aged solutions were not simply due to different starting concentrations of nanoparticles in the fresh solutions. As a control, aliquots of the fresh nanoparticle solutions were digested with nitric acid, and the total lead content was measured in an analogous manner using ICP-OES. Analysis of the fresh nanoparticle solutions revealed a similar amount of lead present for the two materials (Fig. 3.4). PbSMT had 1,927 $\pm$ 7 ppm of lead, while PbS-DT had 2,270 $\pm$ 10 ppm (Fig. 3.4a), corresponding to approximately 90 and 110% recovered lead for PbS-MT and PbS-DT, respectively (Fig. 3.4b). This study demonstrates that the nanoparticles were decomposing over time, releasing ionic lead into solution.

3.3.5. Lead Quantified in PbS-MT, PbS-DT and Lead Nitrate Exposed Embryos

Inductively coupled plasma-mass spectrometry (ICP-MS) was used to quantify the amount of lead in or tightly associated with the embryo. These measurements were taken to determine whether the differential biological response to the PbS could be explained by differences in particle uptake. Embryos were exposed to concentrations (0-320 μg/mL) of either PbS-MT, PbS-DT, or $Pb(NO_3)_2$, and samples were collected at 12 hpf. At this developmental time point, there was no strict dose-dependent increase in lead uptake at low concentration; however, there was a significant increase in lead concentration following 160 μg/mL lead exposure for PbS-MT. A dose-dependent increase in the tissue concentration of lead was observed in the PbS-DT and $Pb(NO_3)_2$-exposed embryos (Fig. 3.5). PbS-DT-exposed embryos had the highest

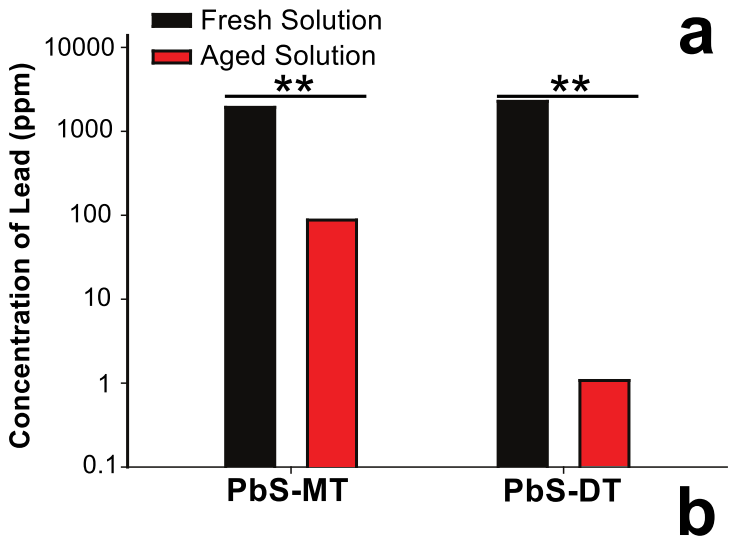

	PbS-MT	PbS-DT
Theoretical Concentration of Pb (ppm)	2189	2129
Measured Concentration of Fresh Solution (ppm)	1927 ± 7	2270 ± 10
Pb Recovered (%)	90 %	110 %
Measured Concentration of Aged Solution (ppm)	87 ± 0.4	1.075 ± 0.002
Pb Recovered (%)	4 %	0.02 %

FIGURE 3.4. Concentration of lead (Pb) in fresh and aged PbS-MT and PbS-DT solutions. Nanoparticle solutions that were initially opened (fresh) and left to oxidize for 5 days (aged) were digested with nitric acid, and Pb concentration was measured 18 h later (**a**) with ICP-optical emission spectrometer (OES). Expected Pb percent recovery concentrations were calculated for both nanoparticles for fresh and aged solutions (**b**). Data presented with ** designate statistically significant values (Student t test, $^{**}P < 0.001$).

lead level for all concentrations up until 160 μg/mL, where PbS-MT embryos had significantly more lead tissue burden.

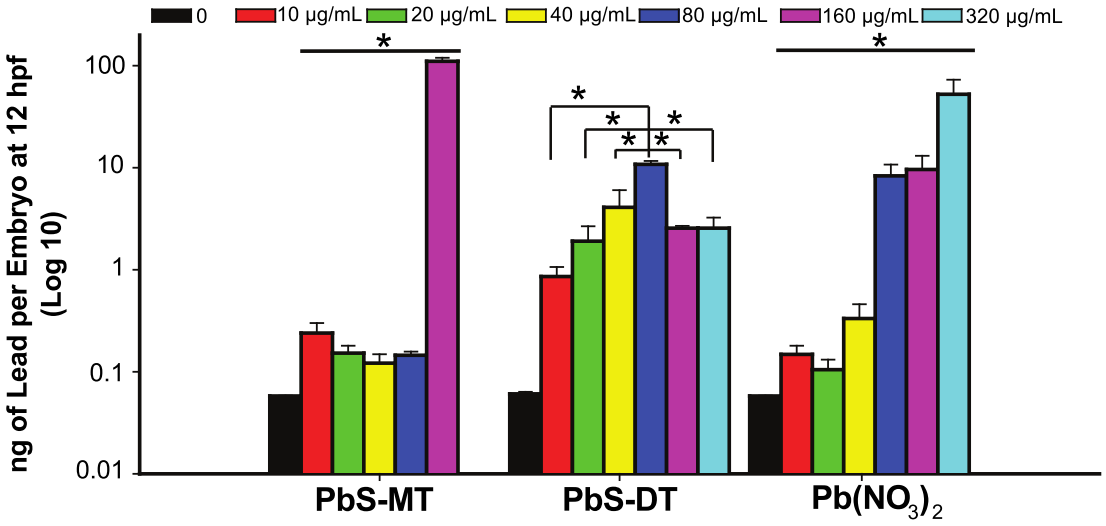

FIGURE 3.5. Tissue concentration of lead in embryos exposed to PbS-MT, PbS-DT and $Pb(NO_3)_2$. Embryos were exposed to 10-320 μg/mL solutions of PbS-MT, DT, and $Pb(NO_3)_2$ at 6 hpf and sampled at 12 hpf. Embryos exposed to PbS-MT at 320 μg/mL did not survive to the time of sampling. Both $Pb(NO_3)_2$ and PbS-DT tissue concentration followed a dose-dependent manner, except PbS-DT only followed this trend until 80 μg/mL. Data presented with * designate statistically significant values (Kruskal-Wallis ANOVA-Tukey test, P <0.05).

3.4. Discussion

In this *in vivo* study, we find that the biological response following exposure to lead sulfide nanoparticles (PbS-NPs) is influenced greatly by surface functionalization. Two major effects can be gleaned from the exposure trials. First, DT-functionalized PbS nanoparticles (PbS-DT) elicit fewer responses than MT-functionalized PbS nanoparticles (PbS-MT). Exposure to PbS-MT induces 100% mortality at 160 μg/mL in zebrafish embryos at 120 hpf and also a variety of sublethal malformations. Conversely, embryos exposed to PbS-DT elicit little to no mortality and fewer

sublethal adverse responses. Second, PbS-MT exposure causes significantly more, and PbS-DT significantly less, mortality than the ionic lead source, lead nitrate ($Pb(NO_3)_2$). PbS-MT- and $Pb(NO_3)_2$-exposed embryos were morphologically similar at concentrations near the onset of mortality. The simplest explanation for these results is a correlation between toxicity and nanoparticle stability. Destabilization of the nanoparticles occurs over the course of the exposure. The two ligands offer differential resistance to this destabilization, leading to differential biological responses in the embryos.

Nanoparticle stability can greatly influence exposure of the core surface. Thiolate ligands at the metal chalcogenide nanoparticle-ligand interface are susceptible to oxidative decomposition (Aldana et al. 2001, Moody et al. 2008). This instability can lead to ligand desorption, resulting in particle agglomeration, greater exposure of the nanoparticle core, and decomposition of the core with the possible generation of soluble ionic lead species.

To our knowledge, no prior toxicity studies have been conducted on PbS-NPs; however, lessons can be learned from studies on other material sets. In general, nanoparticles have been observed to cause cytotoxicity (Lewinski et al. 2008), oxidative stress (Long et al. 2006), and immune responses (Dobrovolskaia and McNeil 2007), either through biochemical interactions with the nanoparticles themselves or from their toxic decomposition products. The ligand shell can influence toxicity by affecting nanoparticle uptake and distribution in biological systems (Seale-Goldsmith and Leary 2009) or as an integral part of the entire nanoparticle-ligand assembly. The accessibility of the nanoparticle core has also been implicated as a potentially important factor. Nanoparticles that have a denser coverage of surface ligands, or are

encapsulated by an inert material (Zhang et al. 2006), are generally less toxic than those particles that offer greater access to the core.

Prior comparisons between PbS-MT and PbS-DT nanoparticles have shown that both materials are susceptible to oxidative decomposition in aqueous solution (Moody et al. 2008). Specifically, the thiol head groups of both MT and DT ligands oxidize to form disulfides, which bind poorly to the nanoparticle surface. The MT ligands oxidize relatively quickly, resulting in rapid ligand desorption and nanoparticle precipitation. Oxidation of the DT ligands proceeds more slowly, and in a manner, which leaves the ligands partially attached to the nanoparticle surface. Although these studies were not conducted in fish water, they suggest that differential decomposition could play a role in the observed biological effects.

In this study, differential stability resulting from different surface functionalization is implicated as the major contributor to the differential biological response to the nanoparticles. DLS measurements performed on nanoparticles in fish water showed that although solution salinity affects agglomeration, PbS-DT nanoparticles are more stable than PbS-MT nanoparticles, just as in prior studies using nanoparticle solutions in deionized water. Core size was not a significant variable in the differential response. Direct comparisons of PbS-MT and PbS-DT nanoparticles were conducted using nanoparticles prepared from the same OLA-capped precursor, and exhibited similar core-related properties. Effects from the ligands themselves were also ruled out as significant factors, as they induce no to low incidence of mortality and morbidity. It is certainly possible that the differential response of the nanoparticles is due to differences in the biological interactions of the entire intact nanoparticle structure. We look to oxidative stability as the likely differentiator, however, because it is the

most notable difference in the physicochemical properties of the nanoparticles. The differential oxidative stability is due to the ligand head group (monothiol vs. dithiol).

The mechanism for how the different decomposition rates of PbS-MT and PbS-DT result in differential nanoparticle-biological interactions remains unclear. Two likely causes for the toxicity are interactions with either (1) presumably ionic lead decomposition products or (2) the exposed nanoparticle cores. The primary reason that the interaction cannot be distinguished is the challenge of quantifying dose. Two studies shed light on the dose of either nanoparticles or its decomposition products received by the embryos. The first is the ICP-OES measurements performed on aged nanoparticle solutions. Soluble lead products are observed during the oxidative decomposition and precipitation of the nanoparticles, with a much greater concentration of ionic lead observed for PbS-MT relative to PbS-DT. The fresh PbS-MT and PbS-DT solutions began with similar concentrations of nanoparticles. However, analysis of the aged solutions shows that the two ligands are not equal in their protection of the nanoparticle surface; as they decompose and precipitate, MT-capped nanoparticles leach ∼80 times more ionic lead into solution than DT-capped nanoparticles. As the PbS-NP solutions age, ligands are oxidized and desorb from the nanoparticle surface, resulting in nanoparticle precipitation. During this process, lead can leach from exposed sites on the nanoparticle cores. The concentration of soluble lead decomposition products observed in the aging studies was below the onset of toxicity at 160 μg/mL for $Pb(NO_3)_2$, even given the much higher concentration (3,000 μg/mL) of nanoparticles used for the ICP-OES studies than for the toxicity studies. What is important, however, is not simply the concentration of soluble lead in the fish water but the actual dose received by the embryos. This dose is dependent on the distribution of nanoparticles, which suggests that the PbS-NPs are

associating with the embryos in the exposure media and resulting in localized soluble lead decomposition products.

Tissue uptake studies were performed in an attempt to better define the dose. In these studies, exposed embryos were washed and then analyzed for lead content using ICP-MS. One limitation of this technique is that no distinction can be made between lead tightly bound to or within the embryo. Visual inspections of the embryos after exposure revealed signs of adsorbed nanoparticles. It is hypothesized that at higher concentrations, nanoparticle solutions are more susceptible to agglomeration and that these agglomerates may adhere preferentially to the embryos. This effect would substantially increase the local concentration of lead around the embryos, leading to increased uptake relative to a uniform solution distribution. Note that the uptake studies were performed at early exposure times. At these early times, only the PbS-MT induced substantial mortality at 320 μg/mL. Near the onset of this mortality (160 μg/mL), the PbS-MT nanoparticles exhibited a sharp increase in uptake to levels higher than those observed for either the PbS-DT or $Pb(NO_3)_2$ exposures.

The uptake and decomposition studies do not definitively distinguish between direct nanoparticle toxicity and nanoparticle decomposition product toxicity. The differential toxicity of the PbS-MT vs PbS-DT nanoparticles can be explained by greater exposure of the nanoparticle core in the former during decomposition. This mechanism also provides a simple explanation for the greater toxicity of the PbS-MT nanoparticles relative to $Pb(NO_3)_2$. Alternatively, nanoparticle decomposition products could be responsible for the increased toxicity of PbS-MT relative to PbS-DT consistent with the greater amount of lead observed to leach from aged solutions of the PbS-MT. The enhanced toxicity of PbS-MT relative to $Pb(NO_3)_2$ is explained

by the agglomeration of nanoparticles on or in the embryos, which acts to increase the local lead concentration. Such a local increase is consistent with the substantial lead uptake observed near the onset of toxicity (160 μg/mL) in the 12-hpf uptake studies.

Further studies will be needed to differentiate between the biological interactions with either the nanoparticle cores and/or soluble decomposition products. Regardless, these studies illustrate the substantial changes in nanoparticle toxicity that can be induced by a relatively minor change in ligand composition. With the knowledge that manipulating physicochemical properties of nanoparticles results in differential biological responses, a systematic methodical use of the rapidly developing embryonic zebrafish model will aid in elucidating the key design principles to develop minimal to non-toxic nanoparticles.

Additionally, these studies using the PbS-NPs highlight the important role that nanoparticle decomposition plays in toxicity. The possibility of ionic lead leaching from the nanoparticles also suggests that more studies should be conducted to understand the poorly known mechanisms of lead toxicity. Physicochemical characterization of NPs in their synthesis media is important, but as demonstrated in these studies, it is critical to conduct characterization of the NPs in exposure media in parallel to toxicity assessments to gain a better understanding of aggregation state and other physicochemical properties. As the field of nanotechnology expands and matures, greater understanding of the nanomaterial-biological interface will be imperative.

3.5. Conclusions

Data presented demonstrate the usefulness of the embryonic zebrafish model as a platform to rapidly assess the nanomaterial-biological interaction of nanoparticles. With this set of nanoparticles, different biological responses between PbS-MT and PbS-DT nanoparticles were attributed to differences in their rates of decomposition. This study illustrates the importance of using well-characterized nanoparticles both from the start and over time. It also opens discussion on the hitherto unexplored biological interactions of lead sulfide nanoparticles. Use of the embryonic zebrafish to conduct nanomaterial-biological interaction assessments will increase the speed at which key physicochemical properties will be identified and used to implement a design rule to produce safer nanomaterials.

3.6. Bridge to Chapter IV

Chapter III explored the toxicology of lead sulfide nanoparticles functionalized with two different short-chain, sulfonate ligands. The results from these studies showed that the nature of the ligand binding group to the nanoparticle surface plays an important role in influencing bioavailability, and thus toxicity, to biological systems. These types of studies are important, even at early stages in the design cycle, to determine the risk associated with implementing the use of novel materials in real-world applications. This study exemplifies the fact that toxicity can sometimes be mitigated through very subtle changes to the chemical structure of the nanoparticle-ligand complex, often times with little impact on material performance.

In Chapter IV, the emphasis is changed from investigating the physical properties of I-NC solutions (examined in Chapters II and III), to the opto-electrical properties of nanoparticle thin films. The lessions learned about the effects of ligand head group

– improved stability and reduced toxicity associated with PbS-DT nanoparticles, relative to PbS-MT nanoparticles – were taken into account, and the focus of Chapter IV is exclusively on PbS-DT nanoparticles.

CHAPTER IV

MOBILE IONS INFLUENCE CHARGE INJECTION AND PHOTOCONDUCTIVITY IN IONICALLY-FUNCTIONALIZED LEAD SULFIDE NANOCRYSTAL THIN FILMS

This chapter is being prepared for submission to *The Journal of Physical Chemistry C*, and includes co-authored material with Mark C. Lonergan.

4.1. Introduction

Semiconductor nanocrystals (SC-NCs) have been widely studied for their unique optical and electrical properties. Their ease of processability added with the fine control afforded over their size, shape, composition, and surface functionalization make SC-NCs attractive candidates for a wide variety of applications[1]. One class of SC-NCs – the lead chalcogenides, PbE (E = S, Se, Te) – have been of particular interest due to their narrow electronic band gap, which renders them optically-active in the near-infrared (NIR) region of the electromagnetic spectrum[2]. Sensitivity to this region is important for applications in several types of photonic devices; e.g. NIR-LEDs[3,4], photovoltaics[5,6,7], and photodetectors[8,9,10]. One of the challenges in realizing the potential of PbE-NCs (and SC-NC-based devices, in general) has been the poor electrical transport properties of SC-NC thin films relative to traditional, bulk-crystalline materials[1]. In this study, we focus on the role that incorporation of ionic functionality into PbS-NCs has on transport properties of the resulting thin films.

First-generation PbE-NC thin films typically consisted of disordered arrays of particles separated by electrically insulating organic ligand shells. Significant progress

has been made towards improving the electronic transport behavior of SC-NC thin films through reduction of the inter-particle spacing. Replacement of long-chain, fatty acid or phosphine ligands – used in the synthesis to control growth and solubility – with short-chain and/or cross-linking molecules has been shown to enable closer packing of NCs in the solid state, which results in orders-of-magnitude improvement in conductivity[11,12,13,14,15]. Advances in thin-film fabrication, particularly the use of layer-by-layer (LbL) deposition techniques, have reduced film defects (e.g. cracking) associated with solid-state ligand exchanges that had plagued early work with chemically-treated SC-NC devices[16]. LbL deposition allows for the formation of thick, crack-free films of SC-NCs functionalized with the shortest possible alkyl ligands, which enables fabrication of efficient sandwich devices[16].

Additional improvements have been achieved through careful control of oxidation and thermal annealing of PbE-NC thin films[11,12,17]. Oxidation and annealing can improve film conductivity and reduce geminate recombination of photogenerated charge carriers through the removal of surface ligands or introduction of thin oxide layers that act as surface traps[18,19,20].

Despite all the recent work, there still remain new avenues for improving SC-NC device performance. Lessons can be learned from other disordered semiconductor systems. In particular, polymer light-emitting electrochemical cells (LECs) – which consist of semiconducting conjugated polymers blended with salts – have demonstrated that finer control over internal electric fields allow for improvement in device efficiencies. In LECs, the presence of mobile ions (from the added salts) facilitate electronic carrier injection from the electrodes into the polymer layer where they can recombine to emit light[21].

There are several reports of SC-NCs functionalized with ionic ligands. Typically, the primary use of ionic ligands (e.g. carboxylic acids) has been to impart water solubility to SC-NCs, e.g. for biological applications[22]. Some recent reports, however, have also examined the use of small, inorganic ions as passivating agents that allow for close packing of particles for improved charge transport in SC-NC solids[23,24]. Additionally, there is one report of a field-effect transistor (FET) fabricated from a thin film of PbSe nanocrystals and using an ion-gel as a dielectric gate material[25]. The high dielectric associated with the ion-gel facilitated accumulation of large amounts of holes and electrons while gating, which, in turn, improved charge transport between source and drain electrodes relative to devices using a traditional SiO_2 gate material. However, mixed-ionic-electronic conductive (MIEC) systems – analagous to those seen in LECs – are absent in the SC-NC literature.

Previously, we reported a solution-phase exchange procedure for PbS-NCs functionalized with a short-chain ligand – sodium 2,3-dimercaptopropanesulfonate (DT)[26]. The denser packing of nanocrystals afforded by the reduced steric bulk of the DT ligand shell, relative to films of bulkier, oleic acid-functionalized PbS nanocrystals, allows for improved charge transport through the PbS nanocrystal films. Additionally, the photoconductive response was increased with the DT ligand.

Here, we explore another key structural feature of the DT ligand – the sulfonate tail group – which consists of a negatively charged sulfonate group covalently bound to the carbon backbone, and a positively charged counter ion, electrostatically bound to the sulfonate. We show that this "ionic functionality" provides another handle by which to further tune the electronic properties of PbS nanocrystal thin films. Proper selection of counter ion allows for control over conductivity and photoconductivity.

As-synthesized PbS-DT NCs contain a native Na^+ counter ion to the sulfonate ligand. We show that thin films of these PbS-DT(Na) NCs exhibit up to a two-order-of-magnitude increase in conductivity and photoconductivity under application of a sustained electrical bias. We attribute this effect to a field-induced displacement of Na^+ ions which aid in electronic charge carrier injection/extraction at the electrode interface through the creation of space-charge regions within the film. Additionally, we report the preparation of PbS-DT thin films functionalized with a series of different counter ions through a facile ion exchange procedure. The identity of the counter ion is shown to influence the absolute magnitude of the conductivity and the change in conductivity with time under bias in PbS-DT thin films. The time-dependent behavior is suppressed as counter ions of greater size and valency are incorporated.

4.2. Results

4.2.1. Preparation of PbS-DT Nanocrystals

The synthesis of PbS nanocrystals functionalized with sodium 2,3-dimercapto-propanesulfonate (DT) has been reported previously[26]. Briefly, oleic acid capped PbS nanocrystals were synthesized using the hot-injection method first reported by Hines and Scholes[27]. First, lead oleate was formed *in situ* by heating a solution of lead oxide in oleic acid under vacuum. To this lead precursor mixture, a solution of hexamethyldisilathiane in 1-octadecene was quickly injected to initiate PbS nanocrystal nucleation. Subsequent workup and purification resulted in oleic-acid-capped PbS nanocrystals (PbS-OLA).

Functionalization of PbS nanocrystals with the DT ligand was performed via a biphasic exchange procedure. A solution of PbS-OLA nanocrystals in toluene was mixed with an aqueous solution of DT and vigorously shaken until the

nanocrystals migrated into the aqueous layer. Purification yielded DT-functionalized PbS nanocrystals (PbS-DT) with an average diameter of 3.0 nm, and a $\lambda_{max} = 1168$ nm, (see Figure 4.1).

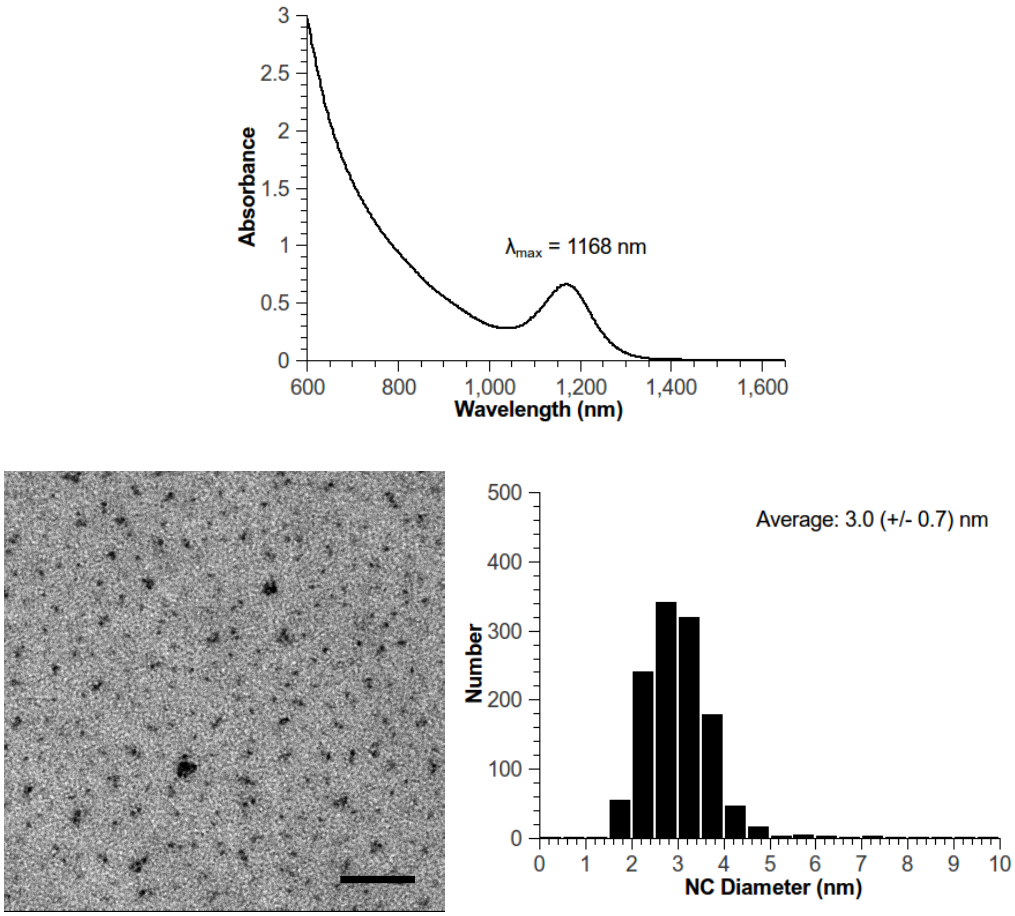

FIGURE 4.1. Size data for a typical PbS-DT(Na) nanocrystal batch. (*top*) vis-NIR absorption spectrum of PbS-DT(Na) nanocrystals in aqueous solution. (*bottom left*) A typical raw TEM image of PbS-DT(Na) nanocrystals with 50 nm scale bar. (*bottom right*) A histogram of NC diameters extracted from TEM images of PbS-DT(Na) nanocrystals.

4.2.2. Ion Exchange of PbS-DT Nanocrystals

Two separate methods for ion-exchange were used to replace the native Na^+ counter ions on PbS-DT nanocrystals. First, exchange with monovalent cations (e.g.

NMe_4^+) was performed by passing an aqueous solution of PbS-DT(Na) nanocrystals down a column filled with a strong-cation exchange resin. Films cast from these solutions showed quantitative exchange of Na^+ for NMe_4^+ via XPS analysis (see Figure 4.2).

The preferential binding of divalent cations (i.e. Ca^{2+}) on the cation exchange resin necessitated the use of a solid-state process in order to functionalize PbS-DT nanocrystals with Ca^{2+} ions. An IDE (see below for description) was coated with a thin film of PbS-DT(Na), dried under vacuum, and then exposed to a solution of $Ca(NO_3)_2$ to swap Na^+ ions for Ca^{2+} ions in the film. XPS analysis showed quantitative exchange of Na^+ for Ca^{2+}, with no evidence of leftover nitrate salts adhered to the film (see Figure 4.2).

4.2.3. Photoconductive Behavior of PbS-DT Nanocrystal Thin Films

To probe the electrical properties of PbS-DT nanocrystals, thin films were cast onto an open-face, interdigitated gold electrode (IDE). IDEs were pre-patterned via standard photolithography methods with a gap spacing of 5 to 9 μm, and an electrode height of $\sim$40 nm. Nanocrystal films were deposited via spin coating, which resulted in an average film thickness of $\sim$40 nm. The coated IDE (henceforth, referred to as a "device") is open-face, has two symmetric electrodes, and behaves as a photoconductor. Figure 4.3 depicts the spectral response of a PbS-DT(Na) device under an applied bias of +10 V. In the *top* plot, the device spectral response overlaps well with the absorption spectrum of the PbS-DT nanocrystal solution. In the *bottom left* plot, the near-infrared spectral response as a function of light intensity was investigated. In general, the responsivity of PbS-DT devices increases

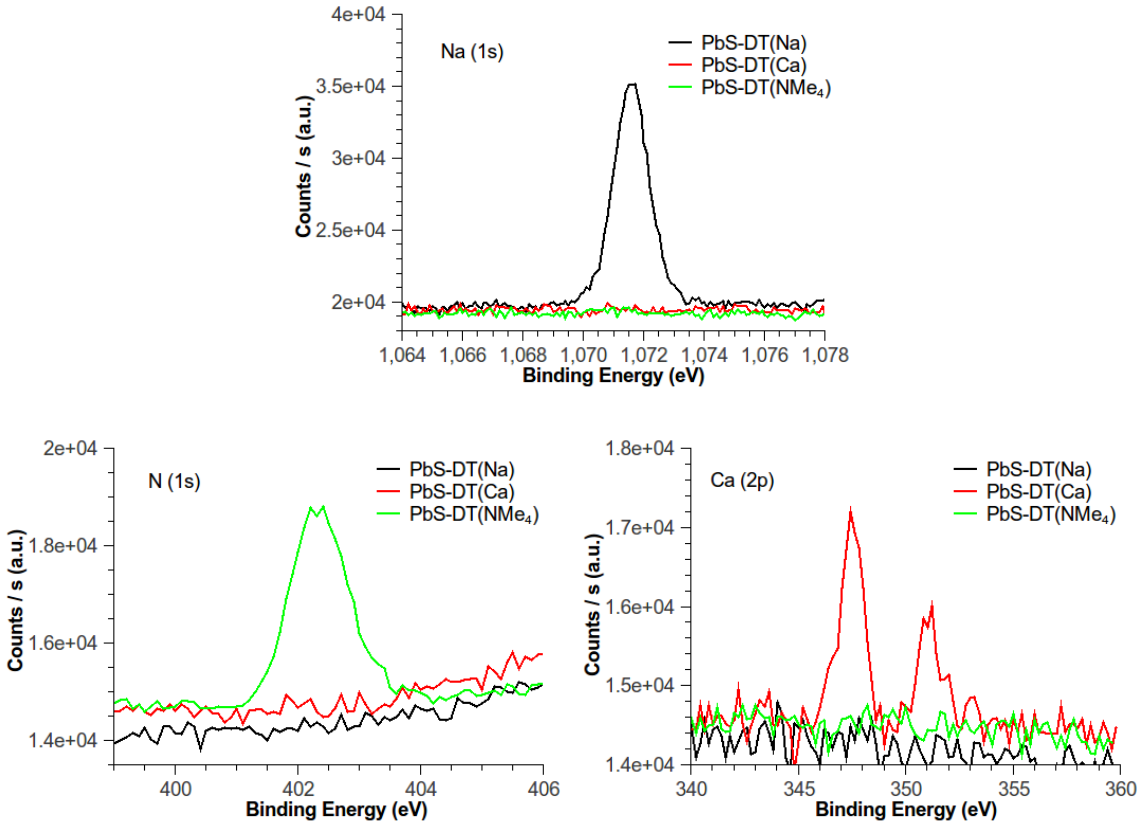

FIGURE 4.2. X-ray photoelectron spectroscopy (XPS) of PbS-DT(Na), PbS-DT(NMe_4), and PbS-DT(Ca) thin films. Selected energy regions for Na (*top*), N (*bottom left*), and Ca (*bottom right*).

with decreasing light intensity. Finally, in the *bottom right* plot, the switching speed of the photoresponse was explored.

Due to the time-dependent effects associated with PbS-DT(Na) devices (discussed in detail in the following section), both sets of measurements of Figure 4.3 were performed once the device had been subjected to a sustained +10 V bias for ∼7 hr prior, and reached steady-state.

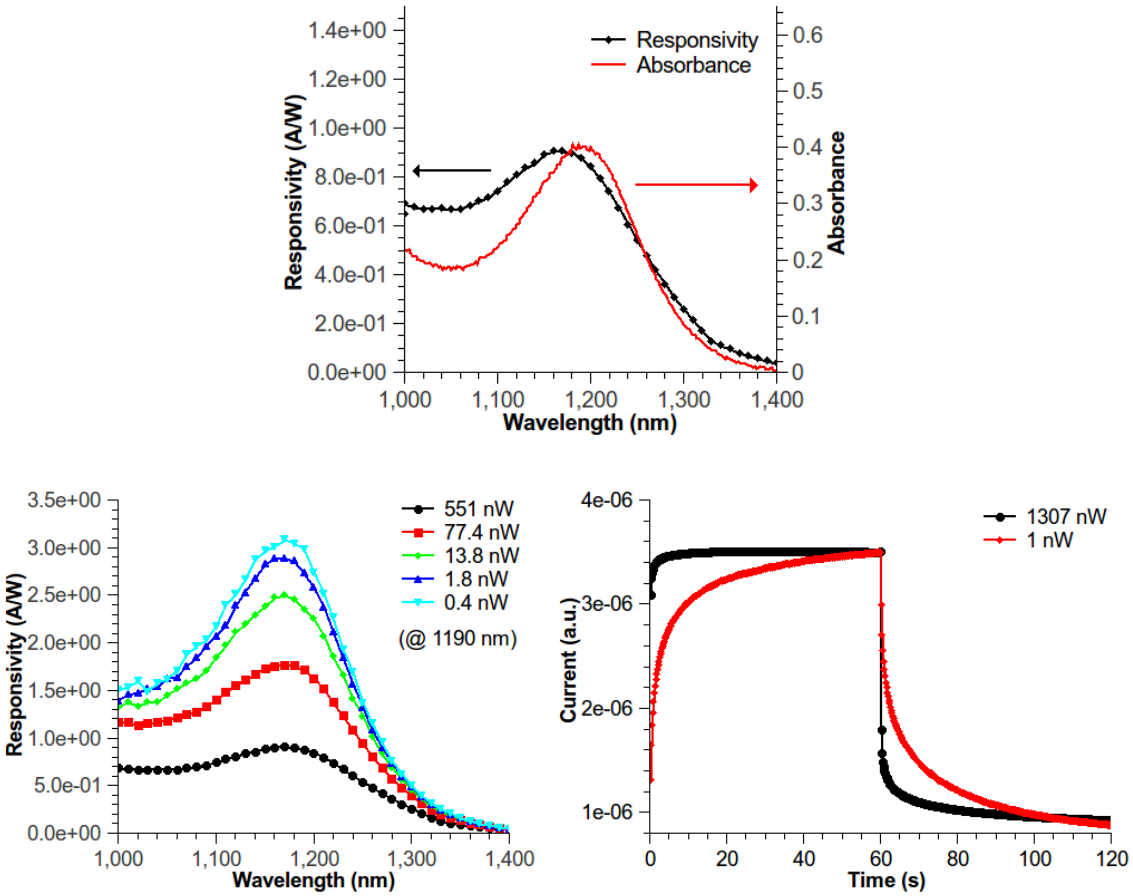

FIGURE 4.3. Photoresponse of a PbS-DT(Na) thin-film device. (*top*) Spectral response of a PbS-DT(Na) device under +10 V bias overlaid with an absorption spectrum of the corresponding nanocrystals in solution prior to deposition. (*bottom left*) Spectral response of the same PbS-DT(Na) device under +10 V applied bias as a function of light intensity. (*bottom right*) Time response of the device current for the same device at the start (0 to 60 s) and finish (60 to 120 s) of a 60 s exposure to 1190 nm light. Total device current (in arbitrary units) is overlaid for exposures to two different light intensities. Note that low light exposure curve was expanded for ease of comparison. (*Also:* Light chopper was removed for this experiment.) All three sets of measurements were performed consecutively following a long applied bias of +10 V. Bias was maintained throughout without break. Lines serve only as guides for the eye.

4.2.4. Time-Dependent Behavior of PbS-DT Nanocrystal Thin Films

PbS-DT nanocrystal thin films functionalized with native Na^+ counter ions exhibit a time-dependent current response to an applied potential. Figure 4.4

illustrates this time dependency for a typical PbS-DT(Na) thin film cast onto an interdigitated gold electrode. PbS nanocrystal thin films also exhibit photoconductive gain when exposed to light. To better understand the effects of a constant bias on ionically-functionalized PbS nanocrystal films, the current response was monitored under both dark and light conditions. Figure 4.4 (*top*) depicts the "dark" current response of a typical PbS-DT(Na) IDE to a series of voltages. For all applied biases (above a certain threshold), the dark current increases as a function of time until it reaches a quasi-steady-state value. The magnitude of the current increase is proportional to the magnitude of the applied bias.

Figure 4.4 (*bottom left*) depicts the evolution of the spectral response of the PbS-DT(Na) device during the application of the +10 V bias (shown in light blue in the top plot). Like the dark current, the responsivity increases with time under bias. In the *bottom right* plot, the light and dark currents measured during the +10 V bias are overlayed, and are shown to increase in a similar manner.

Some variation in response was seen between samples of PbS-DT(Na) devices. In particular, sample variation was observed to affect the time response of the biased photoresponse. During the potential steps plotted in Figure 4.4, the bias on the device was held constant, and the device intermittently exposed to illumination (the data gaps). After each light exposure, there was a relaxation period in which the device switched from a high conductivity "Light" state, back to a low conductivity "Dark" state. As it relaxed, the conductivity would sometimes drop below the value reached prior to the illumination. The magnitude and duration of this dip varied slightly from sample to sample.

The time-dependent behavior of PbS-DT nanocrystal thin films was found to be highly dependent on the identity of the counter ion to the sulfonate group of the

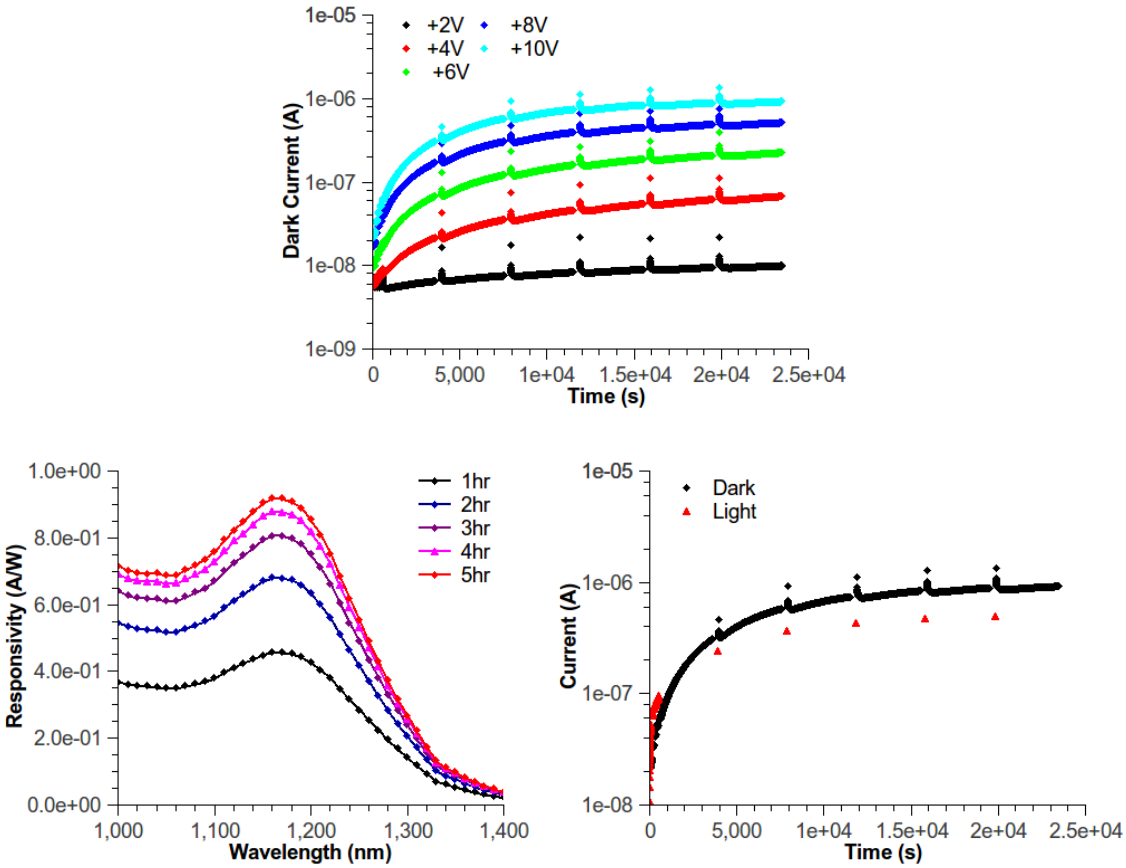

FIGURE 4.4. Time-dependent device response of a typical PbS-DT(Na) thin-film device under bias. (*top*) Current response of a PbS-DT(Na) thin-film device to a series of applied voltages. All data points reflect "dark" measurements. Data gaps regularly spaced along the curves represent brief periods where the photoconductive response was probed (see bottom left plot). After each of these light exposures, the films undergo a brief relaxation period as they return to equilibrium in the "dark" conductive state. (*bottom left*) Spectral response curves recorded during the data gaps of the +10 V potential step (shown at top in light blue). The applied +10 V bias was kept constant as the device was switched between dark and light conditions. (*bottom right*) Overlay of the light and dark currents under +10 V bias. The dark current was measured as the total device current through the source-measure unit of the Agilent 4156C. The light current is the lock-in current acquired through the lock-in amplifier under 35 Hz chopped illumination of 1190 nm.

DT ligand. To explore this effect, the PbS-DT films were prepared with counter ions that varied in size and valency. To minimize any effects of batch variability,

all ion-exchanged samples were derived from the same parent, PbS-DT(Na) batch. Figure 4.5 and Figure 4.6 plot the time dependent behavior of PbS-DT devices in the dark and light, respectively, which contain either Na^+, NMe_4^+, or Ca^{2+} ions. Compared with PbS-DT(Na) devices, both PbS-DT(NMe_4) and PbS-DT(Ca) devices showed a relatively time-independent response to a sustained voltage. This "flat" response was observed for both the dark and light measurements. Additionally, PbS-DT(NMe_4) devices had relatively lower, and PbS-DT(Ca) devices relatively higher, initial conductivities than the PbS-DT(Na) devices.

To ensure that the suppressed time-dependent behavior of PbS-DT(NMe_4) and PbS-DT(Ca) films was not simply an annomalous effect of the ion exchange process, a control experiment was run where natively functionalized PbS-DT(Na) nanocrystals were exchanged on a Na^+-form ion-exchange column. The resulting device showed time-dependent behavior analogous to the non-exchanged PbS-DT(Na) devices, see Figure A.2. Additionally, the column-exchange method was successfully tested with two other small, monovalent cations – Li^+ (78 pm) and NH_4^+ (143 pm). IDEs of these two materials (*data not shown*) exhibited time-dependent behavior analogous to devices of PbS-DT(Na). An attempt to fabricate a Na^+ control sample via the solid-state exchange method was unsuccessful. A PbS-DT(Na) thin film device exposed to an aqueous solution of $NaNO_3$ showed suppressed spectral features and reduced responsivity, suggesting some form of device degradation.

4.2.5. After-Bias Behavior

Following a potential step, PbS-DT nanocrystal films exhibited a relatively long-lived "memory" of the applied bias. To explore this behavior, a fast current-voltage sweep was performed immediately after removing the potential step bias.

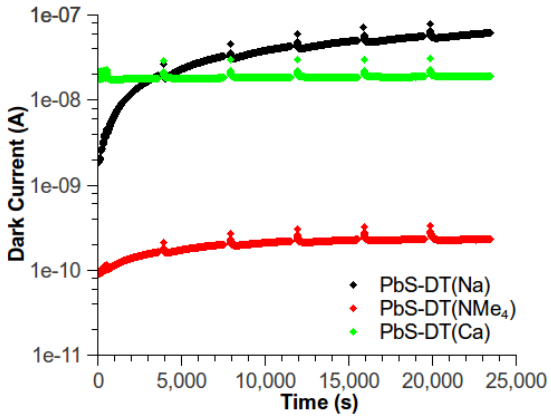

FIGURE 4.5. Effect of counter ion on the time-dependent dark current of PbS-DT thin-film devices under bias. Combined dark current curves for PbS-DT nanocrystal thin films containing Na^+, NMe_4^+, and Ca^{2+} counter ions.

In Figure 4.7, the IV plots show that PbS-DT(Na) films exhibit increasing degrees of rectification following an increase in the magnitude of the applied bias, while PbS-DT(NMe_4) and PbS-DT(Ca) films show approximately linear current-voltage response.

The short-circuit behavior of PbS-DT films was also monitored following the applied bias of a potential step. Figure 4.8 shows short-circuit spectral response sweeps for PbS-DT films containing either Na^+, NMe_4^+, or Ca^{2+} counter ions. Each plot contains two sweeps: one taken before, and one taken after an applied +10V bias. Of the three, only PbS-DT(Na) films exhibit a short-circuit photocurrent that is measurably different from the baseline, "relaxed" state (i.e. before the potential step).

4.2.6. Light Emission from PbS-DT Thin Films

Ions in MIEC systems are known to aid in electron/hole injection through modification of the electric field strength at the semiconductor-electrode interface. This

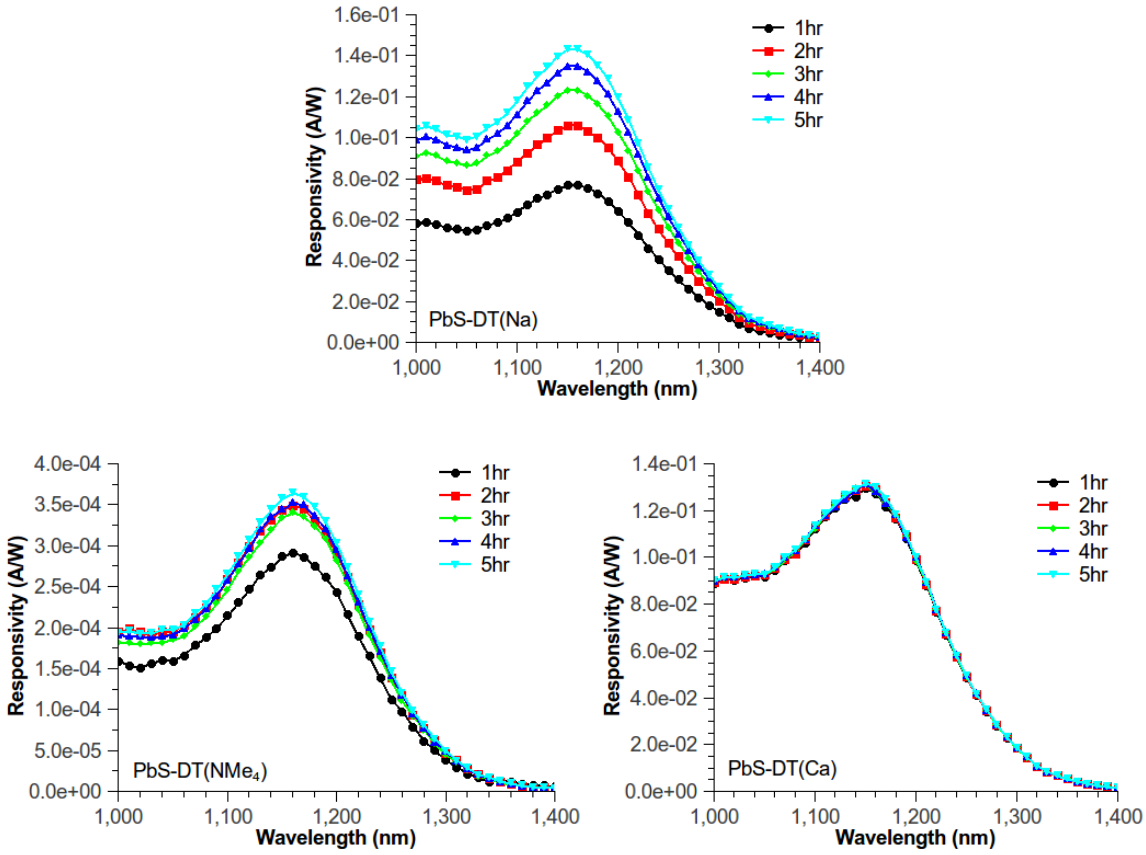

FIGURE 4.6. Effect of counter ion on the time-dependent responsivity of PbS-DT thin-film devices under bias. Spectral response curves measured for PbS-DT(Na) (*top*), PbS-DT(NMe_4) (*bottom left*), and PbS-DT(Ca)(*bottom right*) films, as a function of time under +10 V bias.

effect can be harnessed to improve the electronic carrier balance to achieve greater electroluminescent efficiencies in LEC architectures. To test if ions were enabling electroluminescence in our PbS-DT thin films, devices were placed in close proximity to a commercial InGaAs detector, and the emitted light intensity monitored as a function of device time under bias. Figure 4.9 plots the total device current and InGaAs detector response as a function of time for two PbS-DT devices – one with Na^+ ions and the other with Ca^{2+} ions.

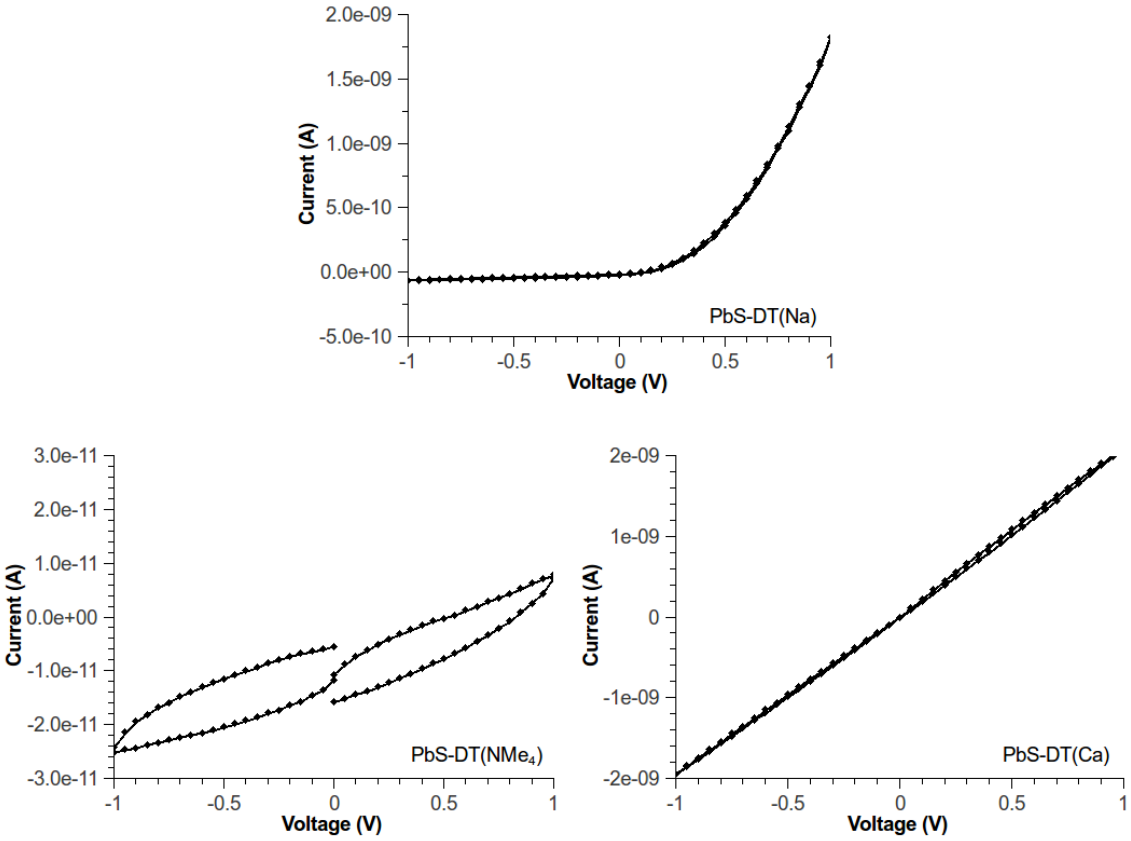

FIGURE 4.7. Current-voltage behavior of PbS-DT(Na), PbS-DT(NMe_4), and PbS-DT(Ca) thin-film devices after bias. Current-voltage sweeps recorded for PbS-DT(Na) *(top)*, PbS-DT(NMe_4) *(bottom left)*, and PbS-DT(Ca) *(bottom right)* thin films immediately following removal of an applied bias of +10 V. All sweeps begin at 0 V and proceed first positive to +1 V, then negative to -1 V, and finally, back to 0 V. Rectification increases with the identity of the counter ion in the order of: Ca^{2+} <NMe_4^+ <Na^+.

NIR electroluminescence from PbS-DT(Na) IDEs is consistent with fluorescence measurements performed on similarly-prepared PbS-DT(Na) solutions (shown in Figure A.1). These solutions had an emission peak at 1261 nm, representing a Stokes shift of 107 nm from the absorption spectra lambda-max. The very low emission intensities from biased PbS-DT(Na) IDEs made spectral resolution infeasible.

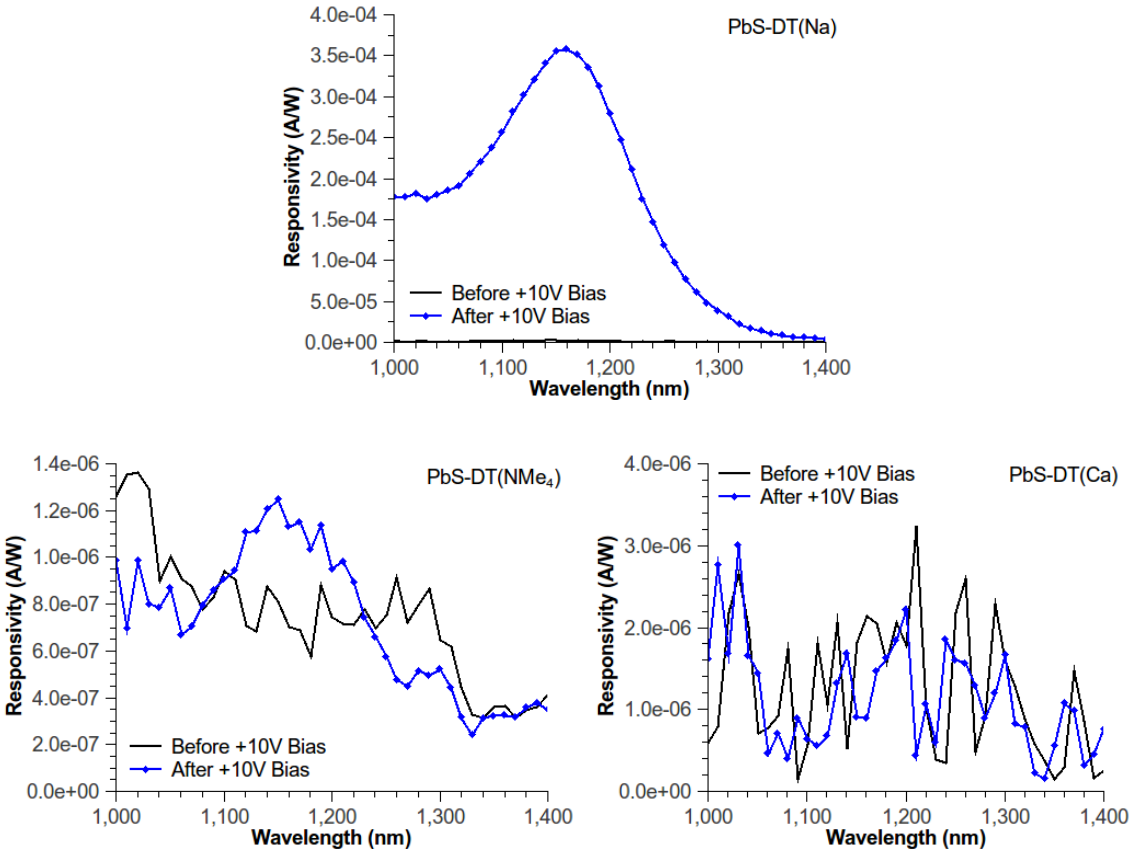

FIGURE 4.8. Short-circuit spectral response sweeps for PbS-DT(Na), PbS-DT(NMe_4), and PbS-DT(Ca) thin-film devices. Short-circuit spectral response curves are plotted for PbS-DT(Na) *(top)*, PbS-DT(NMe_4) *(bottom left)*, and PbS-DT(Ca) *(bottom right)* thin films ∼20 min. following removal of an applied bias of +10 V. The magnitude of the photovoltaic effect increases with the identity of the counter ion in the order of: Ca^{2+} <NMe_4^+ <Na^+.

4.3. Discussion

We propose that the presence of tethered ionic groups to the surface of the lead sulfide nanocrystals is the main factor governing the long-lived time response of PbS-DT thin films. There are three major results that suggest ion motion, and its effects on electronic charge carriers, is the primary cause of the observed electrical behavior of PbS-DT nanocrystal thin films. First is the relatively slow increase in conductivity

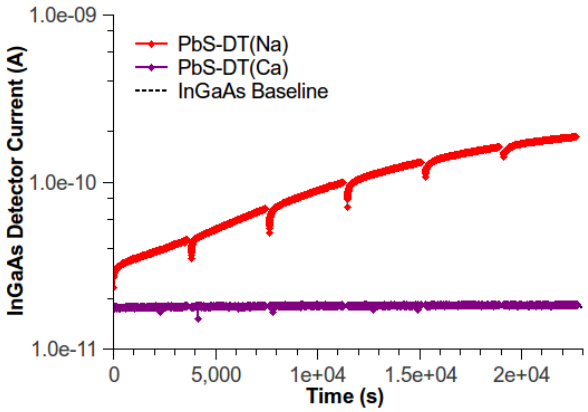

FIGURE 4.9. Electroluminescence of PbS-DT(Na) and PbS-DT(Ca) thin-film devices. Plots of device light emission (as measured by the response of a commercial InGaAs detector) from PbS-DT(Na) and PbS-DT(Ca) thin films as a function of time under +100 V applied bias. (Note: InGaAs detector baseline – measured under dark conditions – lies underneath the PbS-DT(Ca) curve.)

and photoconductivity observed in PbS-DT(Na) films, and the suppression of this time-dependent behavior upon ion-exchange with ions of increased size and valency (NMe_4^+ and Ca^{2+}, respectively). Second is the observed rectification in films of PbS-DT(Na). And third is the remnant photovoltaic behavior seen for PbS-DT(Na) films following the applied bias of a potential step. We hypothesize that all of these observations can be explained by a model in which counter ions to the NC-bound sulfonate groups can respond to an applied electric field and alter energy barriers for electronic charge carriers at the electrode interface.

No prior studies have examined the effects of ionic functional groups on the electronic properties of semiconductor nanocrystal thin films. As an initial point of reference, however, we look to similar systems studied for use in light-emitting electrochemical cells (LECs)[21]. In their most basic form, LEC devices consist of a conjugated, semiconducting polymer blended with salts, sandwiched between two electrodes. They function much in the same manner as light-emitting diodes (LEDs)

– upon application of an electrical bias, electrons and holes are injected into the active layer and recombine to emit light. In LECs, though, the presence of salts introduce mobile *ionic* carriers in addition to the mobile *electronic* carriers. Cations and anions, like holes and electrons, respond to the applied bias and migrate towards, and accumulate near, the cathode and anode, respectively. The accumulation of ions near the electrode interfaces create space-charge regions in the active layer which alter the energies needed for electron and hole injection. The consequence of this, from a device perspective, is that barriers for electronic charge carrier injection are reduced, which results in lower working voltages needed for light emission.

Our PbS-DT system resembles LEC active-layer materials in two important ways. First, PbS-DT nanocrystal thin films consist of a disordered semiconductor array which offer a path for electrons and holes; and secondly, the DT sulfonate ligands offer a source of mobile ions. One notable difference is that in PbS-DT thin films, one of the ions – the sulfonate anion – is bound to the immobile nanocrystals, and presumably contributes little (if any) to the electrical dynamics of the device. Thus, when the device is under bias, only the counter ions (cations) can participate in ionic conduction, and instead of two accumulation regions of mobile cations and anions, PbS-DT IDEs should develop an accumulation region of cations near the cathode, and a wider, depletion region of bound anions near the anode. We now show how this model of mixed ionic, electronic conduction (MIEC) can explain the observed results.

PbS-NCs are known to form barriers at interfaces with gold electrodes[28]. In our devices, MIEC can explain the increase in conductivity and photoconductivity observed in PbS-DT(Na) IDEs with time under bias. Application of an external electric field causes a slow redistribution of mobile Na^+ ions towards the negatively biased electrode (cathode). Over time, an accumulation region of positive space

charge is created near the cathode, and likewise a depletion region of uncompensated, bound sulfonate ions is formed near the anode. The ionic space charge creates localized increases in the electric field strength near the electrode interfaces, which aids in the injection of electronic charge carriers into the nanocrystal film. Thus, the slow increase of device current over time under bias is attributed to the improved charge injection that results from the slow migration of Na^+ ions. Likewise, the improved responsivity of PbS-DT(Na) IDEs with time under bias can be attributed to this same ion-mediated charge injection and extraction. The fact that increases in responsivity follow similar increases in overall device current (Figure 4.3) support this idea.

IDEs of PbS-DT(NMe_4) and PbS-DT(Ca) do not show time-dependent behavior because the NMe_4^+ and Ca^{2+} counter ions in these films are far less mobile relative to Na^+ ions in PbS-DT(Na) IDEs. In the case of PbS-DT(NMe_4) films, the reduced ion mobility is presumably due to the increased steric bulk of NMe_4^+ ions (347 pm) relative to Na^+ ions (98 pm). A dependence of ionic mobility on ion size has been previously observed in polymer LEC systems[29].

The larger steric bulk of NMe_4^+ ions also results in a reduction in absolute conductivity for PbS-DT(NMe_4) films relative PbS-DT(Na) films, presumably because the increased sterics reduce the inter-nanocrystal packing density and thus the efficiency of charge transport between nanocrystals. To separate the two factors of ion mobility and inter-particle separation, PbS-DT(Ca) nanocrystals were prepared. Ca^{2+} ions are close in size to Na^+ ions (99 pm vs. 98 pm, respectively), and thus should lead to similar inter-particle spacings in the respective films. The increased charge density of Ca^{2+} ions relative to Na^+ ions, however, translates to tighter ion binding with bound sulfonate ions, and therefore, reduced mobility. Thus, the

relatively low mobilities of NMe_4^+ and Ca^{2+} counter ions in PbS-DT(NMe_4) and PbS-DT(Ca) devices lead to a flat response with time under bias.

MIEC can also explain the transient IV and after-bias short-circuit response of PbS-DT(Na) IDEs. Our device structure is initially symmetric – a nanocrystal film between two gold electrodes – and shows no initial preference of direction in short-circuit current flow. However, after an extended period under applied bias, redistribution of Na^+ ions creates an ionic gradient that forms an internal electric field that opposes the direction of the applied potential. Upon removal of the applied bias, the ionic gradient is still present and maintains the internal field. The rectification seen in the fast IV sweeps of PbS-DT(Na) IDEs results from the asymmetry induced by this internal electric field – increased current in the direction of the field, and a decreased current opposing the field. Similarly, the photocurrent observed under short-circuit conditions following removal of the applied bias flows with the direction of the internal electric field – that is, opposite to that of the original applied bias. This short-circuit photoresponse – or photovoltaic effect – is very long-lived. Many hours of shorting the device are required to "reset" the device back to its initial state. The large time needed for relaxation is attributed to the slow diffusion of Na^+ ions back to their sulfonate ion pairs.

The increased electroluminescence (EL) of PbS-DT(Na) IDEs vs. PbS-DT(Ca) IDEs (Figure 4.9) also supports the mechanism of MIEC. One of the requirements of EL is the efficient injection of both holes and electrons into the active, luminescent layer. In LECs, this charge carrier injection is aided by the space charge accumulation regions formed by mobile ions. In our devices, we believe that mobile Na^+ ions enable sufficient injection of holes and electrons to result in measurable light emission from EL in PbS-DT(Na) films. The fact that we see any light emission at all from PbS-DT

IDEs is surprising. Our devices consist of relatively thick films of nanocrystals placed between symmetric gold electrodes. This geometry is not optimized for efficient EL. In optimized EL devices, electrodes with work functions close in energy to the active layer HOMO and LUMO levels are chosen to facilitate unidirectional injection of current[30]. Often, additional hole and electron "transport" and/or "blocking" layers are utilized to improve charge carrier balance[3]. Finally, in EL devices based on semiconductor nanocrystals it has been shown that multilayers of NCs decrease EL efficiency by promoting nonradiative recombination pathways. Optimized SC-NC light-emitting devices typically employ nanocrystal monolayers to skirt such issues[3].

We believe the device data collected for PbS-DT IDEs supports the mechanism of MIEC. However, our measurements do not fully rule out other potential mechanisms. In particular, the device response of PbS-DT IDEs could be partially explained by the effects of electronic trapping. In bulk semiconductors, trap states can be caused by localized defects in the crystal lattice, and oxidized or undercoordinated atoms at the semiconductor surface[31]. Trap states introduce available energy levels that lie in the forbidden region of the electronic band gap, and function by temporarily "trapping" holes, electrons, or both. In the special case of a photoconductor, trap states that preferentially capture one photogenerated charge carrier (e.g. electrons) can increase the lifetime for the corresponding carrier of opposite charge (i.e. holes, in this example). Depending on the relative time-scales of trap state occupancy and electron and hole lifetimes, trapping of one charge carrier can allow its partner to make mulitple transits across the device, resulting in photoconductive gain. Thus, trap states can lead to improved response from photoconductive devices. The improvement in the magnitude of the photoresponse comes at the price of a decrease in the time response of the photodetectors.

Thin films of semiconductor nanocrystals, like their bulk crystalline analogues, can harbor trap states. In fact, the increased surface area of nanocrystals makes these materials potentially more susceptible to the introduction of traps. There have been extensive studies on the effects of electronic trap states on the photoresponse of PbS nanocrystal thin films[18,32]. In these photoconductive devices, conduction was hole-dominated and the presence of electron trap states led to improvements in biased photoresponse. One consequence of these traps was a dependence of the magnitude and response time of the photoresponse on the intensity of illumination on the devices, even after the response was normalized for the light power. This behavior was attributed to a population of electron traps of different energies (or depths). At low light intensities, the devices were dominated by the deepest trap states, which consequently resulted in the highest responsivities and slowest response times. As the light intensity was increased, the deep traps became filled (or saturated), the device became dominated by shallower traps, and the photoresponse subsequently decreased in magnitude and increased in switching speed. Furthermore, Sargent et al. was able to correlate the device effects of several observed trap states to specific oxidation products of lead sulfide present in the films after processing[32].

In our study, thin films of PbS-DT(Na) exhibited some of the hallmarks of electronic trapping. PbS-DT IDEs exhibited increased magnitude and reduced switching speed of the photoresponse with a reduction in light intensity (see Figure 4.3). This was true for all PbS-DT thin films, regardless of counter ion (see Figures A.3 and A.4). This independency of the light intensity effect on the counter ion suggests that electronic trapping is a distinct phenomenon from the one causing the ion-dependent effects. Also, the maximum time-scales associated with electronic trap emptying typically fall into the range of tens of seconds[31]. This

contrasts significantly with relaxation times seen in our devices, which can take hours. We therefore discount trap filling or emptying as the basis of the long-lived device dynamics.

Trapping can explain some other effects seen in samples of PbS-DT(Na), though. For some PbS-DT(Na) devices, brief exposures to light during the bias period (when the spectral response was collected), resulted in a quenching of the dark current. One explanation for this behavior is that variation in sample-to-sample air exposure introduces a varying amount of surface traps in the nanocrystal films. Although all nanocrystal samples were synthesized under nitrogen atmosphere, brief exposures to ambient conditions occurred for all samples during film deposition and prior to storage under vacuum. These variations in oxidation should be easy to reduce through better control over the fabrication environment.

From an application point-of-view, ion polarization offers another method with which to tune the efficiencies of photoconductive devices based on semiconductor nanocrystals (SC-NCs) through reduction of barriers at the semiconductor/electrode interface. Similarly, ionically-functionalized nanocrystals (I-NCs) show promise for use in electroluminescent devices based on SC-NCs, particularly if ionic gradients could be "locked in" after formation. An example of a "chemically fixed" ionic gradient has been previously demonstrated for polymer LECs[33].

Additionally, ion exchange chemistry offers an intriguing handle with which to explore new avenues of I-NC research. Fabrication of high-quality, thin-film devices based on non-ionic SC-NCs has benefitted enormously based on advances in layer-by-layer deposition techniques[16]. The vast majority of these methods, however, rely on short-chain, cross-linking molecules (e.g. hydrazine or 1,2-ethanedithiol) that act as insolubilizing agents for the sequential layers of SC-NCs. Choice of linker molecule

is relatively limited using this method, however. I-NCs naturally lend themselves to similar techniques[23], but the presence of the ionic functional group allows for further tuning of properties.

Also, ion exchange chemistry offers a facile method with which to introduce novel functionality into SC-NC thin films (e.g. exchange with redox-active ions). Prior work has demonstrated that functionalization of SC-NCs with redox-active ligands can facilitate charge transfer between nanocrystal and ligand, leading to potential applications as memory devices[34,24].

4.4. Conclusions

We have demonstrated the fabrication of thin-film photoconductors based on PbS-DT nanocrystals compensated by Na^+, NMe_4^+, and Ca^{2+} counter ions. PbS-DT(Na) devices demonstrate time-dependent behavior consistent with a model of mixed ionic, electronic conduction (MIEC), where Na^+ ions respond to an applied bias and aid electronic charge injection and extraction at the electrode interfaces. PbS-DT(Na) devices also demonstrate long-lived rectification and a photovoltaic effect following removal of the applied bias, despite being initially symmetric. We also demonstrate that both "bias" and "after-bias" behavior can be suppressed through ion exchange with ions of increasing size (NMe_4^+) and valency (Ca^{2+}), confirming that transient behavior of PbS-DT(Na) thin films is tied to the presence of mobile Na^+ ions. These ionic effects have implications for improving performance in a variety of photonic devices based on SC-NCs, and warrant further study.

4.5. Experimental

4.5.1. Chemicals

Lead (II) oxide (PbO), oleic acid (OLA, 90% technical grade), 1-octadecene (ODE, 90% technical grade), hexamethyldisilathiane (TMS_2-S), and 2,3-dimercapto-propanesulfonic acid, sodium salt, monohydrate (DT, 95%) were all purchased from Aldrich.

4.5.2. PbS Nanocrystal Synthesis

A typical procedure follows: First, 0.72 g (3.2 mmol) PbO was dissolved in 16 mL (14.2 g, 50 mmol) OLA and heated under vacuum at ∼100°C to drive off water and form lead oleate. Once the water was removed, the flask was back-filled with nitrogen, and the temperature was raised to 130°C. At this stage, 16 mL of a 0.1 M solution of TMS_2-S in ODE was quickly injected into the stirring mixture of Pb-oleate, initiating nucleation of PbS nanocrystal growth. Immediately after injection, the heat was removed, and the flask was left stirring as it slowly cooled to room temperature. The crude nanocrystal solution was purified by a series of precipitation-centrifugation-resuspension steps. Nanocrystals were precipitated with methanol, centrifuged to remove supernatant, and then redissolved in toluene. This procedure was performed twice to remove unreacted lead oleate and freely dissolved oleic acid. A typical yield for this scale is ∼450 mg of PbS-OLA nanocrystals. Unless otherwise specified, nanocrystal solutions were transferred via gas-tight syringe to sealed vessels under an inert N_2 atmosphere. Methanol and toluene used in the work-up were distilled under nitrogen prior to use.

4.5.3. PbS Nanocrystal Ligand Exchange

Natively functionalized oleic-acid capped PbS nanocrystals were exchanged with 2,3-dimercaptopropanesulfonic acid, sodium salt (DT) in a biphasic solution of toluene and water. Biphasic mixtures were manually shaken for ∼1 h and then centrifuged for 5 min at 4000 RPM to break any formed emulsions. The organic layer, along with any remaining organic-soluble NCs, were removed from the aqueous layer and discarded. DT-functionalized NCs (PbS-DT) in the aqueous layer were washed 3x with toluene to remove any remaining free oleic acid. PbS-DT were then precipitated with acetonitrile, centrifuged to remove supernatant, and then redissolved in H_2O. This procedure was performed twice to remove any freely dissolved ligand from the NC solution.

A typical exchange procedure used equal volumes of a 25 mg/mL solution of PbS-OLA in toluene and 78 mM solution of DT in water. The ligand concentration corresponds to ∼5:1 molar ratio of DT/OLA. Under these conditions, an average of 87% of the original mass of PbS-OLA nanocrystals was recovered.

All solvents used in the exchange reactions were either freeze-pump-thaw degassed, or distilled under nitrogen prior to use. All reagents and starting materials used here were obtained from Sigma-Aldrich.

4.5.4. Ion Exchange

Column Exchange (NMe_4^+) A glass column was packed with 10 g (wet) of Dowex®50WX8-400 strong cation exchange resin to give a column height of ∼8.5 cm. This ion-exchange column was first washed with deionized water, then a 1 M aqueous solution of NMe_4OH was run down until eluent came out strongly basic. To remove excess base, additional deionized water was run down the column until the

eluent measured neutral pH. To exchange PbS-DT NCs, a 20-25 mg/mL solution of NCs was run down the prepared ion-exchange column. Excess water was added to push the sample down. Nanocrystal samples came down as a solid band and took ∼10-15 min. to travel down the column.

Solid-State Exchange (Ca^{2+}) A 40 nm thick PbS-DT(Na) film cast onto an interdigitated gold electrode was exchanged with Ca^{2+} ions by submerging the film in a 0.1M aqueous solution of $Ca(NO_3)_2$ for 10 min., followed by a 10 min. soak in deionized water. This two-step process was repeated once with fresh salt and water solutions. Following the last rinse, the film was blown dry with nitrogen and placed under vacuum.

4.5.5. Spectroscopy

Visible and near-infrared (vis-NIR) absorption spectra were measured on a Perkin-Elmer Lambda 1050 Spectrometer. PbS-DT nanocrystals were dissolved in deuterium oxide instead of water for these absorption measurements to minimize O-H stretch overtones that can complicate the spectrum. X-ray photoelectron spectroscopy (XPS) was performed on a Thermo Scientific Escalab 250.

4.5.6. Transmission Electron Microscopy (TEM)

Samples of PbS-DT were prepared using amine-functionalized "Smart Grids" obtained from Dune Sciences, Inc. A drop of dilute PbS-DT solution in deionized water was added atop a"Smart-Grid". After ∼10 sec, the grid was dipped in deionized water to remove excess sample, then blotted dry from beneath using filter paper.

Images were taken using an FEI Tecnai Spirit Transmission Electron Microscope operating at 120 kV and a magnification of 110k.

Minimal processing was performed to enable automated particle counting and sizing using the open-source image analysis software, ImageJ. A Gaussian blur function coupled with application of a bandpass filter was used for background smoothing. Thresholding was achieved through use of the "Multithresholder" plug-in utilizing the "Intermodes" method. Finally, circularity and size constraints were used to remove artifacts and large agglomerates from the count. Particles were fit with an ellipse, and the diameter was taken to be the average of the major and minor axes. Processed images were compared by eye against the raw files to ensure accurate representation of features.

4.5.7. Electrode Fabrication

The active area of the interdigitated gold electrodes (IDE) used in this study consisted of a set of twenty interlocking gold fingers separated by 5-10 μm gaps and running a length of 3 mm. Gold fingers on the IDE were formed using a lift-off procedure. Gold films were deposited by thermal evaporation onto a glass substrate using a chromium adhesion layer, onto a glass substrate patterned with Shipley S1818 photoresist. Gold-coated slides were then soaked in acetone overnight and rinsed with fresh acetone to remove metal not adhered directly to the glass.

4.5.8. Film Casting

Devices were fabricated by spin-coating a PbS-DT film from a concentrated aqueous solution (100 mg/mL) onto a clean gold IDE. Solutions were passed through a 0.45 μm GMF syringe filter to remove agglomerates and improve film quality. To

improve coating between the gold fingers, the IDE was pretreated with oxygen plasma for 2 min. to remove remnant organic molecules from the gold surface and to create a more hydrophillic surface. Deposition was performed in air, and nanocrystal films were dried by placing them under vacuum for a minimum of 12 hours.

4.5.9. Device Characterization

Current-voltage measurements were performed using an Agilent 4156C semiconductor parameter analyzer. Illumination was achieved by focusing light from an EHJ tungsten-halogen lamp through a monochromator and onto the device area. For responsivity measurements, monochromated light was mechanically chopped at a frequency of 35 Hz before being focused onto the device area, and the current was measured using a Stanford Research Systems SR530 lock-in amplifier. For the 1000-1400 nm spectral range measured here, a long pass filter (1000 nm) was used to remove higher order diffraction lines. Light intensity was controlled through use of neutral density filters, and was measured separately at each wavelength using a callibrated InGaAs (Newport) detector placed at the device position. The intensity reported and used for responsivity calculations is that incident on the portion of the film between the gold fingers of the interdigitated electrode.

4.6. Bridge to Chapter V

Chapter IV investigated the opto-electrical properties of thin films fabricated from PbS-DT nanocrystals. This study showed how ionic functionalization – specifically, the identity of the counter ion to the DT sulfonate group – affected the time-dependent behavior of PbS-DT thin films. PbS-DT thin films functionalized with mobile, sodium ions exhibited increased conductance and responsivity with time

under bias, as well as rectification and a short-circuit, photocurrent after removal of the bias. Further experiments, in which sodium ions were replaced with larger (e.g. NMe_4^+) or divalent (e.g. Ca^{2+}) counter ions produced films that exhibited suppression of the time-dependent behavior, and demonstrated tunability of electronic properties through ion exchange.

Chapter V is a concluding overview that will summarize and tie together the main results of Chapters II, III, and IV. Additionally, a brief outlook on future research opportunities for SC-NCs will be presented, with an emphasis on the role that ionic functionalization can play in these efforts.

CHAPTER V

CONCLUDING SUMMARY AND FUTURE OUTLOOKS

As a whole, this document illustrates the important role that surface functionalization – and specifically, ionic functionalization – plays in governing the physical and chemical properties of PbS-NCs. Following is a brief summary of the main results presented in this dissertation, and it is broken down into three main subjects related to ionically-functionalized nanocrystals (I-NCs): 1) Synthesis and Stability of I-NCs (Chapter II), 2) Toxicology of I-NCs (Chapter III), and 3) Optical and Electrical Properties of I-NC Thin Films (Chapters II and IV). Opportunities for future research in these areas follow each summary.

5.1. Synthesis and Stability of I-NCs

5.1.1. Summary of Chapter II

Chapter II demonstrated the facile preparation of two new ionically-functionalized lead sulfide nanocrystals – PbS-MT and PbS-DT. Although both MT and DT ligands are composed of short-chain, alkyl backbones, the ionic functionality of covalently-bound sulfonate groups imbued both moeities with sufficient solution stability to undergo rigorous purification and thin-film fabrication under ambient conditions. Despite their initial stability, both PbS-MT and PbS-DT nanocrystal solutions were found to be susceptible to oxidative decomposition which resulted in particle agglomeration and precipitation. Through a set of experimental trials, molecular oxygen was found to be the primary culprit behind decomposition, with photooxidation serving a secondary role. PbS-DT solutions were also found to be

significantly more stable to oxidative decomposition, which was attributed to the bidentate binding mode of the DT ligand relative to the monodentate MT ligand.

5.1.2. Future Research Opportunities

Although ionic functionality was found to have aided initial stability to PbS-NCs functionalized with short-chain ligands, both materials were destabilized through oxidation of the ligand head groups – thiols in this study. Future studies on nanocrystal stability might look to replace the "weak-link" of the thiol head group with one more robust to oxidation. Since this study was carried out, another research group – Talapin et al. – has discovered a method to functionalize SC-NCs with inorganic ions that forgo the need for an organic chain[1,2]. Although these studies did not include extensive measurements of stability, they did note that some of the ion-functionalized nanocrystals exhibited solution stability for long periods of time under ambient conditions, while others needed to be handled under inert atmosphere. A better understanding of the factors influencing stability in solutions of ionically-functionalized SC-NCs of all types, would prove useful.

The PbS-MT and PbS-DT nanocrystal systems studied here, as well as the inorganic ionic systems of Talapin et al., used anions bound to the nanocrystal surface. In the case of PbS-MT and PbS-MT, the anions were bound covalently through the ligand backbone, while the ions of Talapin et al. were associated electrostatically to undercoordinated metal atoms on the nanocrystal surface. Cationic functionalization, in which positively-charged groups are tethered to the nanocrystal surface has been less explored in SC-NC systems. One could imagine utilizing a ligand of similar backbone to those of the MT and DT ligands, but with a cationic group (e.g. a quaternary ammonium salt) replacing the bound sulfonate group. Effects of cationic

functionalization on stability and optical and electronic properties of thin films are open research questions.

Most close-packed, SC-NC thin films utilize volatile short-chain, or cross-linking organic molecules to reduce barriers to charge transport for electronic studies and applications. These films must be handled with care due to the ability of these ligands to volatilize, leaving bare or oxidized SC-NC films over time. The ionic functionality of the MT and DT ligands greatly reduces their volatility, and in fact, both these materials are solids in their pure state. Although MT and DT ligands can undergo ligand oxidation and desorption from the nanocrystal surface in solution, it is unclear if these same processes would occur in a solid-state film, with no assistance from solvent molecules to disperse oxidized ligand molecules. Future studies, therefore, might look to determine if ionic functionality can impart greater oxidative stability to SC-NC thin films.

5.2. Toxicology of I-NCs

5.2.1. Summary of Chapter III

Chapter III showed that the improvements in oxidative stability afforded by the use of a bidentate, chelating ligand also translate into reduced toxicity in *in vivo* biological systems. Bidentate, and more-stable PbS-DT nanocrystals proved less toxic to embryonic zebrafish than their monodentate, and less-stable analogues, PbS-MT nanocrystals. Additional exposure trials using pure MT and DT showed that the ligands themselves were benign and that toxicity was tied to the nanocrystal-ligand complex. The apparent connection between solution stability and toxicity led to the hypothesis that it was the bare nanocrystal core that was responsible for the toxic response, either through leaching of toxic Pb^{2+} ions or through direct interaction

with sensitive biological systems. This study was one of the first to examine the toxicological effects of the technologically-relevant PbS-NCs, and demonstrated the relevance of solution stability on affecting biological interactions.

5.2.2. Future Research Opportunities

Despite the connection between stability and toxicity, the mechanism of PbS-NC toxicity is still not well understood. Is it the leaching of ionic lead, oxidative stress catalyzed by reactions on the de-ligated nanocrystal surface, or some other effect associated with solution instability that causes mortality and morbidity in embryonic zebrafish? Attempts to relate the toxic response of PbS-MT nanocrystals to an ionic lead control sample proved tentative, at best, due to the difficulty in quantifying doseage. Additionally, due to the complication of different stabilities, the role of the ionic ligand shell on toxicity was not able to be ascertained. Further studies to understand the genetic pathways affected by exposure to PbS-MT and PbS-DT nanocrystal solutions might shed some light on the true culprits of toxicity in these materials, and suggest possible mitigation strategies to make them more benign.

5.3. Optical and Electrical Properties of I-NC Thin Films

5.3.1. Summary of Chapters II and IV

Chapter II demonstrated that the use of short-chain, ionic ligands offers a complementary approach to achieving facile fabrication of high quality thin films for use in a variety of opto-electronic applications. Photodetector devices composed of thin films of PbS-DT nanocrystals exhibited more than two orders of magnitude improvement in both conductivity and photoconductivity relative to devices composed of oleic acid-capped PbS-NCs.

Chapter IV further explored the optical and electronic properties of PbS-DT thin films and demonstrated that the tethered ionic groups on the surface of PbS-DT nanocrystal introduce a new method of tuning the electronic transport properties of nanocrystal thin films. A model in which mobile sodium ions migrated under influence of an applied electric field, was used to explain time-dependent behavior in PbS-DT thin films. Accumulation of sodium ions at the electrode interface reduced charge injection barriers, leading to increases in conductance and responsivity with time under bias. After long periods under bias, the remnant ionic gradient created rectification and a photovoltaic effect in the PbS-DT(Na) film. Both biased, and after-bias behavior could be suppressed through ion exchange of PbS-DT nanocrystals for counter ions of increasing size and valency, both of which presumably have lower ionic mobilities within the film.

5.3.2. Future Research Opportunities

One area of future research for I-NCs is improved fabrication of thin films. Layer-by-layer (LbL) deposition methods have already been utilized to create high-quality, defect-free thin films of SC-NCs, but ligand choice is limited[3]. Ionic functionality could facilitate thin-film formation by allowing LbL deposition of alternating positively- and negatively-charged I-NCs, while still maintaining an ionic handle for further post-depostion, ionic modification. Co-deposition with other ionically-functionalized semiconductors (e.g. conjugated polyelectrolytes) would also be possible. Under the right conditions, this method could allow construction of defect-free I-NC films suitable for sandwich devices.

Additionally, ionic functionality could allow a simple method to introduce additional properties into an I-NC thin film. For example, ion exchange with redox-

active ions (e.g. transition metal ions or viologens) might facilitate charge transfer between ligand and nanocrystal, induce doping of I-NC cores for improved charge transport, or induce changes in absorption and/or emission profiles. Any or all of these examples have potential for future research avenues.

APPENDIX

SUPPLEMENTARY MATERIAL TO CHAPTER IV

A.1. Supplementary Figures

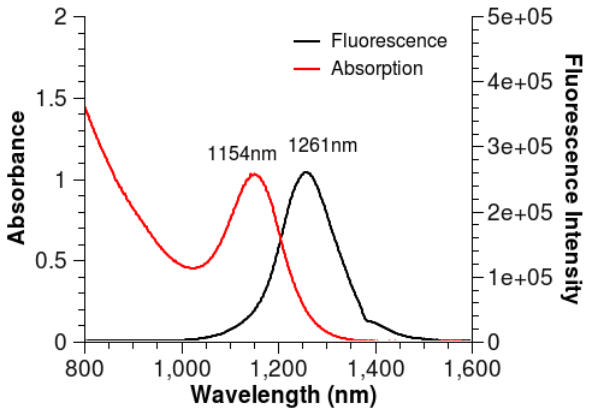

FIGURE A.1. Fluorescence (*black*) and absorption spectra (*red*) for a typical solution of PbS-DT(Na) nanocrystals. This batch of particles was not used in the device study, but was synthesized under the same method and conditions.

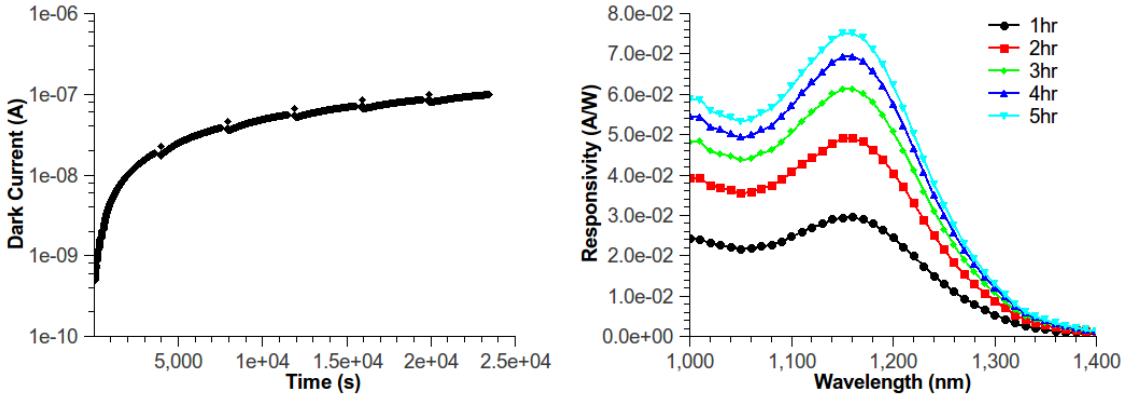

FIGURE A.2. Time-dependent device response of a control sample: a column-exchanged PbS-DT(Na) thin film. (*left*) Device current vs. time under an applied voltage of +10 V. All data points reflect "dark" measurements. Data gaps regularly spaced along the curves represent brief periods where the photoconductive response was probed (see right plot). After each of these light exposures, the films undergo a brief relaxation period as they return to equilibrium in the "dark" conductive state. (*right*) Spectral response curves recorded over a longer period of time and collected during the data gaps of the +10 V potential step (shown at left). The applied +10 V bias was kept constant as the device was switched between dark and light conditions.

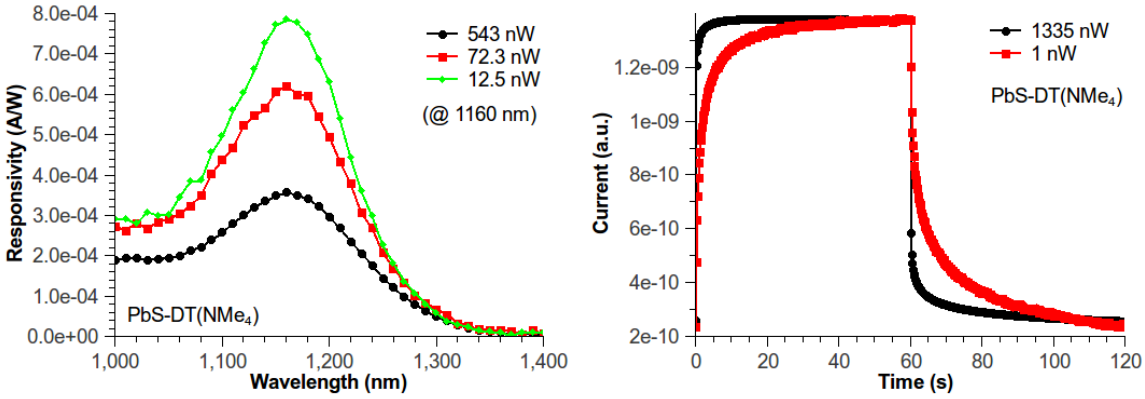

FIGURE A.3. Photoresponse of a PbS-DT(NMe_4) thin film device. (*left*) Spectral response of a PbS-DT(NMe_4) device under +10 V applied bias as a function of light intensity. (*right*) Time response of the device current for the same device at the start (0 to 60 s) and finish (60 to 120 s) of a 60 s exposure to 1190 nm light. Total device current (in arbitrary units) is overlaid for exposures to two different light intensities. Note that low light exposure curve was expanded for ease of comparison. (*Also:* Light chopper was removed for this experiment.) Both sets of measurements were performed consecutively following a long applied bias of +10 V. Bias was maintained throughout without break. Lines serve only as guides for the eye.

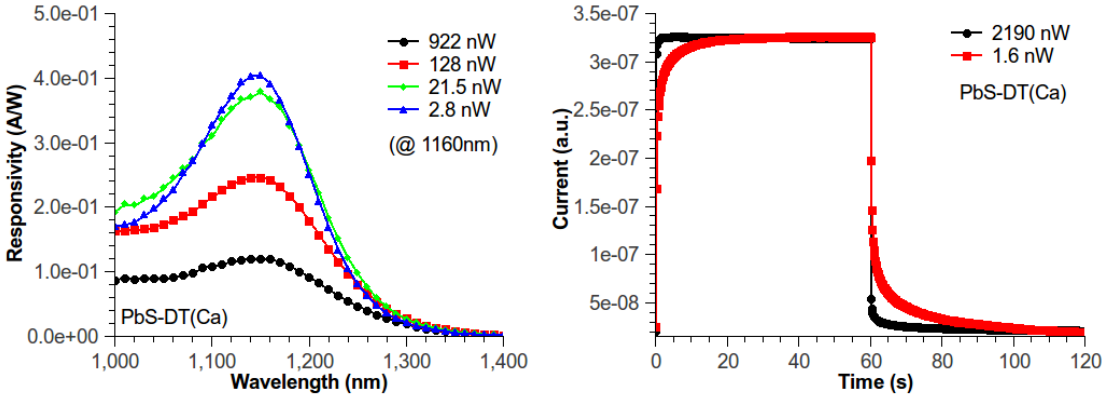

FIGURE A.4. Photoresponse of a PbS-DT(Ca) thin film device. (*left*) Spectral response of a PbS-DT(Ca) device under +10 V applied bias as a function of light intensity. (*right*) Time response of the device current for the same device at the start (0 to 60 s) and finish (60 to 120 s) of a 60 s exposure to 1190 nm light. Total device current (in arbitrary units) is overlaid for exposures to two different light intensities. Note that low light exposure curve was expanded for ease of comparison. (*Also:* Light chopper was removed for this experiment.) Both sets of measurements were performed consecutively following a long applied bias of +10 V. Bias was maintained throughout without break. Lines serve only as guides for the eye.

REFERENCES CITED

References for Chapter I

[1] ASTM E2456-08A, *Terminology for Nanotechnology*; Technical Report, 2006.

[2] Steckel, J. S.; Coe-Sullivan, S.; Bulovic, V.; Bawendi, M. G. *Advanced Materials* **2003**, *15*, 1862–1866.

[3] Rogach, A. L.; Gaponik, N.; Lupton, J. M.; Bertoni, C.; Gallardo, D. E.; Dunn, S.; Pira, N. L.; Paderi, M.; Repetto, P.; Romanov, S. G.; O'Dwyer, C.; Torres, C. M. S.; Eychmuller, A. *Angewandte Chemie International Addition* **2008**, *47*, 6538–6549.

[4] Chan, W. C. W.; Nie, S. *Science* **1998**, *281*, 2016–2018.

[5] Rogach, A. L.; Eychmuller, A.; Hickey, S. G.; Kershaw, S. V. *Small* **2007**, *3*, 536–557.

[6] Hillhouse, H. W.; Beard, M. C. *Current Opinion in Colloid & Interface Science* **2009**, *14*, 245–259.

[7] Sargent, E. H. *Nature Photonics* **2009**, *3*, 325–331.

[8] Konstantatos, G.; Howard, I.; Fischer, A.; Hoogland, S.; Clifford, J.; Klem, E.; Levina, L.; Sargent, E. H. *Nature* **2006**, *442*, 180–183.

[9] Hyun, B.-R.; Chen, H.; Rey, D. A.; Wise, F. W.; Batt, C. A. *The Journal of Physical Chemistry B* **2007**, *111*, 5726–5730.

[10] Sze, S. M. *Physics of Semiconductor Devices*, 2nd ed.; John Wiley & Sons, 1981.

[11] Bube, R. H. *Photoconductivity of Solids*, 2nd ed.; John Wiley & Sons, Inc., 1967.

[12] Alivisatos, A. P. *Science* **1996**, *271*, 933–937.

[13] Norris, D. J. In *Semiconductor and Metal Nanocrystals: Synthesis and Electronic and Optical Properties*; Klimov, V. I., Ed.; Marcel Dekker, Inc., 2004; Chapter 2, pp 65–102.

[14] Wise, F. W. *Accounts of Chemical Research* **2000**, *33*, 773–780.

[15] Allan, G.; Delerue, C. *Physical Review B* **2004**, *70*, 245321.

[16] Nozik, A. J.; Beard, M. C.; Luther, J. M.; Law, M.; Ellingson, R. J.; Johnson, J. C. *Chemical Reviews* **2010**, *110*, 6873–6890.

[17] Ellingson, R. J.; Beard, M. C.; Johnson, J. C.; Yu, P.; Micic, O. I.; Nozik, A. J.; Shabaev, A.; Efros, A. L. *Nano Letters* **2005**, *5*, 865–871.

[18] Allan, G.; Delerue, C. *Physical Review B* **2006**, *73*, 205423.

[19] Xu, J.; Cui, D.; Zhu, T.; Paradee, G.; Liang, Z.; Wang, Q.; Xu, S.; Wang, A. Y. *Nanotechnology* **2006**, *17*, 5428–5434.

[20] Peng, Z. A.; Peng, X. *Journal Of The American Chemical Society* **2001**, *123*, 1389–1395.

[21] Asokan, S.; Krueger, K. M.; Colvin, V. L.; Wong, M. S. *Small* **2007**, *3*, 1164–1169.

[22] Rosetti, R.; Nakahara, S.; Brus, L. E. *Journal of Chemical Physics* **1983**, *79*, 1086–1088.

[23] Murray, C. B.; Norris, D. J.; Bawendi, M. G. *Journal of the American Chemical Society* **1993**, *115*, 8706–8715.

[24] Murray, C. B.; Kagan, C. R.; Bawendi, M. G. *Annual Review of Materials Science* **2000**, *30*, 545–610.

[25] Yin, Y.; Alivisatos, A. P. *Nature* **2005**, *437*, 664–670.

[26] LaMer, V. K.; Dinegar, R. H. *Journal of the American Chemical Society* **1950**, *72*, 4847–4854.

[27] Peng, Z. A.; Peng, X. *Journal Of The American Chemical Society* **2001**, *123*, 183–184.

[28] Qu, L.; Peng, Z. A.; Peng, X. *Nano Letters* **2001**, *1*, 333–337.

[29] Murray, C. B.; Sun, S.; Gaschler, W.; Doyle, H.; Betley, T. A.; Kagan, C. R. *IBM Journal of Research & Development* **2001**, *45*, 47–56.

[30] Hines, M.; Scholes, G. *Advanced Materials* **2003**, *15*, 1844–1849.

[31] Hines, M. A.; Guyot-Sionnest, P. *The Journal of Physical Chemistry* **1996**, *100*, 468–471.

[32] Dabbousi, B. O.; Rodriguez-Viejo, J.; Mikulec, F. V.; Heine, J. R.; Mattoussi, H.; Ober, R.; Jensen, K. F.; Bawendi, M. G. *The Journal of Physical Chemistry B* **1997**, *101*, 9463–9475.

[33] Cao, Y.; Banin, U. *Journal of the American Chemical Society* **2000**, *122*, 9692–9702.

[34] Zhao, X.; Gorelikov, I.; Musikhin, S.; Cauchi, S.; Sukhovatkin, V.; Sargent, E.; Kumacheva, E. *Langmuir* **2005**, *21*, 1086–1090.

[35] Hinds, S.; Myrskog, S.; Levina, L.; Koleilat, G.; Yang, J.; Kelley, S. O.; Sargent, E. H. *Journal Of The American Chemical Society* **2007**, *129*, 7218–7219.

[36] Pearson, R. G. *Journal of the American Chemical Society* **1963**, *85*, 3533–3539.

[37] Nag, A.; Kovalenko, M. V.; Lee, J.-S.; Liu, W.; Spokoyny, B.; Talapin, D. V. *Journal of the American Chemical Society* **2011**, *133*, 10612–10620.

[38] Moody, I. S.; Stonas, A. R.; Lonergan, M. C. *The Journal of Physical Chemistry C* **2008**, *112*, 19383–19389.

[39] Liu, D.; Snee, P. T. *ACS Nano* **2011**, *5*, 546–550.

[40] Jarosz, M. V.; Porter, V. J.; Fisher, B. R.; Kastner, M. A.; Bawendi, M. G. *Physical Review B* **2004**, *70*, 195327.

[41] Law, M.; Luther, J. M.; Song, Q.; Hughes, B. K.; Perkins, C. L.; Nozik, A. J. *Journal of the American Chemical Society* **2008**, *130*, 5974–5985.

[42] Williams, K. J.; Tisdale, W. A.; Leschkies, K. S.; Haugstad, G.; Norris, D. J.; Aydil, E. S. *ACS Nano* **2009**, *3*, 1532–1538.

[43] Zarghami, M. H.; Liu, Y.; Gibbs, M.; Gebremichael, E.; Webster, C.; Law, M. *ACS Nano* **2010**, *4*, 2475–2485.

[44] Barkhouse, D. A. R.; Pattantyus-Abraham, A. G.; Levina, L.; Sargent, E. H. *ACS Nano* **2008**, *2*, 2356–2362.

[45] Aldana, J.; Wang, Y.; Peng, X. *Journal of the American Chemical Society* **2001**, *123*, 8844–8850.

[46] Mulvihill, M. J.; Habas, S. E.; Plante, I. J.-L.; Wan, J.; Mokari, T. *Chemistry of Materials* **2010**, *22*, 5251–5257.

[47] Ji, X.; Copenhaver, D.; Sichmeller, C.; Peng, X. *Journal of the American Chemical Society* **2008**, *130*, 5726–5735.

[48] Cornacchio, A. L. P.; Jones, N. D. *Journal of Materials Chemistry* **2006**, *16*, 1171–1177.

[49] Querner, C.; Reiss, P.; Bleuse, J.; Pron, A. *Journal of the American Chemical Society* **2004**, *126*, 11574–11582.

[50] Dubois, F.; Mahler, B.; Dubertret, B.; Doris, E.; Mioskowski, C. *Journal Of The American Chemical Society* **2007**, *129*, 482–483.

[51] Guo, W.; Li, J. H.; Wang, A.; Peng, X. *Journal Of The American Chemical Society* **2003**, *125*, 3901–3909.

[52] Kotov, N. A.; Winter, J. O.; Clements, I. P.; Jan, E.; Timko, B. P.; Campidelli, S.; Pathak, S.; Mazzatenta, A.; Lieber, C. M.; Prato, M.; Bellamkonda, R. V.; Silva, G. A.; Kam, N. W. S.; Patolsky, F.; Ballerini, L. *Advanced Materials* **2009**, *21*, 3970–4004.

[53] Meng, H.; Chen, Z.; Xing, G.; Yuan, H.; Chen, C.; Zhao, F.; Zhang, C.; Zhao, Y. *Toxicology Letters* **2007**, *175*, 102–110.

[54] Bar-Ilan, O.; Albrecht, R. M.; Fako, V. E.; Furgeson, D. Y. *Small* **2009**, *5*, 1897–1910.

[55] Derfus, A. M.; Chan, W. C.; Bhatia, S. N. *Nano Letters* **2004**, *4*, 11–18.

[56] Kovalenko, M. V.; Heiss, W.; Shevchenko, E. V.; Lee, J.-S.; Schwinghammer, H.; Alivisatos, A. P.; Talapin, D. V. *Journal Of The American Chemical Society* **2007**, *129*, 11354–11355.

[57] Tang, J.; Konstantatos, G.; Hinds, S.; Myrskog, S.; Pattantyus-Abraham, A. G.; Clifford, J.; Sargent, E. H. *ACS Nano* **2009**, *3*, 331–338.

[58] Baumgardner, W. J.; Choi, J. J.; Lim, Y.-F.; Hanrath, T. *Journal Of The American Chemical Society* **2010**, *132*, 9519–9521.

[59] Harper, S. L.; Carriere, J. L.; Miller, J. M.; Hutchison, J. E.; Maddux, B. L. S.; Tanguay, R. L. *ACS Nano* **2011**, *5*, 4688–4697.

[60] Kirchner, C.; Liedl, T.; Kudera, S.; Pellegrino, T.; Javier, A. M.; Gaub, H. E.; Stolzle, S.; Fertig, N.; Parak, W. J. *Nano Letters* **2005**, *5*, 331–338.

[61] Rehg, T. J.; Higgins, B. G. *AlChE Journal* **1992**, *38*, 489–501.

[62] Luther, J. M.; Law, M.; Song, Q.; Perkins, C. L.; Beard, M. C.; Nozik, A. J. *ACS Nano* **2008**, *2*, 271–280.

[63] Talapin, D. V.; Lee, J.-S.; Kovalenko, M. V.; Shevchenko, E. V. *Chemical Reviews* **2010**, *110*, 389–458.

[64] Murphy, J.; Beard, M.; Nozik, A. *The Journal of Physical Chemistry B* **2006**, *110*, 25455–25461.

[65] Liu, Y.; Gibbs, M.; Puthussery, J.; Gaik, S.; Ihly, R.; Hillhouse, H. W.; Law, M. *Nano Letters* **2010**, *10*, 1960–1969.

[66] Koleilat, G. I.; Levina, L.; Shukla, H.; Myrskog, S. H.; Hinds, S.; Pattantyus-Abraham, A. G.; Sargent, E. H. *ACS Nano* **2008**, *2*, 833–840.

[67] Kang, M. S.; Sahu, A.; Norris, D. J.; Frisbie, C. D. *Nano Letters* **2011**, *11*, 3887–3892.

[68] Yu, D.; Wang, C.; Wehrenberg, B. L.; Guyot-Sionnest, P. *Physical Review Letters* **2004**, *92*, 216802.

[69] Wehrenberg, B. L.; Yu, D.; Ma, J.; Guyot-Sionnest, P. *The Journal of Physical Chemistry B* **2005**, *109*, 20192–20199.

[70] Klem, E. J. D.; MacNeil, D. D.; Cyr, P. W.; Levina, L.; Sargent, E. H. *Applied Physics Letters* **2007**, *90*, 183113.

[71] Sambur, J. B.; Novet, T.; Parkinson, B. A. *Science* **2010**, *330*, 63–66.

[72] Konstantatos, G.; Sargent, E. H. *Proceedings of the IEEE* **2009**, *97*, 1666–1683.

[73] Lim, Y. T.; Kim, S.; Nakayama, A.; Stott, N. E.; Bawendi, M. G.; Frangioni, J. V. *Molecular Imaging* **2003**, *2*, 50–64.

[74] Colvin, V. L.; Schlamp, M. C.; Alivisatos, A. P. *Nature* **1994**, *370*, 354–357.

[75] Tessler, N.; Medvedev, V.; Kazes, M.; Kan, S.; Banin, U. *Science* **2002**, *295*, 1506–1508.

[76] Konstantatos, G.; Huang, C.; Levina, L.; Lu, Z.; Sargent, E. H. *Advanced Functional Materials* **2005**, *15*, 1865–1869.

[77] Konstantatos, G.; Sargent, E. H. *Applied Physics Letters* **2007**, *91*, 173505.

[78] Konstantatos, G.; Levina, L.; Fischer, A.; Sargent, E. H. *Nano Letters* **2008**, *8*, 1446–1450.

References for Chapter II

[1] Yin, Y.; Alivisatos, A. P. *Nature* **2005**, *437*, 664–670.

[2] Bakueva, L.; Musikhin, S.; Hines, M. A.; Chang, T. W. F.; Tzolov, M.; Scholes, G. D.; Sargent, E. H. *Applied Physics Letters* **2003**, *82*, 2895–2897.

[3] Oertel, D. C.; Bawendi, M. G.; Arango, A. C.; Bulovic, V. *Applied Physics Letters* **2005**, *87*, 213505.

[4] Konstantatos, G.; Howard, I.; Fischer, A.; Hoogland, S.; Clifford, J.; Klem, E.; Levina, L.; Sargent, E. H. *Nature* **2006**, *442*, 180–183.

[5] Gur, I.; Fromer, N. A.; Geier, M. L.; Alivisatos, A. P. *Science* **2005**, *310*, 462–465.

[6] McDonald, S. A.; Konstantatos, G.; Zhang, S. G.; Cyr, P. W.; Klem, E. J. D.; Levina, L.; Sargent, E. H. *Nature Materials* **2005**, *4*, 138–142.

[7] Schwenn, P. E.; Watt, A. A. R.; Rubinsztein-Dunlop, H.; Meredith, P. *Proceedings of SPIE* **2006**, *6038*, 603818.

[8] Klem, E. J. D.; Levina, L.; Sargent, E. H. *Applied Physics Letters* **2005**, *87*, 053101.

[9] Maria, A.; Cyr, P. W.; Klern, E. J. D.; Levina, L.; Sargent, E. H. *Applied Physics Letters* **2005**, *87*, 213112.

[10] Klem, E. J. D.; MacNeil, D. D.; Cyr, P. W.; Levina, L.; Sargent, E. H. *Applied Physics Letters* **2007**, *90*, 183113.

[11] Leatherdale, C. A.; Kagan, C. R.; Morgan, N. Y.; Empedocles, S. A.; Kastner, M. A.; Bawendi, M. G. *Physical Review B* **2000**, *62*, 2669–2680.

[12] Jarosz, M. V.; Porter, V. J.; Fisher, B. R.; Kastner, M. A.; Bawendi, M. G. *Physical Review B* **2004**, *70*, 195327.

[13] Murphy, J.; Beard, M.; Nozik, A. *The Journal of Physical Chemistry B* **2006**, *110*, 25455–25461.

[14] Yu, D.; Wang, C.; Guyot-Sionnest, P. *Science* **2003**, *300*, 1277–1280.

[15] Talapin, D. V.; Murray, C. B. *Science* **2005**, *310*, 86–89.

[16] Konstantatos, G.; Clifford, J.; Levina, L.; Sargent, E. H. *Nature Photonics* **2007**, *1*, 531–534.

[17] Law, M.; Luther, J. M.; Song, Q.; Hughes, B. K.; Perkins, C. L.; Nozik, A. J. *Journal of the American Chemical Society* **2008**, *130*, 5974–5985.

[18] Hinds, S.; Myrskog, S.; Levina, L.; Koleilat, G.; Yang, J.; Kelley, S. O.; Sargent, E. H. *Journal Of The American Chemical Society* **2007**, *129*, 7218–7219.

[19] Luther, J. M.; Law, M.; Song, Q.; Perkins, C. L.; Beard, M. C.; Nozik, A. J. *ACS Nano* **2008**, *2*, 271–280.

[20] Hyun, B.-R.; Chen, H.; Rey, D. A.; Wise, F. W.; Batt, C. A. *The Journal of Physical Chemistry B* **2007**, *111*, 5726–5730.

[21] Woehrle, G. H.; Warner, M. G.; Hutchison, J. E. *The Journal of Physical Chemistry B* **2002**, *106*, 9979–9981.

[22] Mattoussi, H.; Mauro, J. M.; Goldman, E. R.; Anderson, G. P.; Sundar, V. C.; Mikulec, F. V.; Bawendi, M. G. *Journal of the American Chemical Society* **2000**, *122*, 12142–12150.

[23] Aldana, J.; Wang, Y.; Peng, X. *Journal of the American Chemical Society* **2001**, *123*, 8844–8850.

[24] Bachrach, S. M.; Woody, J. T.; Mulhearn, D. C. *The Journal of Organic Chemistry* **2002**, *67*, 8983–8990.

[25] Cornacchio, A. L. P.; Jones, N. D. *Journal of Materials Chemistry* **2006**, *16*, 1171–1177.

[26] Stouwdam, J.; Shan, J.; vanVeggel, F.; Pattantyus-Abraham, A.; Young, J.; Raudsepp, M. *The Journal of Physical Chemistry C* **2007**, *111*, 1086–1092.

[27] Hines, M.; Scholes, G. *Advanced Materials* **2003**, *15*, 1844–1849.

[28] Lin-Vien, D.; Colthup, N. B.; Fateley, W. G.; Grasselli, J. G. *The Handbook of Infrared and Raman Characteristic Frequencies of Organic Molecules*; Academic Press, Inc., 1991; p 246.

[29] Leatherdale, C. A.; Bawendi, M. G. *Physical Review B* **2001**, *63*, 165315.

[30] Wuister, S. F.; de Mello Donega, C.; Meijerink, A. *The Journal of Physical Chemistry B* **2004**, *108*, 17393–17397.

[31] Jeong, S.; Achermann, M.; Nanda, J.; Ivanov, S.; Klimov, V. I.; Hollingsworth, J. A. *Journal of the American Chemical Society* **2005**, *127*, 10126–10127.

[32] Zingg, D. S.; Hercules, D. M. *The Journal of Physical Chemistry* **1978**, *82*, 1992–1995.

[33] Cheng, C.; Lonergan, M. *Journal of the American Chemical Society* **2004**, *126*, 10536–10537.

[34] Bernards, D. A.; Flores-Torres, S.; Abruna, H. D.; Malliaras, G. G. *Science* **2006**, *313*, 1416–1419.

References for Chapter III

Agency for Toxic Substances and Disease Registry (ATSDR) (2007) Toxicological Profile for Lead. Technical Report, U.S. Department of Health and Human Services, Public Health Service, Atlanta

Aldana J, Wang Y, Peng X (2001) Photochemical instability of CdSe nanocrystals coated by hydrophilic thiols. Journal of the American Chemical Society 123(36):8844–8850

Bar-Ilan O, Albrecht RM, Fako VE, Furgeson DY (2009) Toxicity assessments of multisized gold and silver nanoparticles in zebrafish embryos. Small 5(16):1897–1910

Barbazuk WB, Korf I, Kadavi C, Heyen J, Tate S, Wun E, Bedell JA, McPherson JD, Johnson SL (2000) The syntenic relationship of the zebrafish and human genomes. Genome Research 10(9):1351–1358

Bharali DJ, Khalil M, Gurbiz M, Simone TM, Mousa SA (2009) Nanoparticles and cancer therapy: A concise review with emphasis on dendrimers. International Journal of Nanomedicine 4:1–7

De Gennaro LD (1978) The effects of lead nitrate on the central nervous system of the chick embryo I. Observations of light and electron microscopy. Growth 42(2):141–155

den Hertog J (2005) Chemical genetics: Drug screens in zebrafish. Bioscience Reports 25(5-6):289–297

Dobrovolskaia MA, McNeil SE (2007) Immunological properties of engineered nanomaterials. Nature Nanotechnology 2(8):469–478

Dodd A, Curtis PM, Williams LC, Love DR (2000) Zebrafish: Bridging the gap between development and disease. Human Molecular Genetics 9(16):2443–2449

Guo L, Von Dem Bussche A, Buechner M, Yan A, Kane AB, Hurt RH (2008) Adsorption of essential micronutrients by carbon nanotubes and the implications for nanotoxicity testing. Small 4(6):721–727

Haendel MA, Tilton F, Bailey GS, Tanguay RL (2004) Developmental toxicity of the dithiocarbamate pesticide sodium metam in zebrafish. Toxicological Sciences 81(2):390–400

Hall JB, Dobrovolskaia MA, Patri AK, McNeil SE (2007) Characterization of nanoparticles for therapeutics. Nanomedicine 2(6):789–803

Hill AJ, Teraoka H, Heideman W, Peterson RE (2005) Zebrafish as a model vertebrate for investigating chemical toxicity. Toxicological Sciences 86(1):6–19

Hinds S, Myrskog S, Levina L, Koleilat G, Yang J, Kelley SO, Sargent EH (2007) NIR-emitting colloidal quantum dots having 26 % luminescence quantum yield in buffer solution. Journal Of The American Chemical Society 129(23):7218–7219

Hoshino A, Fujioka K, Oku T, Suga M, Sasaki YF, Ohta T, Yasuhara M, Suzuki K, Yamamoto K (2004) Physicochemical properties and cellular toxicity of nanocrystal quantum dots depend on their surface modification. Nano Letters 4(11):2163–2169

Hyun BR, Chen H, Rey DA, Wise FW, Batt CA (2007) Near-infrared fluorescence imaging with water-soluble lead salt quantum dots. The Journal of Physical Chemistry B 111:5726–5730

Kimmel CB, Ballard WW (1995) Stages of embryonic development of the zebrafish. Developmental Dynamics 203(3):253–310

Kirchner C, Liedl T, Kudera S, Pellegrino T, Javier AM, Gaub HE, Stolzle S, Fertig N, Parak WJ (2005) Cytotoxicity of colloidal CdSe and CdSe/ZnS nanoparticles. Nano Letters 5(2):331–338

Koleilat GI, Levina L, Shukla H, Myrskog SH, Hinds S, Pattantyus-Abraham AG, Sargent EH (2008) Efficient, stable infrared photovoltaics based on solution-cast colloidal quantum dots. ACS Nano 2(5):833–840

Konstantatos G, Howard I, Fischer A, Hoogland S, Clifford J, Klem E, Levina L, Sargent EH (2006) Ultrasensitive solution-cast quantum dot photodetectors. Nature 442:180–183

Konstantatos G, Huang C, Levina L, Lu Z, Sargent EH (2005) Efficient infrared electroluminescent devices using solution-processed colloidal quantum dots. Advanced Functional Materials 15:1865–1869

Kotov NA, Winter JO, Clements IP, Jan E, Timko BP, Campidelli S, Pathak S, Mazzatenta A, Lieber CM, Prato M, Bellamkonda RV, Silva GA, Kam NWS, Patolsky F, Ballerini L (2009) Nanomaterials for neural interfaces. Advanced Materials 21:3970–4004

Lewinski N, Colvin V, Drezek R (2008) Cytotoxicity of nanoparticles. Small 4(1):26–49

Lim YT, Kim S, Nakayama A, Stott NE, Bawendi MG, Frangioni JV (2003) Selection of quantum dot wavelengths for biomedical assays and imaging. Molecular Imaging 2(1):50–64

Liu J, Aruguete DM, Murayama M, Hochella MF Jr (2009) Influence of size and aggregation on the reactivity of an environmentally and industrially relevant nanomaterial (PbS). Environmental Science & Technology 43(21):8178–8183

Long TC, Saleh N, Tilton RD, Lowry GV, Veronesi B (2006) Titanium dioxide (P25) produces reactive oxygen species in immortalized brain microglia (BV2): Implications for nanoparticle neurotoxicity. Environmental Science & Technology 40(14):4346–4352

McDonald SA, Konstantatos G, Zhang SG, Cyr PW, Klem EJD, Levina L, Sargent EH (2005) Solution-processed PbS quantum dot infrared photodetectors and photovoltaics. Nature Materials 4:138–142

Meng H, Chen Z, Xing G, Yuan H, Chen C, Zhao F, Zhang C, Zhao Y (2007) Ultrahigh reactivity provokes nanotoxicity: Explanation of oral toxicity of nano-copper particles. Toxicology Letters 175(1-3):102–110

Minchin RF, Martin DJ (2010) Minireview: Nanoparticles for molecular imaging – an overview. Endocrinology 151(2):474–481

Moody IS, Stonas AR, Lonergan MC (2008) PbS nanocrystals functionalized with a short-chain, ionic, dithiol ligand. The Journal of Physical Chemistry C 112(49):19383–19389

Newman MD, Stotland M, Ellis JI (2009) The safety of nanosized particles in titanium dioxide- and zinc oxide-based sunscreens. Journal of the American Academy of Dermatology 61(4):685–692

Parng C (2005) In vivo zebrafish assays for toxicity testing. Current Opinion in Drug Discovery and Development 8:100–106

Rubinstein AL (2003) Zebrafish: From disease modeling to drug discovery. Current Opinion in Drug Discovery and Development 6(2):218–223

Samia ACS, Chen X, Burda C (2003) Semiconductor quantum dots for photodynamic therapy. Journal Of The American Chemical Society 15(51):15736–15737

Seale-Goldsmith MM, Leary JF (2009) Nanobiosystems. Wiley Interdisciplinary Reviews: Nanomedicine and Nanobiotechnology 1(5):553–567

Sharma V, Sharma A, Kansal L (2010) The effect of oral administration of allium sativum extracts on lead nitrate induced toxicity in male mice. Food and Chemical Toxicology 48(3):928–936

Teraoka H, Dong W, Hiraga T (1993) Zebrafish as a novel experimental model for developmental toxicology. Clinical Genetics 43(2):123–132

Ton C, Lin Y, Willett C (2006) Zebrafish as a model for developmental neurotoxicity testing. Birth Defects Research Part A: Clinical and Molecular Teratology 76(7):553–567

Usenko CY, Harper SL, Tanguay RL (2007) In vivo evaluation of carbon fullerene toxicity using embryonic zebrafish. Carbon 45(9):1891–1898

White LD, Cory-Slechta DA, Gilbert ME, Tiffany-Castiglioni E, Zawia NH, Virgolini M, Rossi-George A, Lasley SM, Qian YC, Basha MR (2007) New and evolving concepts in the neurotoxicology of lead. Toxicology and Applied Pharmacology 225(1):1–27

Wise JPS, Goodale BC, Wise SS, Craig GA, Pongan AF, Walter RB, Thompson WD, Ng AK, Aboueissa AM, Mitani H, Spalding MJ, Mason MD (2010) Silver nanospheres are cytotoxic and genotoxic to fish cells. Aquatic Toxicology 97(1):34–41

Yang L, Ho NY, Alshut R, Legradi J, Weiss C, Reischl M, Mikut R, Liebel U, Muller F, Strahle U (2009) Zebrafish embryos as models for embryotoxic and teratological effects of chemicals. Reproductive Toxicology 28(2):245–253

Zelikoff JT, Li JH, Hartwig A, Wang XW, Costa M, Rossman TG (1988) Genetic toxicology of lead compounds. Carcinogenesis 9:1727–1732

Zhang T, Stilwell JL, Gerion D, Ding L, Elboudwarej O, Cooke PA, Gray JW, Alivisatos AP, Chen FF (2006) Cellular effect of high doses of silica-coated quantum dot profiled with high throughput gene expression analysis and high content cellomics measurements. Nano Letters 6:800–808

References for Chapter IV

[1] Talapin, D. V.; Lee, J.-S.; Kovalenko, M. V.; Shevchenko, E. V. *Chemical Reviews* **2010**, *110*, 389–458.

[2] Wise, F. W. *Accounts of Chemical Research* **2000**, *33*, 773–780.

[3] Steckel, J. S.; Coe-Sullivan, S.; Bulovic, V.; Bawendi, M. G. *Advanced Materials* **2003**, *15*, 1862–1866.

[4] Bakueva, L.; Gorelikov, I.; Musikhin, S.; Zhao, X. S.; Sargent, E. H.; Kumacheva, E. *Advanced Materials* **2004**, *16*, 926–929.

[5] Sargent, E. H. *Nature Photonics* **2009**, *3*, 325–331.

[6] Koleilat, G. I.; Levina, L.; Shukla, H.; Myrskog, S. H.; Hinds, S.; Pattantyus-Abraham, A. G.; Sargent, E. H. *ACS Nano* **2008**, *2*, 833–840.

[7] Fu, H.; Tsang, S.-W.; Zhang, Y.; Ouyang, J.; Lu, J.; Yu, K.; Tao, Y. *Chemistry of Materials* **2011**, *23*, 1805–1810.

[8] Konstantatos, G.; Howard, I.; Fischer, A.; Hoogland, S.; Clifford, J.; Klem, E.; Levina, L.; Sargent, E. H. *Nature* **2006**, *442*, 180–183.

[9] Konstantatos, G.; Clifford, J.; Levina, L.; Sargent, E. H. *Nature Photonics* **2007**, *1*, 531–534.

[10] Hinds, S.; Levina, L.; Klem, E. J. D.; Konstantatos, G.; Sukhovatkin, V.; Sargent, E. H. *Advanced Materials* **2008**, *20*, 4398–4402.

[11] Klem, E. J. D.; Shukla, H.; Hinds, S.; MacNeil, D. D.; Levina, L.; Sargent, E. H. *Applied Physics Letters* **2008**, *92*, 212105.

[12] Law, M.; Luther, J. M.; Song, Q.; Hughes, B. K.; Perkins, C. L.; Nozik, A. J. *Journal of the American Chemical Society* **2008**, *130*, 5974–5985.

[13] Williams, K. J.; Tisdale, W. A.; Leschkies, K. S.; Haugstad, G.; Norris, D. J.; Aydil, E. S. *ACS Nano* **2009**, *3*, 1532–1538.

[14] Liu, Y.; Gibbs, M.; Puthussery, J.; Gaik, S.; Ihly, R.; Hillhouse, H. W.; Law, M. *Nano Letters* **2010**, *10*, 1960–1969.

[15] Zarghami, M. H.; Liu, Y.; Gibbs, M.; Gebremichael, E.; Webster, C.; Law, M. *ACS Nano* **2010**, *4*, 2475–2485.

[16] Luther, J. M.; Law, M.; Song, Q.; Perkins, C. L.; Beard, M. C.; Nozik, A. J. *ACS Nano* **2008**, *2*, 271–280.

[17] Mentzel, T. S.; Porter, V. J.; Geyer, S.; MacLean, K.; Bawendi, M. G.; Kastner, M. A. *Physical Review B* **2008**, *77*, 075316.

[18] Konstantatos, G.; Sargent, E. H. *Applied Physics Letters* **2007**, *91*, 173505.

[19] Zhao, N.; Osedach, T. P.; Chang, L.-Y.; Geyer, S. M.; Wanger, D.; Binda, M. T.; Arango, A. C.; Bawendi, M. G.; Bulovic, V. *ACS Nano* **2010**, *4*, 3743–3752.

[20] Baik, S. J.; Kim, K.; Lim, K. S.; Jung, S.; Park, Y.-C.; Han, D. G.; Lim, S.; Yoo, S.; Jeong, S. *The Journal of Physical Chemistry C* **2011**, *115*, 607–612.

[21] deMello, J. C.; Tessler, N.; Graham, S. C.; Friend, R. H. *Physical Review B* **1998**, *57*, 12951–12963.

[22] Hyun, B.-R.; Chen, H.; Rey, D. A.; Wise, F. W.; Batt, C. A. *The Journal of Physical Chemistry B* **2007**, *111*, 5726–5730.

[23] Kovalenko, M. V.; Bodnarchuk, M. I.; Talapin, D. V. *Journal of the American Chemical Society* **2010**, *132*, 15124–15126.

[24] Nag, A.; Kovalenko, M. V.; Lee, J.-S.; Liu, W.; Spokoyny, B.; Talapin, D. V. *Journal of the American Chemical Society* **2011**, *133*, 10612–10620.

[25] Kang, M. S.; Lee, J.; Norris, D. J.; Frisbie, C. D. *Nano Letters* **2009**, *9*, 3848–3852.

[26] Moody, I. S.; Stonas, A. R.; Lonergan, M. C. *The Journal of Physical Chemistry C* **2008**, *112*, 19383–19389.

[27] Hines, M.; Scholes, G. *Advanced Materials* **2003**, *15*, 1844–1849.

[28] Gao, J.; Perkins, C. L.; Luther, J. M.; Hanna, M. C.; Chen, O. E., Hsiang-Yu an Semonin; Nozik, A. J.; Ellingson, R. J.; Beard, M. C. *Nano Letters* **2011**, *11*, 3263–3266.

[29] Hu, Y.; Gao, J. *Applied Physics Letters* **2006**, *89*, 253514.

[30] Colvin, V. L.; Schlamp, M. C.; Alivisatos, A. P. *Nature* **1994**, *370*, 354–357.

[31] Bube, R. H. *Photoconductivity of Solids*, 2nd ed.; John Wiley & Sons, Inc., 1967.

[32] Konstantatos, G.; Levina, L.; Fischer, A.; Sargent, E. H. *Nano Letters* **2008**, *8*, 1446–1450.

[33] Leger, J. M.; Patel, D. G.; Rodovsky, D. B.; Bartholomew, G. P. *Advanced Functional Materials* **2008**, *18*, 1212–1219.

[34] Das, B. C.; Pal, A. J. *ACS Nano* **2008**, *2*, 1930–1938.

References for Chapter V

[1] Kovalenko, M. V.; Bodnarchuk, M. I.; Zaumseil, J.; Lee, J.-S.; Talapin, D. V. *Journal of the American Chemical Society* **2010**, *132*, 10085–10092.

[2] Nag, A.; Kovalenko, M. V.; Lee, J.-S.; Liu, W.; Spokoyny, B.; Talapin, D. V. *Journal of the American Chemical Society* **2011**, *133*, 10612–10620.

[3] Luther, J. M.; Law, M.; Song, Q.; Perkins, C. L.; Beard, M. C.; Nozik, A. J. *ACS Nano* **2008**, *2*, 271–280.